







## **Development and Validation of a CFD Multiphase Model for Micro-channels**

Design of Small Heat Exchangers for Small Module Reactors

#### **Sven Jaspers**

Supervisor: Stefano Lorenzi

Full Professor, Politecnico di Milano

Wouter Schroeyers Full Professor, Hasselt Univeristy

Co-supervisor: Marco Enrico Ricotti

Full Professor, Politecnico di Milano

Andrea Missaglia

PhD Researcher, Politecnico di Milano & Massachusetts Institute of Technology

Faculty of Engineering Technology

Master in Nuclear Engineering Technology

Master Thesis

Hasselt, June 2025

Development and Validation of a CFD Multiphase Model for Micro-channels
Copyright © 2025 - Sven Jaspers.

This dissertation is original work, written solely for this purpose, and all the authors whose studies and publications contributed to it have been duly cited. Partial reproduction is allowed with acknowledgment of the author and reference to the degree, academic year, institution - *Hasselt University & KU Leuven & Politecnico di Milano* - and public defense date.

## Acknowledgements

I would like to express my gratitude to Prof. Lorenzi and Prof. Ricotti from Politecnico di Milano for their valuable guidance and for providing the topic that laid the foundation for this work. I am also sincerely thankful to Prof. Wouter Schroeyers from Hasselt University for his support and insightful feedback throughout the project.

A special thanks goes to Andrea Missaglia for his continuous guidance throughout the thesis, his assistance greatly enriched the technical aspects of this work and helped me push through the difficult moments.

Additionally, I would like to thank all those who contributed to discussions and offered encouragement along the way, especially Jelle Vandeweyer, who helped me persevere during the late nights and early mornings when the model was as unstable as Boltzmann's and Ehrenfest's mental health in 1906 and 1933.

Lastly, I can't forget to thank two other classmates, Enes and Jorrit, who helped me retain *la passion* for multiphase CFD and of course my beloved girlfriend, other friends and family, for keeping up with my *trabajo*.

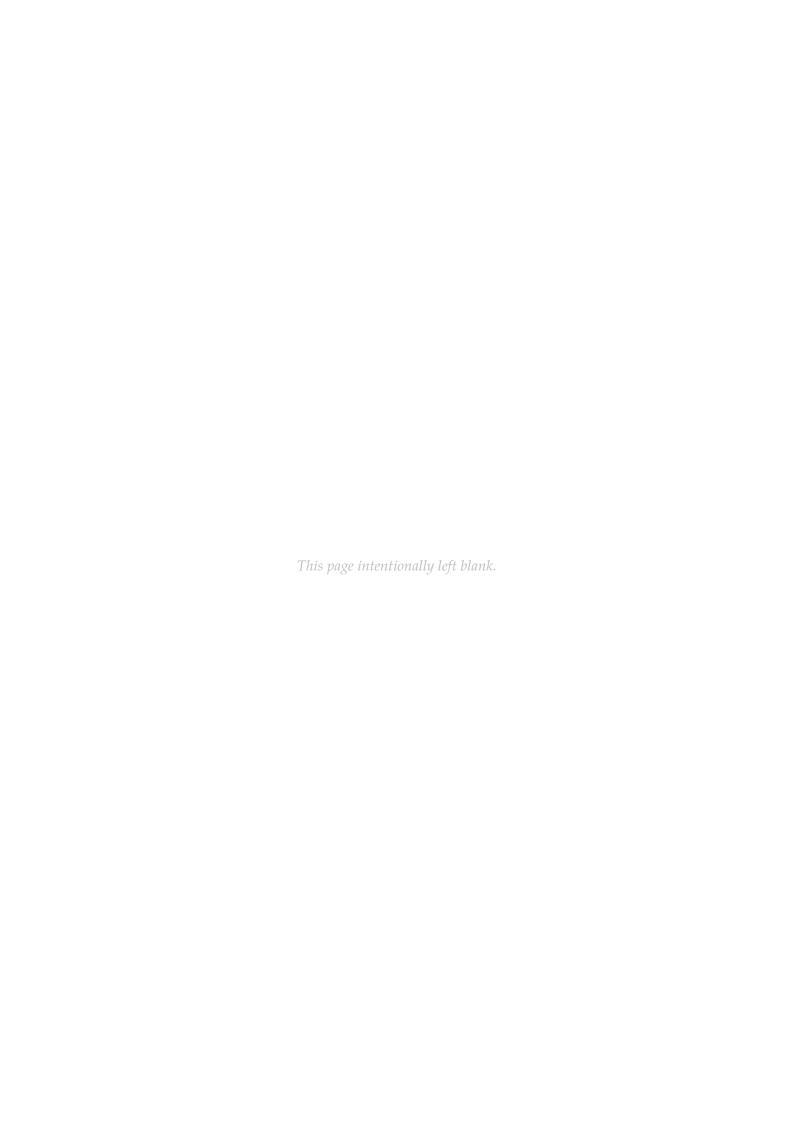
All models are wrong, but some are useful.

~ George E.P. Box

## **Abstract**

This master's thesis presents the development and validation of a Computational Fluid Dynamics model for adiabatic two-phase flow and boiling heat transfer in a single microchannel, with a focus on applications for Microchannel Heat Exchangers in Small Modular Reactors. The Eulerian–Eulerian multiphase approach was adopted and several interfacial forces and heat transfer mechanisms were tested for maximum applicability to match the experimental setups. A modular modeling strategy was employed, progressing from an adiabatic baseline adiabatic model (vertical small channel) to a refined adiabatic model (horizontal microchannel) to a complete boiling model (vertical microchannel). The baseline and refined models showed strong agreement with experimental data for void fraction, velocity profiles, specific flow regimes and pressure drops. However, the critical lack of high-resolution data and sub-models for horizontal microchannel flows limited development and quantitative validation for the refined model. Boiling simulations predicted pressure drops and wall superheat trends consistent with literature but revealed sensitivity mainly due to liquid film stability. Overall, the models proved a good foundation for key thermo-hydraulic behavior, specifically in annular flow regimes, but showed limitations in more extreme conditions and regimes. Future work to progress to a full scale Microchannel Heat Exchanger model should prioritize horizontal flow datasets and robust interfacial force models suitable for broader flow regimes.

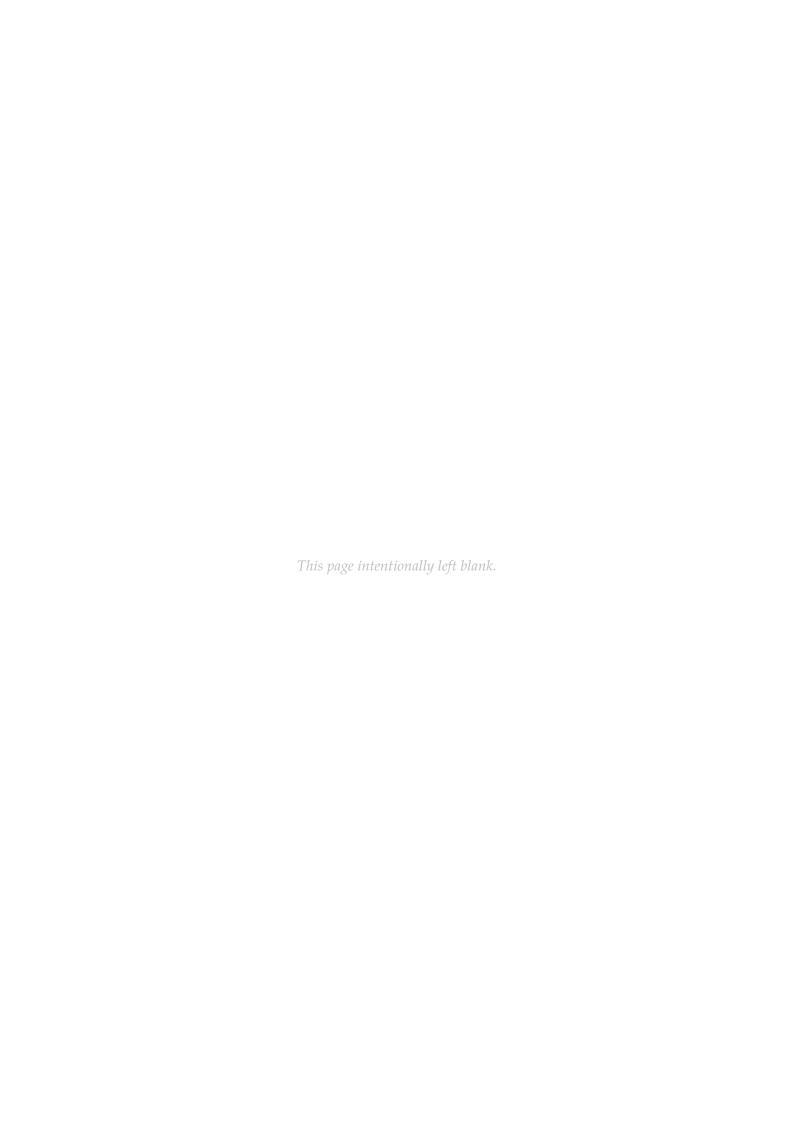
**Keywords:** Computational Fluid Dynamics, Two-Phase Flow, Microchannel Heat Exchangers, Eulerian–Eulerian Model, Wall Boiling, Small Modular Reactors



## **Abstract**

Deze masterscriptie beschrijft de ontwikkeling en validatie van een Computational Fluid Dynamics-model voor adiabatische en diabatisch twee-fasenstroming in een microkanaal, met focus op toepassingen in Microkanaal-Warmtewisselaars voor Small Modular Reactors. De Euleriaans-Euleriaanse methode werd toegepast en meerdere interfaciale krachten en warmteoverdrachtsmodellen werden getest op toepasbaarheid binnen experimentele configuraties. Een modulaire strategie werd gevolgd, van een adiabatisch basismodel (verticale kleine kanaal), tot een verfijnd adiabatisch model (horizontaal microkanaal), naar een volledig kookmodel (verticaal microkanaal). De eerste twee modellen toonden sterke overeenkomst met experimentele data voor volumefracties, snelheidsprofielen, stromingsregimes en drukverliezen. Voor horizontale stroming vormde het gebrek aan gedetailleerde data en geschikte submodellen echter een beperking. De kooksimulaties voorspelden drukverliezen en wandoververhitting correct, maar toonden gevoeligheid voor de stabiliteit van de vloeistoffilm aan de wand. De modellen vormen een degelijke basis voor thermo-hydraulisch gedrag in annulair regime, maar zijn beperkt bij extremere condities. Toekomstig werk moet zich richten op horizontale data en robuustere krachtmodellen voor bredere stromingsregimes.

**Keywords:** Computational Fluid Dynamics, Twee-fasenstroming, Microkanaal warmtewisselaars, Euleriaans–Euleriaanse methode, Kleine Modulaire Reactor



## Contents

Li	st of F	igures		xiv
Li	st of T	ables		xix
1	Intr	oductio	on to Small Heat Exchangers and Multiphase CFD	1
	1.1	Introd	duction to the Topic	1
	1.2	Micro	channel Heat Exchangers	2
	1.3	Multi	-phase Computational Fluid Dynamics	4
		1.3.1	Current State of the Art	4
			1.3.1.1 Averaging Methods	4
			1.3.1.2 Interface-Resolving Methods	4
		1.3.2	Challenges with Two-Phase Flow CFD	5
	1.4	Scope	and Objectives of this Thesis	6
		1.4.1	Research Questions	7
		1.4.2	Modeling Roadmap	7
	1.5	Theor	retical Foundation	8
		1.5.1	Eulerian-Eulerian Framework: Adiabatic	10
			1.5.1.1 Continuity Equations	10
			1.5.1.2 Momentum Conservation	11
		1.5.2	Eulerian-Eulerian Framework: Extension to Diabatic	12
	1.6	Flow	Regimes in microchannels	13
		1.6.1	Different flow regimes	13
		1.6.2	Classification of flow regimes	14
		1.6.3	Boiling flow regimes	15
		1.6.4	Challenges in modeling flow regimes	15
		1.6.5	Analytical and (non-CFD) numerical framework	16
	1.7	Two-F	Phase Flow Interaction Forces	16
		1.7.1	Lift Force	16
			1.7.1.1 Physical Background	16
			1.7.1.2 Overview of Modeling Approaches	18
		1.7.2	Turbulent Dispersion Force	19
			1.7.2.1 Physical Background	19
			1.7.2.2 Overview of modeling approaches	19
		173	Wall Lubrication Force	20

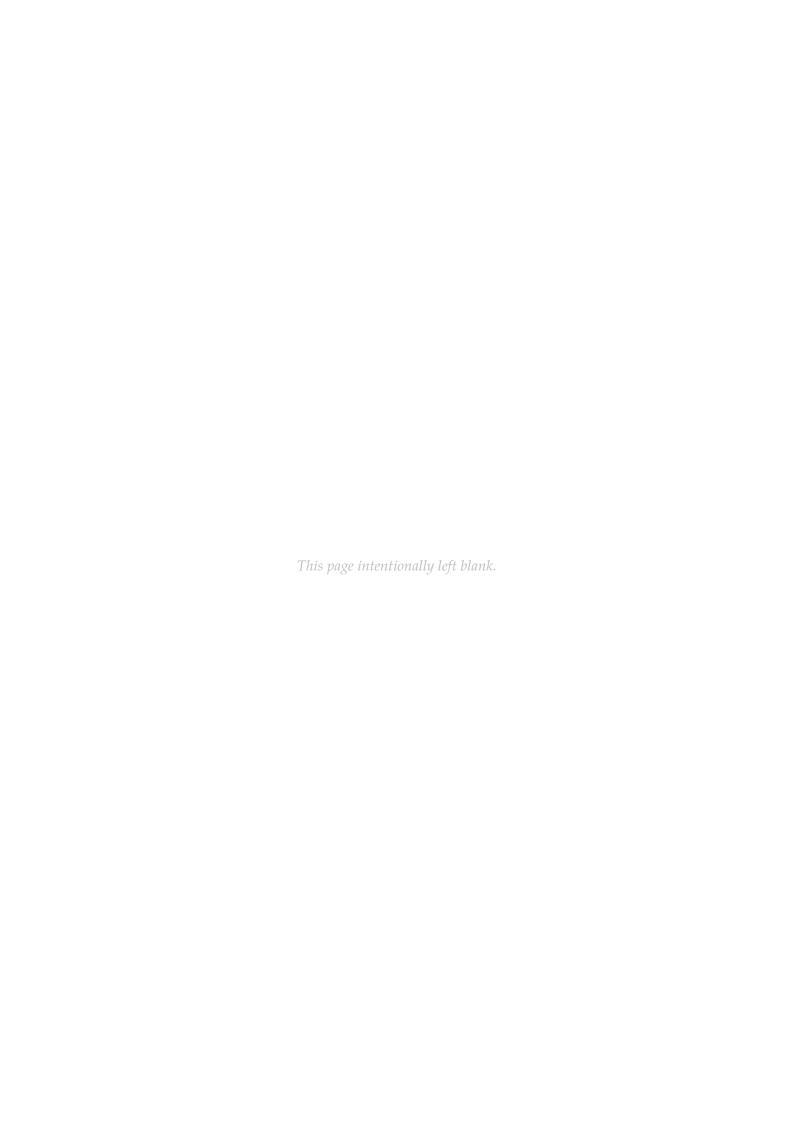
CONTENTS ix

			1.7.3.1	Physical Background	20
			1.7.3.2	Overview of Modeling Approaches	20
		1.7.4	Virtual N	Mass Force	21
		1.7.5	Drag For	rce	21
			1.7.5.1	Physical Background	21
			1.7.5.2	Overview of Modeling Approaches	22
		1.7.6	Basset (1	History) Force	22
	1.8	Turbul	lence Mo	deling in Multiphase Flows	23
		1.8.1	$k - \varepsilon Mc$	odel	23
		1.8.2	$k - \omega M$	odel	24
		1.8.3	Applicat	tion in Multiphase Flows	24
		1.8.4	Wall Tre	atment and Considerations	24
	1.9	Bubble	e Size Gro	ouping & Interfacial Area	25
		1.9.1	Populati	on Balance Models & MUSIG	25
		1.9.2	Method	of Moments & S- $\gamma$	26
		1.9.3		Iean Diameter	26
	1.10	Wall B	oiling .		27
		1.10.1	Convect	ive Heat Transfer	27
		1.10.2	Evapora	tive Heat Transfer	27
		1.10.3	Quenchi	ing Heat Transfer	29
		1.10.4	Modelin	g Strategies	29
2	Mat	erials a	nd Meth	ods	31
	2.1				32
		2.1.1		ry and mesh	32
		2.1.2		Models	33
			2.1.2.1	Lift Force: Sugrue	33
			2.1.2.2	Turbulent Dispersion Force: Lopez de Bertodano	35
			2.1.2.3	Wall Lubrication Force: Antal et al	35
			2.1.2.4	Drag Froce: Tomiyama	36
			2.1.2.5	Virtual Mass Force: Zuber	37
			2.1.2.6	Turbulence: $k-\varepsilon$ Model	37
			2.1.2.7	Bubble Group Size: Pre-Integrated S–γ Model	37
		2.1.3	Boundar	ry and Initial Conditions	38
		011			
		2.1.4	Solver pa	arameters and Monitoring	38
	2.2		-	arameters and Monitoring	38 39
	2.2		d model	<u> </u>	
	2.2	Refine	d model Geometi		39 39
	2.2	Refine 2.2.1	d model Geometi	ry and mesh	39
	2.2	Refine 2.2.1	d model Geometr Physics	ry and mesh	39 39 40
	2.2	Refine 2.2.1	d model Geometr Physics 1 2.2.2.1	ry and mesh	39 39 40 41

X CONTENTS

			2.2.2.5	Virtual Mass Force: Zuber	44
			2.2.2.6	Turbulence: $k-\varepsilon$ Model	44
		2.2.3	Boundar	ry and Initial Conditions	44
			2.2.3.1	Void Fractions & Correction Factor $\Psi \dots \dots$	44
			2.2.3.2	Other Boundary and Initial Conditions	46
		2.2.4	Solver P	arameters and Monitoring	47
	2.3	Boilin	g model		47
		2.3.1	Geometr	ry and mesh	47
		2.3.2	Physics 1	Models	48
			2.3.2.1	Interfacial Forces	48
			2.3.2.2	Boiling Model	48
		2.3.3	Boundar	ry and Initial Conditions	49
		2.3.4	Solver So	ettings and Strategy	50
	2.4	Perfor	med Simi	ulations & Setups	51
		2.4.1	Baseline	Model	51
		2.4.2	Refined	Model	51
		2.4.3	Boiling I	Model	52
		2.4.4	Monitor	ing of the simulations	52
_	ъ	1. 0.1	D		- 4
3			Discussio		54 54
	3.1				54
		3.1.1		tional Work	54
		3.1.2	-	Velocity and Void Fraction Profile Validation	54
			3.1.2.1	Radial Void-Fraction Results	55 
			3.1.2.2	Liquid Radial Velocity Results	55 56
			3.1.2.3	Two-Dimensional Profile Comparison	56
			3.1.2.4	Common Results	61
	2.2	D. C	3.1.2.5	Mesh Sensitivity Analysis	62
	3.2				64
		3.2.1	_	Strategy Choice	64
		3.2.2		ve Performance of the Correction Factor $\Psi$	65
		3.2.3		e Drops	66
			3.2.3.1	Case A: High Velocity Ratio	66
			3.2.3.2	Case B: Normal Velocity Ratio	67
			3.2.3.3	Case C: Low Velocity Ratio	68
		224	3.2.3.4	Discussion of the Pressure Drop Results	68
		3.2.4		gime Testing	70
			3.2.4.1	Bubbly Flow	70
			3.2.4.2	Slug Flow	70
			3.2.4.3	Wavy-Annular Flow	72
			3.2.4.4	Annular Flow	72
		3.2.5	Liquid F	Film Comparison	73

3.3 Boiling Model					76
		3.3.1	Pressure	e Drop	76
		3.3.2	Wall Su	perheat Behavior	78
			3.3.2.1	Wall Temperature and Heat Flux Response	78
			3.3.2.2	Wall Superheating Trends	79
			3.3.2.3	Wall Superheat Difference	80
		3.3.3	Mesh Se	ensitivity Analysis	80
			3.3.3.1	Baze Size Comparison	80
			3.3.3.2	Butterfly vs Quadrilateral Comparison	82
		3.3.4	Turbule	nce Analysis	83
4	Con	clusior	ns and Fu	ture Developments	84
	4.1	Concl	usions .		84
		4.1.1	Baseline	e Model	84
		4.1.2	Refined	Model	85
		4.1.3	Boiling	Model	85
		4.1.4	Pressure	e Drop Comparison and General Conclusion	86
	4.2	Future	e Develop	oments	86
Aj	ppen	dices			
A	App	endix			98
	A.1	STAR-	-CCM+ I	mplementation Code	98
		A.1.1		s Lift Coefficient	98
		A.1.2	Lopez d	le Bertodano's Turbulent Dispersion Model	98
В	App	endix			99
	B.1	Other	Used Co	des	99
		B.1.1	Python	Script for Turbulence Calculation	99
		B.1.2	MITB S	TAR-CCM+ Implementation Code	100



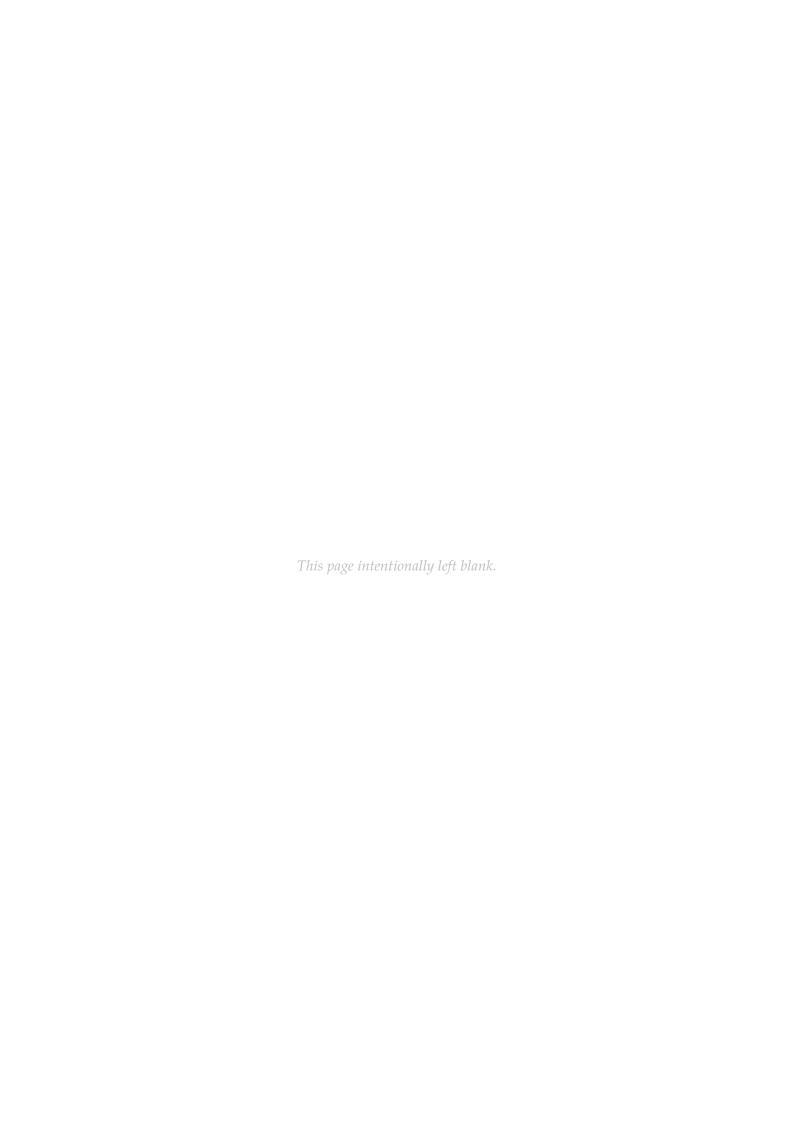
## List of Figures

1.1	Different microchannel two-phase flow regimes	14
1.2	Flow regime map in $We_{LS}$ - $We_{GS}$ space with experimental data and regime	
	boundaries	15
1.3	Schematic of lift-induced lateral migration of a spherical bubble in a wall-bound	ded
	shear flow	17
1.4	Schematic comparison of lift-force direction and sign of $C_L$ for a spherical	
	bubble (+), a deformed bubble (–) and a solid particle (–)	18
1.5	Schematic of the turbulent dispersion force acting on neighboring bubbles.	19
1.6	Schematic of wall lubrication force	20
1.7	Schematic of virtual mass force	21
1.8	Schematic of drag force (with bubble swarm)	22
1.9	Typical $y^+$ zones and corresponding turbulence modeling strategies. The	
	high- $y^+$ (log-law) region used in this study is compatible with standard	
	wall functions and avoids the need for resolving the viscous sublayer	25
1.10	Schematic of single-phase convective heat transfer from the wall to the con-	
	tinuous liquid phase	28
1.11	Schematic representation of evaporative heat transfer from the wall to a	
	growing vapor bubble	28
1.12	Schematic representation of quenching heat transfer	29
1.13	Conceptual representation of the complete and self-consistent wall boiling	
	framework, illustrating the interdependencies between nucleation, sliding,	
	evaporation, and quenching mechanisms	30
2.1	Cross-section comparison of mesh topologies used in the baseline pipe ge-	
	ometry	32
2.2	Full view of the patched (butterfly) mesh applied to the 9-meter baseline	
	pipe	33
2.3	Comparison of Sugrue's and Tomiyama's Lift Coefficient	34
2.4	Mesh overview of the unified mesh strategy	40
2.5	Mesh overview of the split mesh strategy	40
2.6	Comparison of full-domain mesh strategies for the refined model	41

LIST OF FIGURES xv

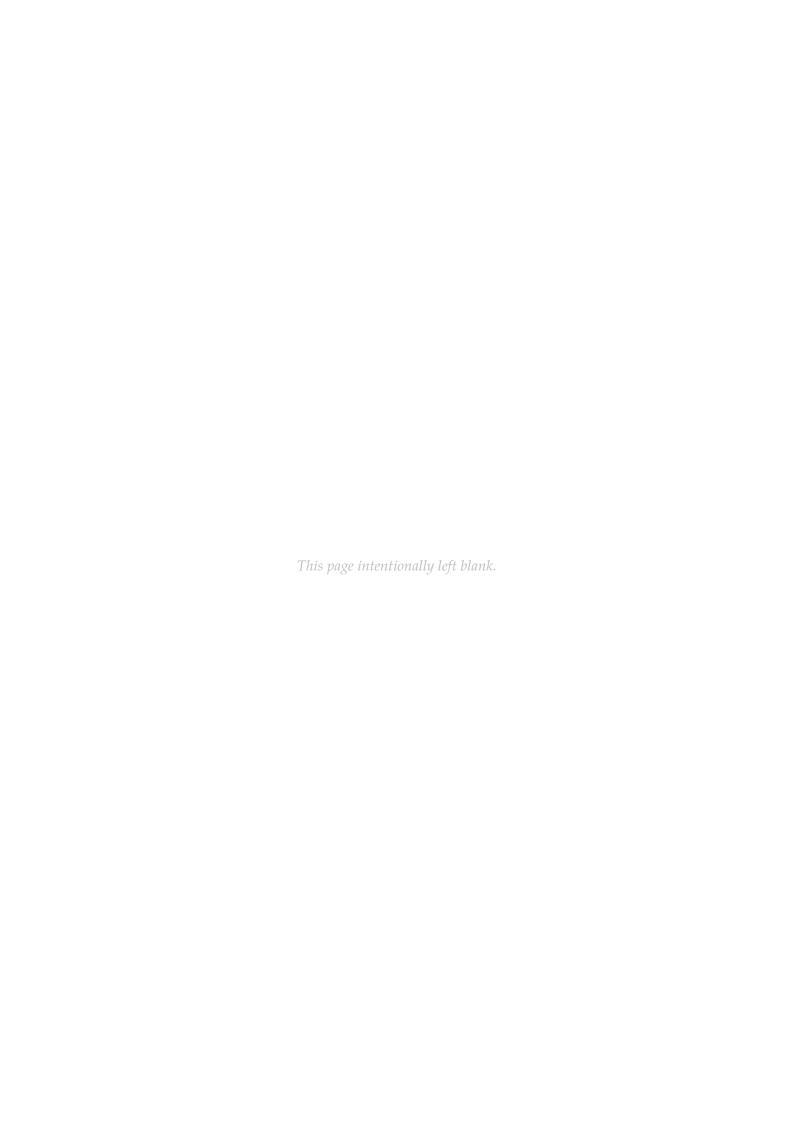
2.7	Schematic of Lubchenko's approach (a) side view of bubbles, (b) front view of the cross-sections of bubbles. (c) cross-section of gas phase as a function of distance from the wall.	43
2.8	Correction ratio $\Psi$ as a function of ratio of velocities $(u_{dc})$ , based on the ratio between experimentally reported void fraction and the corrected inlet condition.	45
2.9	Comparison of mesh refinement levels for the boiling model	48
	Example of instability caused by singularity	53
3.1	Radial void-fraction, Cases A–D	57
3.2	Radial velocity, Cases A–D	58
3.3	2D profile comparison	59
3.4	2D profile comparison	60
3.5	The influence of $C_{TD}$ on the void fraction distribution (top view), from low	
	$C_{TD}$ (0.2) to extremely high $C_{TD}$ (1.5)	61
3.6	Mass-conservation error for the air phase	62
3.7	Mass-conservation error for the liquid phase	62
3.8	Influence of mesh strategy on radial profiles for Case B	63
3.9	Comparison of stable vs unstable velocity near the liquid–air interface	64
3.10	Comparison of stable vs unstable velocity near the outlet region	64
3.11	Simulated vs. experimental pressure drop results for case A ( $j_c$ = 0.156 m/s).	67
3.12	Simulated vs. experimental pressure drop results for case B ( $j_c$ = 0.515 m/s).	67
3.13	Simulated vs. experimental pressure drop results for case C ( $j_c$ = 3.018 m/s).	68
3.14	Void fraction color scale used for all visualized flow regime results	70
3.15	Comparison of experimental and simulated bubbly flow	71
3.16	Comparison of experimental and simulated slug (Taylor) flow	71
3.17	Comparison of experimental and simulated wavy-annular flow	72
3.18	Comparison of experimental and simulated annular flow	73
3.19	Comparison of predicted liquid film thickness for the simulation and the	
	experimental data	74
3.20	Visualization of simulated liquid film behavior across five representative	
	cases, highlighting transitions from stable to unstable regimes and eventual	
	film depletion	75
3.21	Absolute pressure comparison along the microchannel between experimen-	
	tal and simulation	76
3.22	Liquid film thickness along the microchannel at $Q=151kW/m^2$	77
3.23	Absolute temperature comparison along the microchannel between experi-	
	mental and simulation	78
3.24	Wall superheat under varying heat fluxes for different mass fluxes together	
	with the pool boiling correlation and crusical points A & B	79
	Differences is dominant heat transfer mechanism	79
3.26	Wall superheat difference along the flow direction for $G = 106.5 \text{ kg/m}^2\text{s.}$ .	80

3.27	Comparison of void fraction field across different mesh resolutions	81
3.28	Pressure drop prediction for different mesh resolutions	82
3.29	Comparison of void fraction distribution across mesh types	82
3.30	Pressure drop comparison between butterfly and quadrilateral mesh simu-	
	lations.	83



## List of Tables

2.1	Overview of mesh types and controls used for the baseline model	32
2.2	Overview of all models used for the baseline model	33
2.3	Overview of solver settings for the baseline model	39
2.4	Overview of mesh types and controls used for the refined model	39
2.5	Overview of all models used for the refined model	41
2.6	Overview of solver settings for the refined model	47
2.7	Overview of mesh types and controls used for the boiling model	47
2.8	Overview of solver settings for the boiling model	50
3.1	Comparison of peak void fraction and peak liquid velocity	56
3.2	Overview of the predictive performance of the correlation factor $\Psi$	65
3.3	Experimental data, theoretical calculated parameters and simulation results	
	for case A	66
3.4	Experimental data, theoretical parameters, and simulation results for Case B	67
3.5	Experimental data, theoretical parameters, and simulation results for Case C.	68
3.6	Comparison of theoretical, and simulated liquid film thicknesses in $\mu m$	73
3.7	Comparison of imposed heat fluxes and wall temperature response at $G =$	
	$106.5 \text{ kg/m}^2\text{s.}$	78



1

# Introduction to Small Heat Exchangers and Multiphase CFD

#### 1.1 Introduction to the Topic

The global demand for energy continues to rise sharply, driven by rapid urbanization, industrial growth, and the electrification of mobility and manufacturing sectors. In parallel, concerns over climate change and energy security are accelerating the development of next-generation, low-carbon energy systems. Among these, Small Module Reactors (SMR)s have emerged as a promising solution due to their enhanced safety, scalability, and suitability for deployment in remote power grids. These characteristics make SMRs especially attractive for developing countries and for companies with high thermal and electrical energy demands, such as AI-focused firms and data center operators [1,2].

In power plants, heat exchangers play a vital role in thermo-hydraulic efficiency, safety, and performance of the reactor system. Heat exchangers are essential across a wide spectrum of applications, from large-scale power plants to compact thermal management systems in electronics, aerospace, and medical devices. The performance of a heat exchanger is increasingly critical in today's world given the constraints on fossil resources and the need for energy-efficient technologies across industrial sectors.

In recent years, Compact Heat Exchangers (CHE)s (such as plate-fin, plate-and-frame, printed-circuit, microchannel, ...) have attracted significant interest as engineering systems move toward smaller, more efficient designs. Microchannel Heat Exchangers (MCHE)s are a specific type of CHE characterized by very small hydraulic diameters and densely packed channels. Compared to other CHE designs, Microchannel Heat Exchangers (MCHE)s offer higher surface-area-to-volume ratios, which yield superior heat and mass transfer performance. However, their extremely small hydraulic diameters introduce deviated fluid dynamic behavior compared to conventional or even small-channel devices which affects flow regimes, enhances surface tension effects and

leads to higher pressure drops.

Due to the increasing interest in MCHEs, (boiling) two-phase flows in microscale geometries have become a major focus of research. This interest spans across experimental [3–9], analytical [10–14], and numerical studies [15–19], to only cite a few of many. However, modeling two-phase flow in MCHEs remains a challenge due to complex interfacial dynamics, diverse flow regimes, phase changes, and dominant surface tension effects. As said in the previous paragraph, these phenomena often deviate from the behaviors predicted by conventional macro-scale correlations, because of this new physical models are needed which further increases the difficulty of accurately modeling two-phase flow in MCHEs [20].

To address these challenges, Computational Fluid Dynamics (CFD) has become an indispensable tool for developing numerical models of two-phase flow in microchannels, the central focus of this thesis. CFD enables detailed analysis of key hydrodynamic phenomena such as flow behavior and pressure drops, as well as thermodynamic aspects like heat transfer, all under varying geometric and operating conditions. Ultimately, such models can support both the design and optimization of MCHE systems for various applications: from SMRs to air-conditioning and refrigeration systems [21].

#### 1.2 Microchannel Heat Exchangers

The concept of the microchannel heat exchanger was first introduced and demonstrated by Tuckerman and Pease in 1981 [22]. Since then, defining what qualifies as a MCHE has been an important but somewhat ambiguous task. Although the term may appear self-explanatory, there is no universally accepted definition or threshold. Mehendale et al. [23] proposed that any pipe with a hydraulic diameter between 1  $\mu m$  and 100  $\mu m$  should be considered a microchannel. Kandlikar and Grande [24] later raised the upper limit to 200  $\mu m$ , since fabricating channels below 200  $\mu m$  proved very challenging in practice.

Kew and Cornwell [25] introduced a physical criterion called the Confinement Number (Co), defined as:

$$Co = \frac{\sqrt{\sigma / \left[g \left(\rho_L - \rho_G\right)\right]}}{d_i} \tag{1.1}$$

where  $\sigma$  is the surface tension,  $\rho_L$  and  $\rho_G$  are the liquid and gas densities, g is the gravitational acceleration, and  $d_i$  is the channel's inner diameter. The numerator in Equation 1.1 is known as the Laplace diameter (or capillary length), which represents the scale at which surface tension and gravitational forces are balanced.

When the channel diameter becomes comparable to or smaller than  $d_{\rm Laplace}$ , buoyancy-driven motion is suppressed, and surface tension effects dominate characteristic of microscale two-phase flows. For Co > 0.5, heat transfer coefficients begin to deviate significantly from correlations developed for conventional (macro-scale) channels,

signaling the onset of confinement effects such as bubble elongation, film thinning, and enhanced wall interaction, typical of MCHE behavior.

Although the Confinement Number represents a major step forward, it does not account for factors such as surface roughness, surface treatments or coatings, wettability, operating pressure, and local heating conditions. To fully describe an MCHE, these parameters must also be considered when defining and analyzing two-phase flows at the microscale.

MCHEs are becoming increasingly important in both conventional and advanced thermal management systems. As said before, their most significant advantage lies in their exceptionally high surface-area-to-volume ratio, which enables highly efficient heat transfer, particularly in applications involving phase change phenomena such as boiling and condensation. The exploitation of latent heat during these processes allows for thermal performance far beyond that of single-phase systems. Combined with their compact size and ability to handle high heat fluxes, MCHEs are especially well-suited for environments with strict space, weight, and efficiency constraints, such as in SMRs. These benefits can also lead to reductions in overall equipment weight, footprint, and potentially even manufacturing costs. However, the inclusion of phase change processes together with strong surface effects introduces added complexity in both design and numerical modeling.

One of key challenges caused by the complexity is trying to model the internal flow regimes (see Section 1.6) since they are highly sensitive to channel geometry, surface characteristics, and fluid properties. Unlike in conventional or even small-diameter channels, flow regimes in microchannels often deviate significantly due to dominant surface tension forces, enhanced wall effects, and altered interfacial dynamics [26]. A well-known example is the persistence and geometrical configuration of Taylor (slug) flow across a broad range of flow conditions in microchannels, even where annular or churn flow would dominate in larger pipes [27]. These differences complicate regime mapping and require modified criteria compared to classical macroscale flow regime maps. Therefore, modeling these regimes requires a sophisticated understanding of multi-physics interactions at the microscale, which is where advanced CFD tools become critical.

The relevance of MCHEs extends well beyond nuclear applications. In high-performance computing data centers, MCHEs have become integral to sustainable infrastructure, enabling the efficient removal of large thermal loads from densely packed electronic components. In the aerospace industry, reliable thermal management during supersonic flight and satellite operations critically depends on the use of lightweight, compact heat exchangers. Similarly, in chemical microreactors, precise thermal control enabled by MCHEs is vital for achieving optimal reaction rates, selectivity, and energy efficiency. These examples highlight the versatility of MCHEs across sectors where space, efficiency, and control are paramount.

#### 1.3 Multi-phase Computational Fluid Dynamics

Multi-phase CFD is an advanced simulation technique used to analyze the behavior and interaction of multiple fluid phases (typically gas-liquid or two immiscible liquids) within confined geometries. It is based on solving the Navier–Stokes equations together with the continuity and energy equations, extended to account for interfacial dynamics and phase interactions. Depending on the modeling framework, these interactions may be represented using volume-averaged fields for each phase or by explicitly resolving the interface through interface-capturing or interface-tracking methods. Achieving reliable results requires accurate mesh resolution, robust boundary condition implementation, and careful numerical stability control, where surface tension and capillary effects often dominate over inertial forces.

#### 1.3.1 Current State of the Art

State-of-the-art multiphase CFD modeling employs a range of techniques adapted for microchannel contexts but can be categorized into two main classes: *averaging methods* and *interface-resolving methods*.

#### 1.3.1.1 Averaging Methods

Averaging methods are particularly suitable for systems with many dispersed bubbles or droplets where resolving each interface is computationally expensive. They rely on volume-averaged governing equations and are widely used in large-scale industrial simulations.

In the Eulerian–Eulerian approach, which is the model used in this thesis, both phases are treated as interpenetrating continua. Separate sets of volume-averaged mass and momentum conservation equations are solved for each phase. Interfacial forces (such as drag, lift, turbulent dispersion, and wall lubrication) are incorporated through closure relations, making the model's accuracy highly dependent on the quality of these models. This method is particularly advantageous when phase interfaces are not clearly defined in space, as in bubbly or churn flow regimes. In the context of MCHEs, especially for nuclear applications, the Eulerian–Eulerian method has seen increasing adoption due to its scalability and ability to handle complex, multi-channel configurations. A more detailed discussion of the Eulerian–Eulerian model and the treatment of interfacial forces is provided in Section 1.5.

#### 1.3.1.2 Interface-Resolving Methods

Although this thesis focuses on the Euler–Euler approach, it is important to acknowledge the class of *interface-resolving methods*, which are commonly used in microchannel flow regimes such as slug and annular flows, where the interface is of the same scale as the geometry.

These methods aim to directly resolve the interface between two phases and fall into two main categories:

- Interface Capturing Methods: These include the Volume of Fluid (VOF) method, Level-Set method, and Phase-Field method. They solve a single set of governing equations and use a scalar field (such as volume fraction or signed distance function) to capture the interface on a fixed grid.
- Interface Tracking Methods: These rely on a boundary-fitted mesh that moves with the interface, enabling sharp interface resolution but complicating topological changes like coalescence or breakup.

Despite these approaches can offer high resolution of interfacial dynamics, they are not used in this work because of their substantial computational costs and are often limited to small domains and simplified geometries. In contrast, the Euler–Euler framework provides a more computationally efficient approach for simulating large-scale or system-level microchannel flows. Given the scope of this thesis, focused on parametric and model analysis for engineering-scale microchannels to understand thermohydraulic behavior, the Eulerian–Eulerian approach offers the best balance between physical accuracy and computational feasibility. A detailed discussion on the implementation of interface-resolving methods, their challenges, and typical applications is available in the work by Gupta and Deshpande [28].

#### 1.3.2 Challenges with Two-Phase Flow CFD

While CFD provides a powerful tool to explore multi-phase interactions in microscale heat exchangers, it also presents several challenges:

- Surface-to-Volume ratio: Microchannels exhibit a high surface-to-volume ratio, making surface effects and surface forces significantly more influential than in conventional channels. As a result surface force models must be carefully implemented in the governing equations to accurately capture phenomena such as film formation and bubble breakup.
- Mesh Sensitivity: The resolution of interfacial regions, such as the thin liquid film formed during boiling, require fine cells. Studies have shown that the choice of meshing strategy can significantly affect solution accuracy [29]. In two-phase flow there is a trade-off to be made regarding mesh sensitivity. Two incorporate all the surface effects and interfacial forces correctly a fine mesh (especially at the edges) is needed. The trade-off is that a to fine mesh results in unrealistic two-phase flow behavior and/or numerical instability.
- Numerical stability: Numerical instability remains one of the most critical challenges in CFD simulations of two-phase flow. Common issues arise from sharp interface dynamics, "extreme" boundary or initial conditions, abrupt flow regime transitions, and singularities (particularly at gas—liquid—solid contact lines). Some

of many other difficulties include ensuring mass and energy conservation, suppressing non-physical oscillations and handling steep, simulation-induced gradients. These challenges often lead to divergence or unphysical results, necessitating careful mesh refinement, time-step control, and tuning of solver relaxation parameters.

- Model selection challenge: With a wide range of models available for interfacial forces, heat transfer mechanisms, and turbulence closure, selecting the most appropriate combination (and corresponding coefficients) for a given application is a significant challenge. The accuracy and applicability of each model depends heavily on parameters such as flow orientation (horizontal vs. vertical), hydraulic diameter, flow regime, and operating pressure. As no single model currently captures all relevant phenomena across this broad parameter space, careful consolidation of assumptions is required prior to model selection. Consequently, case-specific judgment, calibration, and validation are essential to ensure reliable predictions.
- Heat and Mass Transfer: Modeling heat and mass transfer in two-phase flows is
  inherently complex due to the coupling between fluid dynamics, phase change,
  and interfacial phenomena. This leads to deviations from the saturation temperature, steep gradients and localized phase-change source terms which can introduce significant modeling and numerical challenges [30].

#### 1.4 Scope and Objectives of this Thesis

This thesis aims to develop and validate a robust CFD model capable of accurately simulating two-phase flow and heat transfer in microchannels to identify key thermohydraulic parameters. As said before, modeling two-phase behavior at the microscale introduces significant challenges because of a number of reasons. To tackle these challenges, the thesis adopts a modular, step-by-step modeling strategy. The first objective was developing an adiabatic model to get confident with modeling the interfacial forces of two-phase flow. The aim of this extended model was to be able to produce key fluid-dynamic parameters like void fraction profiles, pressure drops (and an attempt to flow regimes). Thereafter the model was extended to a diabatic model by incorporating boiling and thermal transport. The main objectives of this model was to be able to reproduce key thermo-hydraulic characteristics such as pressure drops, liquid films, ... in microchannels.

Summarized, the global objective is to develop a CFD-based boiling model for single microchannels, which can later be adapted or extended to full MCHE systems for nuclear applications. The primary focus is on accurately understanding and predicting pressure drops, while also capturing other essential thermo-hydraulic parameters such as void fraction and heat transfer rates within individual microchannels.

#### 1.4.1 Research Questions

This thesis is guided by the overarching question: How can a CFD model be developed and validated to accurately simulate two-phase flow and heat transfer behavior to predict key thermo-hydraulic parameters in a single microchannel? Addressing this requires an understanding of the dominant physical mechanisms at play and the ability to reproduce key performance metrics such as pressure drop, void fraction, and heat transfer rate.

One of the first challenges is *identifying and accurately modeling the dominant mechanisms* that govern two-phase microchannel flow. The most dominant mechanisms include: interfacial forces, turbulence and heat transfer but also their underlying parameters and coefficients. Furthermore, an important question is whether existing models can accurately capture these mechanisms within the spatial constraints typical of microchannel applications, such as confined geometries and specific orientations. Many of these submodels were originally developed based on earlier experimental data and theoretical frameworks. Consequently, refinement or recalibration of these models is often required to improve their applicability and accuracy in microchannel flow simulations. *Validation against experimental data presents another layer of complexity.* While several benchmark datasets exist in the literature, they vary significantly in terms of geometry, working fluids, and operating conditions. Notably, most available experimental data (and consequently, many submodels) are based on vertically oriented microchannels. This creates a gap in both experimental benchmarks and validated submodels for horizontal configurations.

Given these challenges, this thesis focuses specifically on developing and validating a diabatic two-phase flow model in single microchannels, with particular emphasis on reproducing and understanding pressure drop behavior. The intent is to establish a reliable modeling framework that can later be extended to full MCHE configurations. To further close the bridge to developing a model for MCHEs improvement should be made in boiling submodels, horizontal interfacial submodels, detailed flow regime prediction and full 3D MCHE geometry implementation.

#### 1.4.2 Modeling Roadmap

The modeling strategy unfolds through a series of progressive phases. First, a thorough literature review (summarized in Section 1.5-Section 1.10) identifies the key two-phase flow phenomena, existing modeling approaches, and available experimental datasets. Building on these insights, specific physical models were selected for testing. Chapter 2 describes the methodology used to test them. In parallel with the literature study, basic CFD skills were developed in STAR-CCM+.

Next, three increasingly sophisticated models (baseline, refined, and boiling) are constructed and validated against experimental data in a graduated manner (Chapter 3). The baseline model implements an Eulerian–Eulerian multiphase formulation to try replicate velocity and void fraction profiles in small channels. The refined model extends this model to microchannel geometries with the main focus on pressure drops

and flow regimes. Lastly, by adding bubble dynamics and vapor generation to capture phase change, the boiling model was developed to evaluate key thermo-hydraulic parameters.

#### 1.5 Theoretical Foundation

To understand the complex behavior of two-phase flow in microchannels, it is essential to first establish a solid theoretical foundation. This section outlines the fundamental modeling framework, including the Eulerian-Eulerian approach, interfacial forces, heat transfer mechanisms, turbulence descriptions and key assumptions used in this work.

#### Important Dimensionless Numbers and Basic Terms

In order to formulate and compare the various interfacial-force, boiling and turbulence closures presented in this work, it is essential to introduce a consistent set of dimensionless numbers and important terms. They will recur throughout the lift, drag, dispersion and lubrication models. Throughout this thesis, subscripts c and d denote the continuous (liquid) and dispersed (bubble) phases, respectively, and universally used symbols  $(\alpha, \rho, \mathbf{u}, D_b)$  will not be redefined after this section.

**Bubble Reynolds number** ( $Re_b$ ): Characterizes the ratio of inertial to viscous forces around a single bubble (comparable to the "standard" Reynolds number but for a specific bubble instead of bulk flow):

$$Re_b = \frac{\rho_c |\mathbf{u}_r| D_b}{\mu_c} \tag{1.2}$$

 $\left[ 
ho_{\it c}: {\it density}, \; D_{\it b}: {\it bubble diameter}, \; \mu_{\it c}: {\it dynamic viscosity} 
ight]$ 

**Eötvös number** (Eo): Measures the ratio of buoyancy to surface-tension forces for a bubble of diameter, used to describe deformation and shape of bubbles:

$$Eo = \frac{g(\rho_c - \rho_d)D_b^2}{\sigma}$$
 (1.3)

 $[g : gravity, \sigma : surface tension]$ 

**Wobble number** (Wo): A turbulence–deformation grouping combining bubble deformability and local unsteadiness:

$$Wo = Eo \cdot \frac{k_c}{|\mathbf{u}_r^2|} \tag{1.4}$$

[k: turbulent kinetic energy]

**Morton number** (Mo): Represents the viscous versus surface tension forces for a single bubble, and is used to select appropriate drag and shape correlations:

$$Mo = \frac{g \,\mu_c^4 \left(\rho_c - \rho_d\right)}{\rho_c^2 \,\sigma^3} \tag{1.5}$$

**Weber Number** (We): the ratio of inertial to surface tension forces, indicating a fluid's ability to deform an interface. It is defined as:

$$We = \frac{\rho u^2 \ell}{\sigma} \tag{1.6}$$

 $[\ell: characteristic length]$ 

**Froude Number** (Fr): the ratio of inertial to external force fields (most often gravity), often used to characterize stratification and phase separation in vertical or inclined flows:

$$Fr = \frac{j}{\sqrt{g\ell}} \tag{1.7}$$

 $[j: superficial velocity, \ell: characteristic length]$ 

**Nusselt Number** (Nu): the ratio of convective to conductive heat transfer at a boundary. It reflects the effectiveness of convective heat transport:

$$Nu = \frac{hD}{\lambda}$$
 (1.8)

 $[h: heat transfer coefficient, \lambda: thermal conductivity]$ 

**Pressure drop** ( $\Delta P$ ): the loss in energy due to friction and interfacial interactions along the flow direction.

$$\Delta P \propto f(\alpha, j_c, j_d)$$
 (1.9)

**Split velocity**  $(u_r)$ : The relative velocity difference between the continuous phase and dispersed phase:

$$\mathbf{u}_r = \mathbf{u}_d - \mathbf{u}_c \tag{1.10}$$

**Void fraction** ( $\alpha$ ): The local volume fraction of the dispersed (gas) phase within a control volume. It ranges from 0 (no bubbles) to 1 (pure gas):

$$\alpha = \frac{V_{\text{gas}}}{V_{\text{total}}} \tag{1.11}$$

**Vapor Quality** ( $\chi$ ): the mass fraction of vapor in a two-phase mixture, used to describe thermodynamic state in boiling or condensation:

$$\chi = \frac{m_d}{m_d + m_c} \tag{1.12}$$

**Bubble diameter** ( $D_b$ ): The bubble diameter is the average diameter of a vapor bubble

calculated using the Sauter Mean Diameter (SMD) method:

$$D_b = \left(\sum_{i=1}^{M} \frac{f_i}{d_i}\right)^{-1} \tag{1.13}$$

[f: fraction of bubble group, M: bubble class]

**Superficial Velocities** ( $j_d$ ,  $j_c$ ): the hypothetical velocity that a single phase would have if it alone occupied the entire cross-sectional area. It is computed by dividing that phase's volumetric flow rate by the total area, implicitly ignoring the presence of any other phase.

$$\tilde{u}_d = \frac{\dot{Q}_d}{\alpha A} = \frac{\langle j_d \rangle}{\alpha} \tag{1.14}$$

$$\tilde{u}_c = \frac{\dot{Q}_c}{(1-\alpha)A} = \frac{\langle j_c \rangle}{(1-\alpha)} \tag{1.15}$$

 $[\dot{Q}_c: \text{volumetric flow}, A: \text{cross section area}]$ 

#### 1.5.1 Eulerian-Eulerian Framework: Adiabatic

In the Eulerian–Eulerian (two-fluid, single flow) framework, both the continuous (liquid) and dispersed (gas) phases are treated as interpenetrating continua. Each phase k is described by its local volume fraction  $\alpha_k$  (with  $\alpha_c + \alpha_d = 1$ ), density  $\rho_k$ , and velocity field  $\mathbf{u}_k$ . Phase interactions appear as source terms in the ensemble-averaged conservation equations [31]. In the case of a dispersed phase, a poly-dispersed flow can be assumed, where multiple bubble size groups (M) are tracked independently.

In this thesis, a **single flow regime model** is developed, based on the assumption that the flow remains within the *annular regime*, which is consistent with the experimental observations used for validation [5]. While this limits the model's applicability across different flow regimes, it allows for targeted calibration and validation within a specific operating range. Future work should extend this framework to include multiple flow regime capabilities, enabling dynamic regime transitions and improved generalization across broader operating conditions.

#### 1.5.1.1 Continuity Equations

The ensemble-averaged mass conservation for the respectively continuous and polydispersed flows (assuming adiabatic and incompressible condition) reads:

$$\frac{\partial}{\partial t} (\rho_c \alpha_c) + \nabla \cdot (\rho_c \alpha_c \mathbf{u}_c) = 0, \tag{1.16}$$

$$\frac{\partial}{\partial t} (\rho_d \alpha_i) + \nabla \cdot (\rho_d \alpha_i \mathbf{u}_d) = S_i^{topo} + S_i^{phase}, \tag{1.17}$$

where:

- $\alpha_i$  denotes the volume fraction of each bubble size group  $(\sum_{i=0}^{M} \alpha_i = \alpha_d)$ ,
- $S_i^{topo}$  is the source term of each bubble size group that accounts for the birth and death of the bubbles caused by break-up coalescence (topological),
- $S_i^{phase}$  accounts for phase change of each bubble size group due to evaporation and condensation.

To track all of the M numbers of bubble size groups, different methods can be used, which will be described in detail in Section 1.9. In this formulation, the continuous and poly-dispersed phases are described separately, but the equations can also be written in a unified form by introducing a generic phase index k, where k = (c, i) denotes the continuous and poly-dispersed phases, which will be done in the momentum and energy conservation equations.

#### 1.5.1.2 Momentum Conservation

The volume-averaged momentum balance for phase k (k = c, i) is written as:

$$\frac{\partial}{\partial t} \left( \rho_k \, \alpha_k \, \mathbf{u}_k \right) + \nabla \cdot \left( \rho_k \, \alpha_k \, \mathbf{u}_k \, \mathbf{u}_k \right) = - \, \alpha_k \, \nabla p + \nabla \cdot \left( \alpha_k \, \mu_k^{\mathrm{eff}} \left( \nabla \mathbf{u}_k + (\nabla \mathbf{u}_k)^T \right) \right) + \alpha_k \, \rho_k \, \mathbf{g} + \mathbf{M}_k, \ (1.18)$$

In this equation,  $\rho_k$  and  $\alpha_k$  denote the density and volume fraction of phase k, respectively; p is the common pressure and g the gravity vector. The term

$$\nabla \cdot \left(\alpha_k \, \mu_k^{\text{eff}} (\nabla \mathbf{u}_k + (\nabla \mathbf{u}_k)^T)\right)$$

represents viscous and (for the liquid) turbulent stresses, with  $\mu_d^{\rm eff} = \mu_d$  (turbulence in the vapor is neglected) and  $\mu_L^{\rm eff} = \mu_L + \mu_L^T$ . Finally,  $\mathbf{M}_k$  accounts for interphase momentum exchange arising interface forces:

$$\mathbf{M}_{k} = \mathbf{F}_{D} + \mathbf{F}_{L} + \mathbf{F}_{VM} + \mathbf{F}_{WL} + \mathbf{F}_{TD}, \tag{1.19}$$

where:

- $\mathbf{F}_D$  is the drag force acting on the dispersed phase,
- $\mathbf{F}_L$  is the lift force due to shear in the continuous phase,
- ullet  $F_{\mathrm{VM}}$  is the virtual-mass force accounting for added-mass effects,
- ullet  ${f F}_{
  m WL}$  is the wall-lubrication force correcting near-wall migration,
- $\bullet$   $\mathbf{F}_{TD}$  is the turbulent-dispersion force due to fluctuations.

These interfacial forces originate from detailed single-bubble studies, but in dense bubbly flows their exact forms and magnitudes are typically chosen empirically and then checked against experiments. It remains difficult to model them mathematically when we must rely on limited bulk data (e.g. pressure drop, average phase fraction) to capture multiple interacting effects. A detailed description of the forces is given in Section 1.7.

#### 1.5.2 Eulerian-Eulerian Framework: Extension to Diabatic

When extending the adiabatic Eulerian–Eulerian two-phase framework to incorporate boiling, several additional effects must be introduced and the governing balance equations augmented accordingly.

**Interphase Mass Transfer:** Liquid evaporates at heated boundaries or within the bulk, creating a vapor source in the gas continuity equation and a corresponding sink in the liquid continuity equation. To mathematically implement this, we introduce the mass transfer rate term  $(\Gamma_c, \Gamma_i \text{ or unified } \Gamma_k)$  to the right hand site of respectively the continuous and dispersed mass conservation equations (Equation 1.16 & Equation 1.17), with:

$$\Gamma_c = -\sum_{i=0}^{M} \Gamma_i \tag{1.20}$$

$$\Gamma_k = \frac{Q_c + Q_d}{h_{fg}} \tag{1.21}$$

Where  $h_{fg}$  is the latent heat of vaporization (or condensation depending on direction) and  $Q_c$ ,  $Q_d$  the heat transfers of respectively the continuous and dispersed side. They can be easily modeled using a general approach through classic heat transfer:

$$Q_k = h_k a_i (T_{Sat} - T_k) \tag{1.22}$$

$$h_k = \frac{Nu_k \ k_k}{d_k} \tag{1.23}$$

where  $h_k$  is the overall heat transfer coefficient and described via appropriate Nusselt number correlation.  $a_i$  is the interfacial area density, which can be calculated via void fraction correlations (symmetric:  $\frac{6\alpha(1-\alpha)}{d}$ , linear:  $\frac{6\alpha}{d}$  or other).

Additionally, the mass transfer rate should also be included in the interphase momentum exchange term ( $\Gamma_k U_k$ ) in Equation 1.18.

**Conservation of Energy:** The energy conservation equation is essential in simulations involving boiling, as it accounts for thermal transport and phase change effects. The source term  $(Q_t)$  typically includes interfacial heat transfer, which drives vapor generation in boiling flows and accounts for latent-heat consumption/production:

$$\frac{\partial}{\partial t}(\alpha_k \rho_k h_k) + \nabla \cdot (\alpha_k \rho_k \mathbf{u}_k h_k) - \nabla \cdot \left(\alpha_k \left(\lambda_k \nabla T_k + \frac{\mu_t}{\sigma_h} \nabla h_k\right)\right) = Q_k \tag{1.24}$$

where:

- *h* is the specific enthalpy,
- $\lambda$  is the thermal conductivity,
- *T* is the temperature,

- $\mu_t$  is the turbulent viscosity,
- $\sigma_h$  is the turbulent Prandtl number for enthalpy,
- $Q_k$  is the source term accounting for interfacial heat transfer.

**Wall Boiling:** In microchannel boiling, the heat transferred from the wall to the fluid occurs through three mechanisms, proposed by Kurul and Podowski [32]. Firstly, where no bubbles are present, heat is conducted directly into the subcooled liquid  $(q_c'')$ . Secondly, at nucleation sites, part of the heat is consumed by vapor generation as bubbles grow  $(q_e'')$ . Lastly, departing bubbles induce local mixing that brings cooler liquid from the bulk into contact with the hot wall, a transient mechanism known as quenching  $(q_e'')$ :

$$q_{tot}^{"} = q_c^{"} + q_e^{"} + q_q^{"} \tag{1.25}$$

In some more recent formulations, a five-term wall boiling model is adopted in place of the traditional three-term approach. In this extended model, the convective heat transfer term  $(q_c)$  is split into two components  $(q_{c,l} \ q_{c,v})$  and weighted by a function of the local void fraction. Additionally, a new contribution is introduced to account for thin-film boiling  $(q_{\text{thinfilm}})$  which becomes significant for high void fraction applications [18].

Despite these advances, the present work adopts the classical three-term model, due to its widespread use and the extensive research supporting its constituent mechanisms. Nevertheless, newer sub-models can incorporate effects such as thin-film boiling implicitly or explicitly through empirical adjustments or wall-function extensions.

Further details on each mechanism and its corresponding model coefficients can be found in Section 1.10.

#### 1.6 Flow Regimes in microchannels

#### 1.6.1 Different flow regimes

In two-phase microchannel flows, distinct spatial configurations of the gas and liquid phases emerge, known as flow regimes. These regimes differ substantially from those observed in conventional channels due to the small hydraulic diameter and dominant surface tension effects (because of the high surface to volume ratio) [3]. Additionally, flow regime behavior in microchannel can vary depending on the The flow regimes are primarily determined by superficial velocities, fluid properties, microchannel geometry but also channel orientation, with horizontal and vertical microchannels exhibiting different regime transitions and stability characteristics.

• **Bubbly flow**: Characterized by small, dispersed bubbles typically at low gas flow rates.

- **Slug** (**Taylor**) **flow**: Larger gas bubbles extend across the almost the entire channel cross-section, separated by a liquid film from the channel edge.
- **Churn flow**: Formed as Taylor bubbles become unstable, with chaotic breakup and recirculation.
- **Annular flow**: Different bubbles coalesce to form a continuous gas core along the center of the tube, while the liquid phase flows as a film along the walls [33].
- **Stratified flow**: Liquid and gas separate into distinct layers, with liquid flowing along the bottom of the channel and gas moving above.

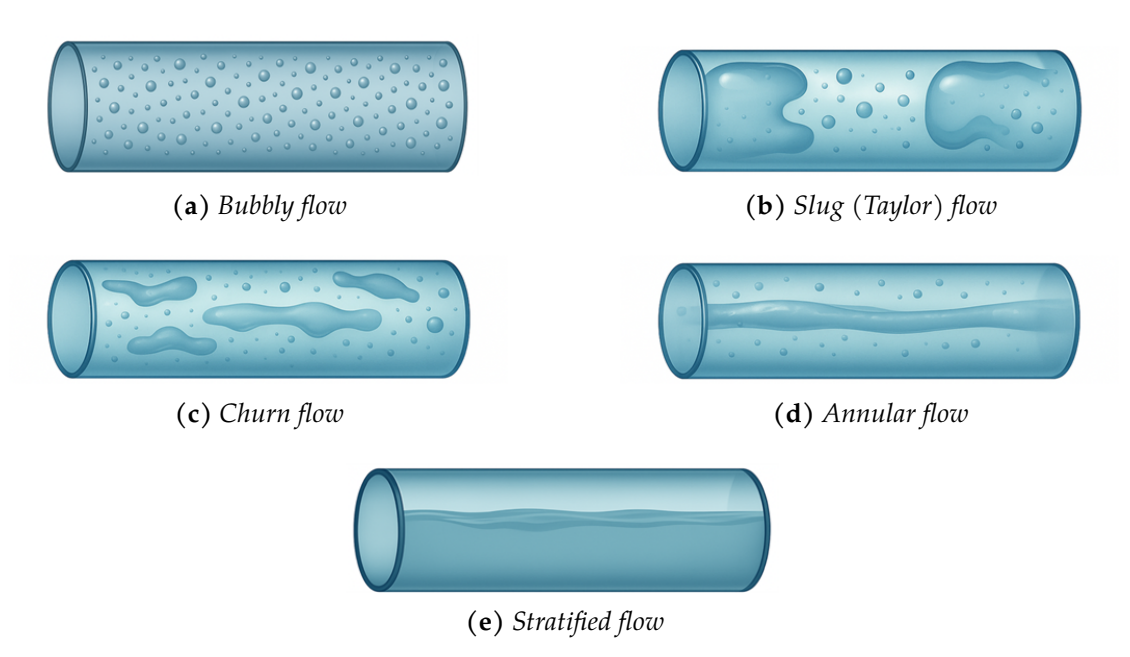


Figure 1.1: Different microchannel two-phase flow regimes

#### 1.6.2 Classification of flow regimes

To classify these regimes, maps using gas and liquid superficial velocities are commonly used. While intuitive, some maps often neglect critical microscale effects like surface tension [34]. A more generalized framework relies on non-dimensional parameters ( $We_c$ ,  $We_d$ ,  $Re_d$ , Eo) that better reflect the balance between inertia, viscosity, surface tension, and buoyancy [28]:

A widely cited map by Akbar et al. employs the continuous and dispersed Weber numbers to delineate regime boundaries [35]. They define transition criteria as:

$${
m We}_d < 0.11 \, {
m We}_c^{0.315}$$
 (Surface tension dominated)  ${
m We}_d > 11 \, {
m We}_c^{0.14}$  (Annular flow region)  ${
m We}_d > 1$ ,  ${
m We}_c > 3$  (Dispersed flow)

The corresponding regime classification and transition boundaries proposed by [35]

are visually illustrated in Figure 1.2, providing a clear overview of the flow behavior across varying inertial and surface tension conditions.

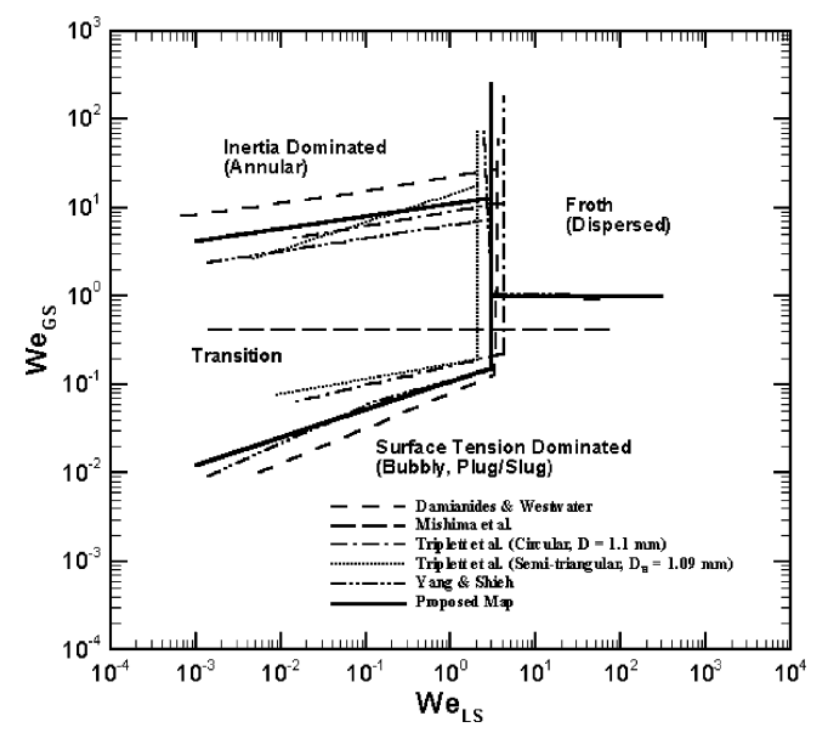


**Figure 1.2:** Flow regime map in We<sub>LS</sub>-We<sub>GS</sub> space with experimental data and regime boundaries

#### 1.6.3 Boiling flow regimes

When boiling occurs, the development of vapor bubbles adds another layer of complexity to flow regime evolution. Initially, nucleate boiling produces isolated bubbles, which coalesce into confined slug or bubbly flows. As heat flux increases, the flow may transition into churn or annular regimes due to vapor expansion and liquid film thinning.

To capture these transitions, Harirchian and Garimella proposed a boiling flow map using compound dimensionless groups that combine thermal and hydrodynamic effects [36].

#### 1.6.4 Challenges in modeling flow regimes

Despite progress in computational methods, accurately modeling flow regimes in microchannels remains a significant challenge in CFD. One of the primary difficulties lies in the inherently dynamic nature of two-phase flows, where multiple regimes can occur and transition within short spatial and temporal scales. Most numerical models are calibrated for a specific flow regime and struggle to capture regime transitions due to limitations in interface capturing methods, closure laws, and mesh resolution. Surface tension, wall adhesion, and microscale interfacial forces play the dominant role in regime formation but are challenging to represent consistently across different regimes. This

makes it difficult to develop a single CFD framework that remains robust and predictive under varying flow conditions. Additionally, experimental data used to validate such models are not always reliable, as visualization techniques provide only a visual representation of the flow. Direct measurements are rarely possible because inserting sensors into microchannels would obstruct the flow and disturb the flow regimes being observed. Even non-intrusive methods are prone to optical distortions, light refraction, and wall effects, all of which introduce uncertainty in identifying and classifying flow regimes.

#### 1.6.5 Analytical and (non-CFD) numerical framework

Beyond experimental observation, flow regimes in microchannels have been investigated through both analytical and numerical modeling. Analytically, simplifications of the Navier–Stokes equations with slip boundary conditions allow first-order approximations of velocity and pressure distributions in long microchannels, particularly for isothermal, incompressible flows at low Reynolds numbers. Numerically, the Lattice Boltzmann Equation (LBE) method has emerged as a powerful kinetic-based approach for simulating microchannel flows. Verhaeghe et al. demonstrated that LBE with multiple relaxation times can accurately resolve pressure-driven slip flows and capture non-continuum effects without relying on artificial slip terms [10]. Their work showed excellent agreement with direct simulation Monte Carlo results in the slip regime, highlighting the LBE's effectiveness where traditional CFD may struggle. However, LBE models with bounce-back boundary conditions were shown to introduce non-physical, viscosity-dependent slip velocities, underlining the need for careful boundary treatment in microscale simulations.

#### 1.7 Two-Phase Flow Interaction Forces

As described in Section 1.5.1.2, the interfacial momentum exchange term  $(M_k)$  plays a crucial role in accurately modeling two-phase flow. This term accounts for the various forces that govern the interaction between the continuous and dispersed phases. The interfacial forces considered in this work and how they are currently modeled are briefly introduced in the following subsections.

#### 1.7.1 Lift Force

#### 1.7.1.1 Physical Background

The lateral (transverse) lift force on a dispersed-phase element (e.g. a spherical bubble or solid particle) in a sheared flow arises from the inertial interaction between the slip velocity and the local fluid vorticity [37–39]. Per unit dispersed-phase volume, it can be written as:

$$\mathbf{F}_L = -C_L \alpha \, \rho_c \, \cdot \mathbf{u}_r \times (\nabla \times \mathbf{u}_c) \tag{1.26}$$

#### where:

- *C*<sub>L</sub> is the lift coefficient, which depends on the size, shape and deformability of the dispersed element (and, in more advanced models, on local turbulence levels),
- $\nabla \times \mathbf{u}_c$  is the vorticity of the continuous phase.

A positive  $C_L$  (typical for small, nearly spherical bubbles in simple shear) drives migration toward regions of lower liquid velocity (e.g. walls in upward flows), whereas a negative  $C_L$  (seen for larger, deformable bubbles) pushes them toward faster-moving regions (e.g. the channel centerline). Typical suggested values of  $C_L$  lies between -0.25 and 0.25 for two phase flow, but the discussion for a specific value remains open in literature [40] [41].

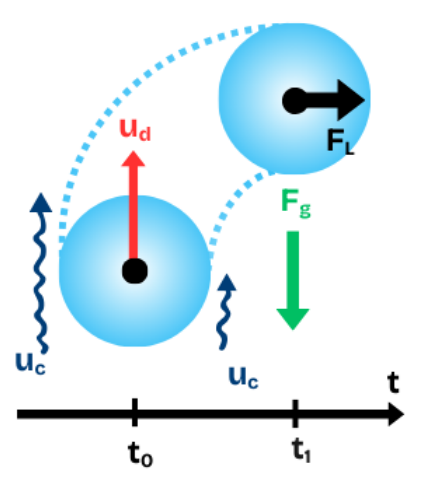


**Figure 1.3:** Schematic of lift-induced lateral migration of a spherical bubble in a wall-bounded shear flow.

In the case of microchannels, the velocity of the continuous phase increases from the wall towards the center. Figure Figure 1.3 illustrates how, in the presence of such a velocity gradient, buoyancy and shear combine to establish a slip velocity which results in a net lateral force on a bubble by the cross–product in Equation 1.26 [42]. This lift force is a key mechanism behind the non-uniform void fraction distributions commonly observed in wall-bounded bubbly flows. Other important contributes are Turbulent Dispersion and Wall Lubrication who will be discussed in Section 1.7.2 and Section 1.7.3. Most classical lift-coefficient models assume a rigid, spherical inclusion in steady, laminar shear and thus neglect three key factors that significantly alter lateral migration in practical two-phase flows: the surface boundary condition (slip vs. no-slip), the bubble's deformation state, and the local turbulence level. Solid particles enforce a no-slip interface, producing strong vorticity and spin effects; spherical bubbles have a shear-free surface that reverses the pressure imbalance; both moderate deformation and unsteady oscillations (enhanced by turbulence) reshape the wake and amplify the lift:

• **Solid particle** ( $C_L < 0$ ): Migration toward the high-velocity side (center).

- **Spherical bubble** ( $C_L > 0$ ): Migration toward the low-velocity side (wall).
- **Deformed bubble** ( $C_L$  < 0): Migration toward the high-velocity side (center). Note that for oscillating bubbles the migration is amplified due to unsteady interface dynamics and vortex-shedding-induced pressure fluctuations, which increase the instantaneous lift magnitude.

Figure 1.4 illustrates how boundary condition, shape, and unsteadiness combine to set the sign and strength of the lateral lift.

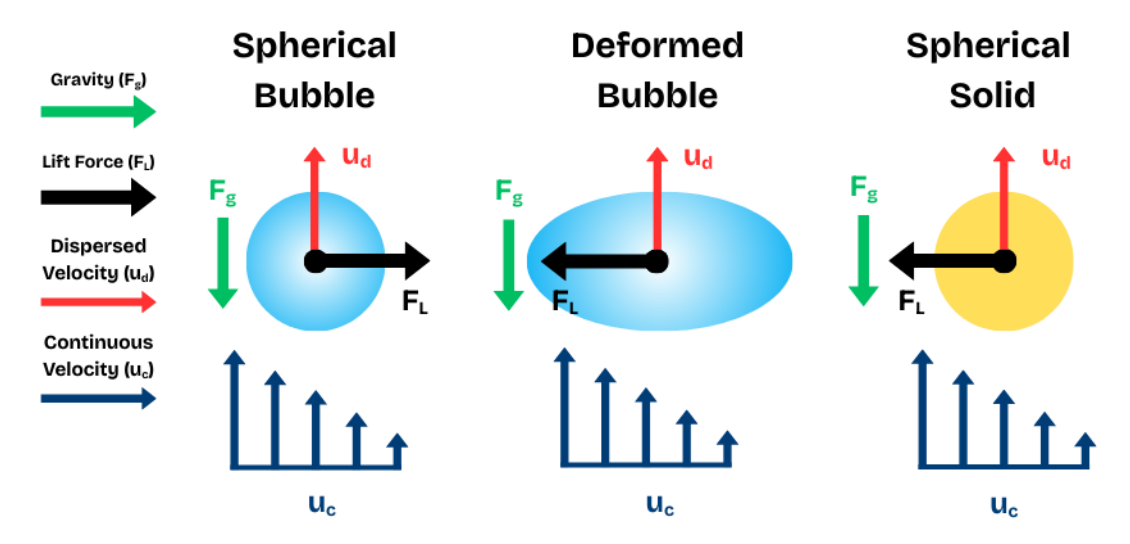


**Figure 1.4:** *Schematic comparison of lift-force direction and sign of*  $C_L$  *for a spherical bubble* (+)*, a deformed bubble* (-) *and a solid particle* (-).

#### 1.7.1.2 Overview of Modeling Approaches

Although a complete prediction of all effects/forces governing lateral migration remains an open challenge, several broad modeling strategies have been developed to estimate the lift on (non-spherical) bubbles and describe their transverse motion:

- Analytical approaches derive closed-form expressions under simplifying limits.
   Classic examples include the early, low-Reynolds-number solutions of Saffman or Legendre & Magnaudet and the high-Reynolds, inviscid-flow result of Auton [42–44].
- Numerical approaches solve the full Navier–Stokes equations in spherical coordinates. Notable studies in this category are those by McLaughlin and by Legendre & Magnaudet, which cover wide ranges of Reynolds number & shear rate and allow for more practical use [42,45].
- Experimental correlations fit lift-coefficient data from controlled shear-flow measurements. The most widely adopted of these is the Tomiyama et al. correlation, which captures both shear-induced and wake-induced contributions [40]. Newer models who also try to include the effect of turbulence but remain open for discussion [46].

# 1.7.2 Turbulent Dispersion Force

## 1.7.2.1 Physical Background

Turbulent dispersion arises because fluctuations in the continuous-phase velocity carry bubbles or particles from regions of high concentration to low concentration, acting as an effective "diffusive" force on the void (or particle) fraction field (Figure 1.5). In fact, virtually all turbulent-dispersion closures share the same constitutive form:

$$\mathbf{F_{TD}} = -C \, \nabla \alpha \tag{1.27}$$

analogous to Fick's law of molecular diffusion or Fourier's law of heat conduction. Along with lift, this diffusive-type force plays a key role in the net lateral migration of the dispersed phase by smoothing concentration peaks and counterbalancing the shear-induced lateral drift [47].

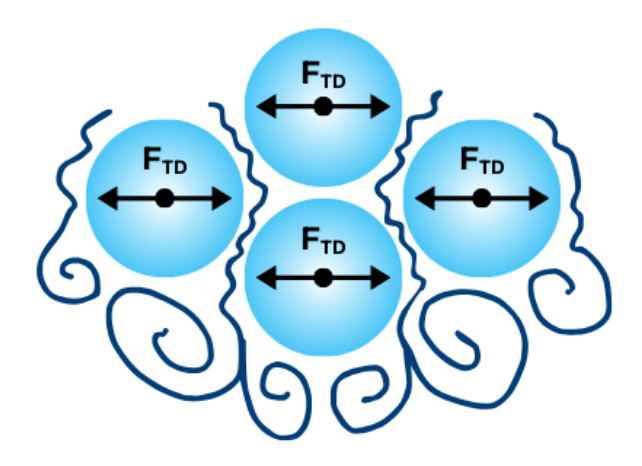


**Figure 1.5:** *Schematic of the turbulent dispersion force acting on neighboring bubbles.* 

## 1.7.2.2 Overview of modeling approaches

Several authors have adopted gradient-based forms  $F_{TD} = -C \nabla \alpha$ , but differ in how C is obtained:

- **Semi-analytical approaches:** Derive *C* by integrating theoretical expressions for drag-fluctuation statistics or bubble-turbulence interactions, like the models of Burns and Lavieville [47,48].
- Favre-Averaged Drag (FAD) closures: Apply density- or volume-fraction-weighted averaging to the instantaneous interphase drag, then close the fluctuation correlations via an eddy-diffusivity hypothesis to recover a Fickian form. Some models used in literature are: the Imperial College Model, the Chalmers University Model, Lopez de Bertodano's Model and Carrica's Model [49–52].

#### 1.7.3 Wall Lubrication Force

#### 1.7.3.1 Physical Background

The wall lubrication force is an additional (artificial) lateral force introduced in bubbly-flow simulations to counteract the tendency of bubbles to accumulate near solid boundaries. Based on early (inaccurate) experiments, it was believed that the force physically arises because of a liquid film between a rising bubble and a no-slip wall which causes difference in liquid and bubble flow rate (as seen of Figure 1.6) [53,54]. This difference creates a hydrodynamic pressure difference across the bubble, producing a net "force" that pushes the bubble away from the wall, which results in a low void fraction near the wall [55]. Without it, classical lift and turbulent dispersion models often predict an unrealistically high void fraction in the near-wall region. Recently newer experiments have shown strong evidence that bubbles can be in contact with the will, postulating that the liquid film is non-existent or negligible [56].

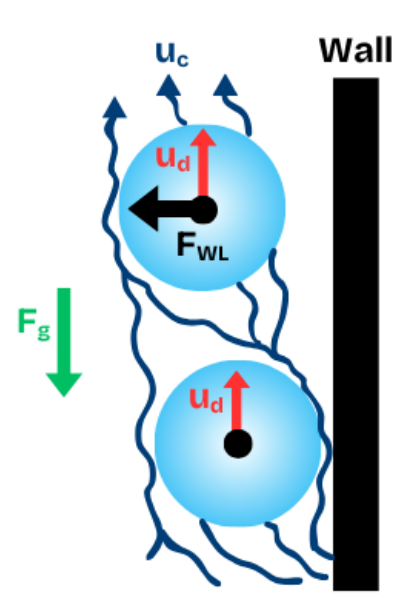


Figure 1.6: Schematic of wall lubrication force

#### 1.7.3.2 Overview of Modeling Approaches

Two main strategies have been adopted in the literature to account for wall lubrication effects in dispersed gas–liquid flows:

• Analytical-Empirical: Derive or postulate an additional lateral force term  $\mathbf{F}_{WL}$  acting on bubbles near solid boundaries. The first (and widely accepted) model was derived by Antal. Later other modified models were derived (more detailed dependencies, but by same hypothesis), becoming more complicated for CFD use [55,57,58]. More recently, Lubchenko proposed a fundamentally new model, he postulates that the near-wall void fraction peak arises from turbulent-dispersion regularization rather than a distinct physical force [59].

• Lift-Force Modification Approaches: Recognize that conventional lift models do not naturally vanish at the wall, and therefore suppress or damp the lift force in a thin near-wall layer, rather than add a separate lubrication term like the approach of Shaver & Podowski [60].

#### 1.7.4 Virtual Mass Force

When bubbles accelerate relative to the surrounding liquid, they must "carry" an added mass of fluid with them, which manifests as an extra inertia term in the momentum balance (see Figure 1.7). In accelerating or swirling bubbly flows, this virtual mass force can be of the same order as drag or lift, influencing bubble trajectories and phase distributions [39]. Numerically, including a virtual mass term often enhances convergence and stability by tempering abrupt changes in relative acceleration, even in flows that appear pseudo-steady. However, its use remains subject to debate: some studies omit it without noticeable loss of accuracy, while others retain it to capture transient acceleration effects.

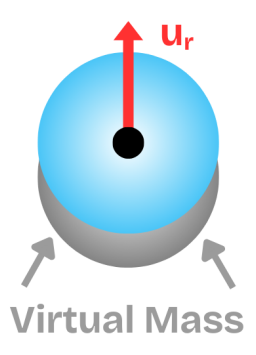


Figure 1.7: Schematic of virtual mass force

#### 1.7.5 Drag Force

#### 1.7.5.1 Physical Background

The drag force arises from the resistance experienced by a bubble moving through the liquid, comprising both viscous drag and pressure-induced drag as seen on Figure 1.8. Per unit dispersed-phase volume, it is expressed as (with  $C_D$  being the drag coefficient):

$$\mathbf{F}_D = -\frac{3}{4} \frac{C_D}{D_b} \alpha_d \rho_c |\mathbf{u}_r| \mathbf{u}_r, \quad \mathbf{u}_r = \mathbf{u}_d - \mathbf{u}_c$$
 (1.28)

The principal challenge in modeling the drag force lies in accurately specifying the drag coefficient  $(C_D)$ . In theory,  $C_D$  can be derived from single-bubble terminal-velocity measurements by equating buoyancy and drag at steady rise speed. More recent correlations augment  $C_D$  with swarm effects to account for neighbor-induced interactions.

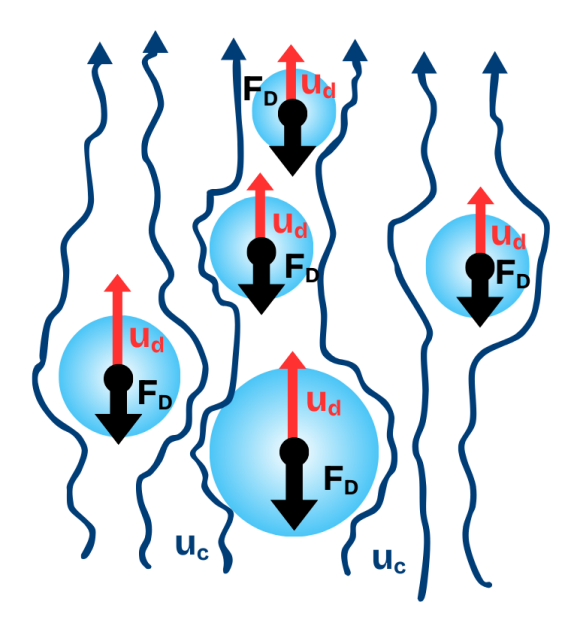


**Figure 1.8:** *Schematic of drag force (with bubble swarm)* 

## 1.7.5.2 Overview of Modeling Approaches

Two broad strategies have been used to model  $C_D$ , both of them are analytical-experimental methods:

- **Single Bubble Correlations:** Correlations are derived from theoretical limits, terminal-velocity studies, pressure drop-studies and single-bubble curve-fitting experiments. Key examples include of this approach are Schiller-Naumann, Tomiyama, Ishii–Zuber and Kendoush [61–64].
- Swarm and Turbulence Corrections: Modifications to single-bubble  $C_D$  to account for group effects (swarm), deformation and turbulence. Most notable developments are Bozzano–Dente, Wen-Yu, Gidaspow [65–67].

It is important to note most drag coefficients are tuned for specific regimes: e.g. Schiller–Naumann for isolated, small-bubble Stokes flows, Ergun and Wen–Yu for packed or fluidized beds, Kendoush for taylor bubbles and so on. Therefore, selecting the appropriate correlation for the expected flow regime is critical for robust CFD predictions. However it has been observed been several studies that the influence of the drag coefficient doesn't have much effect for bubbly flows (which togheter with annular works best in boiling simulations) [68,69].

#### 1.7.6 Basset (History) Force

The Basset force accounts for the temporal lag in the development of the viscous boundary layer around a particle when the relative velocity varies with time. It represents the accumulated effect of past accelerations on the instantaneous hydrodynamic force. In this work, the Basset force is neglected because, under our flow conditions, its contribution is orders of magnitude smaller than the other forces.

# 1.8 Turbulence Modeling in Multiphase Flows

Accurate turbulence modeling is essential in the simulation of multiphase flows, particularly in bubbly and boiling systems where phase interactions alter the flow dynamics profoundly. Since the direct solution of the Navier-Stokes equations via Direct Numerical Simulation (DNS) is computationally prohibitive for most engineering applications, turbulence models are required to close the Reynolds-averaged Navier-Stokes equations (RANS).

The RANS framework offers a practical approach to model turbulent flows by decomposing instantaneous flow variables (such as velocity and pressure) into mean and fluctuating components ( $u = \overline{u} + u'$  and  $p = \overline{p} + p'$ ). By averaging the Navier–Stokes equations in time, the RANS formulation results in governing equations for the mean flow (which has the same form as the multiphase equations since they are also averaged equations (see Equation 1.18)). However, this process introduces an additional term called the Reynolds stress tensor:

$$\tau_k^t = -\rho \overline{u_i' u_j'} \tag{1.29}$$

The Reynolds stress tensor poses the turbulence closure problem, since there are now more unknowns than equations. Although one could attempt to derive transport equations for each of the six independent Reynolds stress components, doing so introduces even more unknown quantities. Instead, a pragmatic solution (first proposed by Boussinesq in 1877) is to relate the Reynolds stresses to the mean rate of strain via an eddy-viscosity hypothesis:

$$\tau_k^t = \mu_t \left( \frac{\partial \overline{u}_i}{\partial x_i} + \frac{\partial \overline{u}_j}{\partial x_i} \right) \tag{1.30}$$

This reduces the problem to finding a reliable expression for the turbulent viscosity  $(\mu_t)$ . Two widely used approaches to achieve this are the so-called *two-equation models*, which introduce transport equations for two turbulence quantities. The most established models in this category are the  $k-\varepsilon$  and the  $k-\omega$  models.

#### **1.8.1** $k - \varepsilon$ Model

The standard  $k-\varepsilon$  model uses the turbulent kinetic energy (k) and its dissipation rate  $(\varepsilon)$  to calculate the turbulence viscosity. It is known for its robustness in fully turbulent flows, particularly in high-Reynolds number regimes. The  $k-\varepsilon$  model performs well in free-shear flows but struggles near walls, requiring wall functions or damping modifications. The widely used model proposed by Launder and Spalding is formulated as following for the continous phase [70]:

$$\mu_t^c = \rho_c C_\mu \frac{k_c^2}{\varepsilon} \tag{1.31}$$

$$\frac{\partial}{\partial t} \alpha_c \rho_c k + \nabla \cdot \alpha_c \rho_c \mathbf{u}_c k = \nabla \cdot \left( \frac{\alpha_c (\mu_c + \mu_t^c)}{\sigma_k} \nabla k \right) + \alpha_c \left( P - \rho_c \varepsilon \right)$$
(1.32)

$$\frac{\partial}{\partial t} \alpha_c \rho_c \varepsilon + \nabla \cdot \alpha_c \rho_c \mathbf{u}_c \varepsilon = \nabla \cdot \left( \frac{\alpha_c (\mu_c + \mu_t^c)}{\sigma_\varepsilon} \nabla \varepsilon \right) + \alpha_c \frac{\varepsilon}{k} \left( C_{\epsilon 1} P - C_{\epsilon 2} \rho_c \varepsilon \right)$$
(1.33)

Standard constants:  $\left[C_{\mu} = 0.09, \ \sigma_k = 1.0, \ \sigma_{\varepsilon} = 1.3, \ C_{\varepsilon 1} = 1.44, \ C_{\varepsilon 2} = 1.92\right]$ 

#### **1.8.2** $k - \omega$ **Model**

The  $k-\omega$  model substitutes the dissipation rate  $(\varepsilon)$  with the specific dissipation rate  $(\omega = \varepsilon/(\beta^*k))$ , resulting in better near-wall accuracy and improved performance in adverse pressure gradients. The  $k-\omega$  model is therefore particularly effective for wall-bounded flows and regions with high strain rates or separation. However, it can be overly sensitive to freestream values of  $\omega$ , which led to the development of the  $k-\omega$  SST model. It can be mathematically modeled as [71]:

$$\mu_t = \rho \frac{k}{\omega} \tag{1.34}$$

$$\frac{\partial}{\partial t} \left( \alpha_c \rho_c k \right) + \nabla \cdot \left( \alpha_c \rho_c \mathbf{u}_c k \right) = \nabla \cdot \left( \frac{\alpha_c (\mu_c + \mu_t^c)}{\sigma_b^\omega} \nabla k \right) + \alpha_c \rho_c P_k - \alpha_c \rho_c \beta^* k \omega \tag{1.35}$$

$$\frac{\partial}{\partial t} \left( \alpha_c \rho_c \omega \right) + \nabla \cdot \left( \alpha_c \rho_c \mathbf{u}_c \omega \right) = \nabla \cdot \left( \frac{\alpha_c (\mu_c + \mu_t^c)}{\sigma_\omega^\omega} \nabla \omega \right) + \alpha_c \rho_c \alpha \frac{\omega}{k} P_k - \alpha_c \rho_c \beta \omega^2$$
 (1.36)

Standard constants:  $[\alpha = 5/9, \beta = 3/40, \beta^* = 9/100, \sigma_k = 2.0, \sigma_{\omega} = 2.0]$ 

# 1.8.3 Application in Multiphase Flows

In the Eulerian-Eulerian multiphase framework, turbulence is typically modeled only for the continuous phase. The dispersed phase is assumed to behave in a laminar fashion, but its influence on the continuous-phase turbulence is not neglected. Turbulence from the dispersed phase can be taken into account using bubble-induced turbulence models. In this approach, additional source terms  $(S_k, S_{\varepsilon}, \text{ or } S_{\omega})$  are introduced on the right-hand side of the turbulence transport equations to account for energy transfer from dispersed phase motion. One first and most used BIT models is Sato's eddy viscosity model, but many other formulations models exist today [72].

#### 1.8.4 Wall Treatment and Considerations

An important parameter in turbulence modeling near solid boundaries is the nondimensional wall distance  $(y^+)$  which guides how the mesh resolves the near-wall flow region. It determines the suitability of wall treatment approaches and is especially relevant for capturing momentum and heat transfer accurately in high-gradient boundary layers.

In turbulent flows, resolving the near-wall region accurately is critical for predicting heat transfer and phase interactions. The non-dimensional wall distance  $y^+$  is defined as:

$$y^+ = \frac{u_\tau y}{v}$$

where  $u_{\tau}$  is the friction velocity, y is the distance to the wall, and v is the kinematic viscosity. This parameter indicates the location of the first mesh node relative to the viscous sub-layers of the boundary layer.

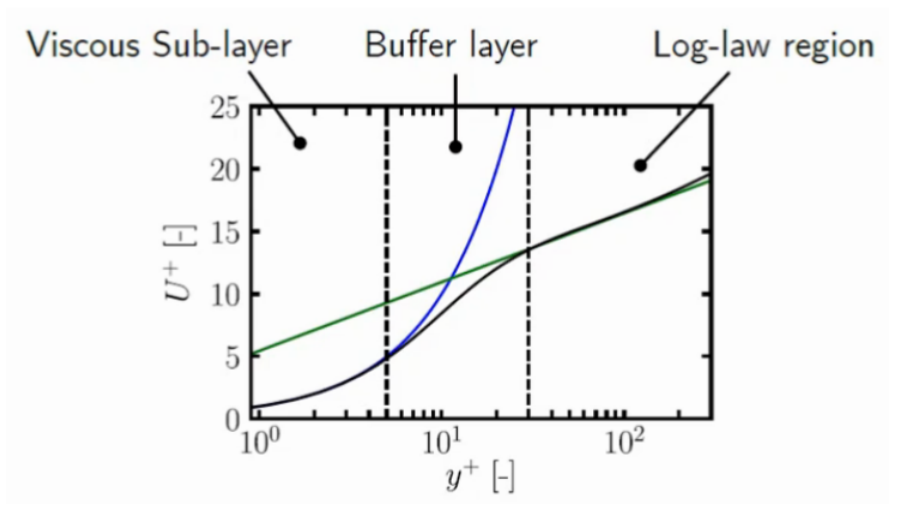


**Figure 1.9:** Typical  $y^+$  zones and corresponding turbulence modeling strategies. The high- $y^+$  (log-law) region used in this study is compatible with standard wall functions and avoids the need for resolving the viscous sublayer.

# 1.9 Bubble Size Grouping & Interfacial Area

In gas-liquid multiphase flows, the prediction of the previously discussed interfacial dynamics depends on the bubble size distribution. In early CFD formulations, bubbles were assumed to be of uniform size, a simplification that fails in real-world applications involving previously discussed coalescence, breakup, or wide void fraction ranges. Hence, modeling the bubble population's size evolution is essential.

# 1.9.1 Population Balance Models & MUSIG

The first major improvement was the Multiple size group (MUSIG) model, which introduced a discrete binning approach to track the evolution of bubble size classes. It was developed by Lo in 1996 and later extended to account for inhomogeneous velocity fields (iMUSIG) [73]. The model solves a separate continuity equation for each bubble

class, capturing inter-group mass transfer via breakup and coalescence source terms derived from the population balance equation:

$$\frac{Dn_i}{Dt} = B_{br,i} + B_{cl,i} - D_{br,i} - D_{cl,i}$$
 (1.37)

While MUSIG offers good fidelity, especially in low void fraction bubbly flows, it suffers from high computational cost due to the number of additional equations required.

# **1.9.2** Method of Moments & S- $\gamma$

A more efficient alternative to MUSIG is the Methods of Moments (MOM), initially proposed by Hulburt and Katz and later adapted for two-phase CFD under the S- $\gamma$  framework [74,75]. Instead of tracking discrete groups, MOM reformulates the population balance in terms of low-order statistical moments ( $S_{\gamma}$ ) of the size distribution (P(d)), such as:

$$S_0 = \int_0^\infty n(d) \, dd \qquad \qquad \text{(number density)} \tag{1.38}$$

$$S_2 = \int_0^\infty d^2 n(d) dd \qquad \text{(interfacial area)} \tag{1.39}$$

$$S_3 = \int_0^\infty d^3 n(d) dd \qquad \text{(void fraction)} \tag{1.40}$$

The third moment  $S_3$  is directly related to the void fraction  $(\alpha)$ , while the second moment  $S_2$  is linked to the interfacial area density  $(a_i)$ . This approach drastically reduces computational cost while retaining sufficient physical detail for engineering analysis. STAR-CCM+ adopts the S- $\gamma$  method by default to compute interfacial area dynamics within the Eulerian–Eulerian framework.

# 1.9.3 Sauter Mean Diameter

In general, a mean diameter  $d_{pq}$  is defined as the ratio of the  $p^{th}$  and  $q^{th}$  order moments of the distribution:

$$d_{pq} = \left(\frac{\int_0^\infty d^p P(d) \, dd}{\int_0^\infty d^q P(d) \, dd}\right)^{\frac{1}{p-q}} = \left(\frac{S_p}{S_q}\right)^{\frac{1}{p-q}}$$
(1.41)

Different combinations of p and q yield different characteristic diameters. For example:

- $d_{10} = \frac{S_1}{S_0}$ : number-averaged diameter,
- $d_{43} = \frac{\tilde{S}_4^0}{\tilde{S}_3^2}$ : volume-weighted average diameter,
- $d_{32} = \frac{S_3}{S_2}$ : surface-volume ratio diameter, also known as the SMD.

The SMD is especially relevant in multiphase flow modeling because it represents the diameter of a monodisperse bubble population that would yield the same surface-area-

1.10. Wall Boiling

to-volume ratio as the polydisperse mixture. Once the interfacial area density  $a_i$  and the dispersed phase volume fraction  $\alpha_d$  are known, the SMD can be calculated via:

$$D_{32} = \frac{6\alpha_d}{a_i} = \frac{6S_3}{S_2} = 6 \cdot \frac{n \int_0^\infty d^3 P(d) \, dd}{n \int_0^\infty d^2 P(d) \, dd}$$
(1.42)

This mean diameter is critical in interfacial closure models as it affects drag calculations, heat and mass transfer rates, and the estimation of bubble-induced turbulence. Since both  $S_2$  (related to interfacial area) and  $S_3$  (related to volume fraction) are computed or transported in S- $\gamma$  models, the SMD naturally emerges as a key post-processed quantity for coupling with closure correlations.

# 1.10 Wall Boiling

As shortly described in paragraph 1.5.2, the wall boiling model decomposes the total heat transfer at the heated surface into three separate contributions. Each term is associated with a distinct physical mechanism and depends on both thermal conditions and bubble dynamics. The corresponding expressions used in the implemented model are given below.

#### 1.10.1 Convective Heat Transfer

Convective heat transfer is the most intuitive and easily understood mechanism in the wall boiling model. It represents the heat exchanged between the heated surface and the surrounding liquid in regions not influenced by nucleating bubbles. Much like heating water on a stove, thermal energy is transferred from the wall into the liquid through a combination of conduction and fluid motion. Figure 1.10 illustrates this mechanism schematically. The convective contribution depends strongly on local flow properties, including turbulence intensity, liquid velocity, and thermal boundary layer development. It is commonly modeled using a classical heat transfer relation:

$$q_c'' = A_c h_e \cdot (T_w - T_c) \tag{1.43}$$

where  $A_c$  is the effective wall area participating in single-phase convection,  $h_e$  is the convective heat transfer coefficient and  $T_w - T_c$  is the temperature difference between the heated wall and the adjacent liquid.

## 1.10.2 Evaporative Heat Transfer

This term models the latent heat transfer resulting from phase change during bubble growth. As vapor bubbles form and expand at the heated wall, liquid is locally evaporated into vapor, carrying away a significant amount of thermal energy. Figure 1.11

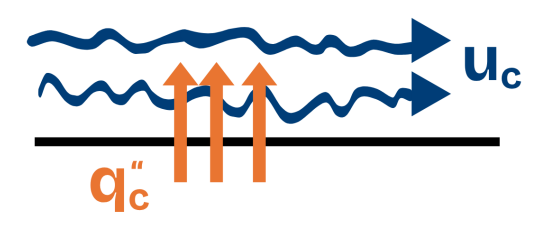


**Figure 1.10:** *Schematic of single-phase convective heat transfer from the wall to the continuous liquid phase.* 

illustrates how this mechanism contributes to wall heat removal during nucleate boiling.

Evaporative heat transfer is primarily governed by three key parameters: the active nucleation site density  $(N_a)$ , the bubble departure diameter  $(D_b)$ , and the bubble departure frequency (f). These parameters are central to modeling heat exchange in MCHEs, where surface interactions and microscale bubble dynamics dominate the boiling process. The evaporation heat flux can be modeled as [76]:

$$q_e'' = \frac{\pi}{6} D_b^3 h_{f,d} \rho_d f N_a \tag{1.44}$$

where:

- *f* is the bubble departure frequency,
- $D_b$  is the bubble departure diameter (it defines the size of a vapor bubble at the moment it detaches from the heated wall surface),
- $h_{fg}$  is the latent heat of vaporization,
- $N_a$  is the nucleation site density which controls the number of active nucleation sites per unit area.

Given the critical role of these parameters in determining evaporation rates, it is essential to model them as accurately as possible, despite the significant challenges involved in their estimation and validation.

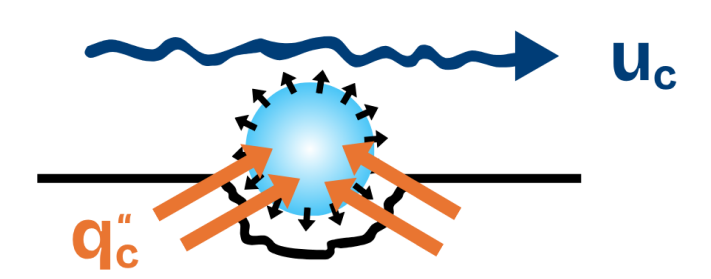


**Figure 1.11:** Schematic representation of evaporative heat transfer from the wall to a growing vapor bubble.

1.10. Wall Boiling

# 1.10.3 Quenching Heat Transfer

Quenching occurs when a vapor bubble detaches from the heated wall, momentarily exposing a dry spot. Cold liquid from the surrounding region then rushes in to re-wet this area. Due to the large temperature difference between the wall and the incoming liquid, this re-wetting event triggers a sharp, transient heat conduction pulse. Although highly localized and short-lived, such events occur frequently and contribute significantly to the total wall heat flux. Figure 1.12 illustrates this mechanism and the associated thermal response near the wall. The quenching heat flux is classically modeled as:

$$q_g^{\prime\prime} = A_e h_g \cdot (T_w - T_c) \tag{1.45}$$

Here,  $A_e$  is the effective two-phase area undergoing transient evaporation, and  $h_q$  is the quenching heat transfer coefficient, which is typically related to the bubble departure frequency (f), which self explanatory defines how frequently bubbles detach from active nucleation sites. Since the total wall area is shared between convection and quenching mechanisms, a logical constraint is applied:  $A_e + A_c = 1$ , where  $A_c$  represents the area available for single-phase convection. It is important to note that  $A_e$  is strongly dependent on the number of nucleation site density and mean departure diameter of bubbles and should therefore be modeled accordingly [77,78].

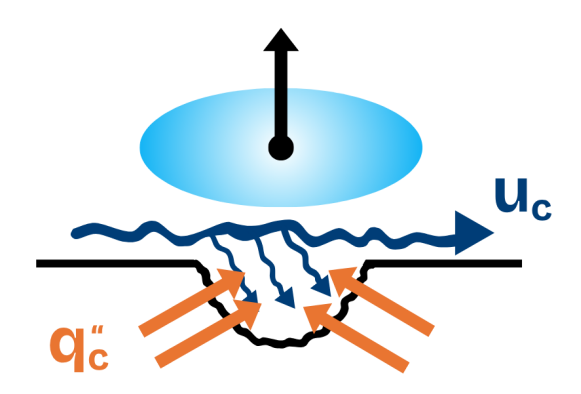


Figure 1.12: Schematic representation of quenching heat transfer.

#### 1.10.4 Modeling Strategies

Widely accepted wall boiling models—such as Cole (for departure frequency f), Hibiki (for nucleation site density  $N_a$ ), Kocamustafaogullari (for departure diameter  $D_b$ ), Kurul–Podowski (for evaporation area  $A_e$ ), and Del Valle–Kenning (for quenching coefficient  $h_q$ ) provide semi-empirical formulations based on pool boiling experiments and mechanistic assumptions [32,76–82]. These models established the foundational concept of heat flux partitioning and established widely used correlations for nucleation parameters and area weighting functions.

Recent research has shown that merely replacing these classical correlations with improved submodels does not necessarily lead to more accurate simulations. This is primarily due to the lack of mechanistic fidelity in how bubble dynamics, sliding motion, microlayer evaporation, and wall re-wetting are treated [83].

To address these limitations, a fundamentally new class of boiling models has emerged. These models propose a more physically consistent and self-contained framework (see Figure 1.13) based on five core enhancements:

- 1. Mechanistic prediction of both bubble departure  $(D_b)$  and lift-off diameters  $(D_l)$ .
- 2. Modeling of microlayer evaporation during both stationary and sliding phases.
- 3. Inclusion of sliding bubble heat transfer & effect on boundary layer regeneration.
- 4. Realistic treatment of nucleation site (de)activation and spatial interaction.
- 5. Accounting for bubble interactions on the surface.

Developed using high-resolution experimental data and validated against multiple test cases, these models demonstrate significantly improved generality and predictive performance across a wide range of flow conditions. Their integration into Eulerian–Eulerian multiphase CFD solvers enables better resolution of local heat fluxes and phase dynamics, offering a promising path forward for high-fidelity boiling simulations in nuclear and microscale thermal systems [84,85].

Figure 1.13 illustrates the conceptual structure of the complete and self-consistent wall boiling framework. Each node represents a physical mechanism or parameter involved in boiling heat transfer. The arrows indicate dependencies, highlighting how dynamic interactions like bubble growth, sliding, and growth influence both heat partitioning and surface behavior [86]. The diagram is adapted from lecture materials on the GEN-II boiling framework presented at MIT [86].

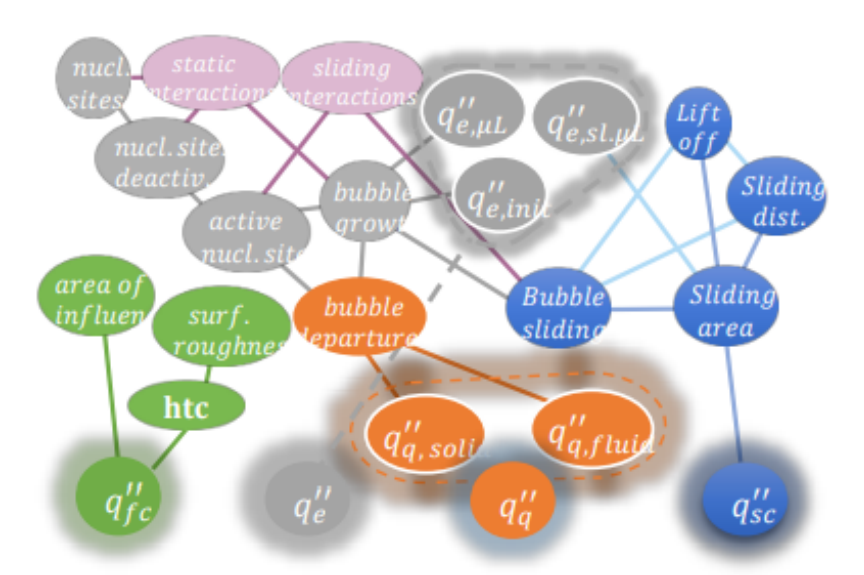


**Figure 1.13:** Conceptual representation of the complete and self-consistent wall boiling framework, illustrating the interdependencies between nucleation, sliding, evaporation, and quenching mechanisms.

# Materials and Methods

This chapter outlines the computational strategies, modeling assumptions, and validation workflow adopted to simulate two-phase and boiling flow phenomena in microchannels. As previously mentioned, all simulations were performed using STAR-CCM+, employing the Eulerian–Eulerian two-fluid framework enriched with interfacial force models, turbulence closures, and wall boiling correlations where applicable. To ensure physical robustness and numerical stability before applying the models to the full complex geometry, a stepwise testing approach was adopted. Each stage was inspired by relevant experimental and/or numerical studies from the literature and served as a validation benchmark:

- **Baseline Model:** A straight vertical pipe with a diameter of 50.3 mm was used as the initial test case, inspired by the experimental work of Kocamustafaogullari and the numerical studies of Ekambara et al [15,87]. It served as a foundation to evaluate the stability and basic behavior of the multiphase solver.
- Refined Model: The validated baseline setup was then extended to a mixing pipe geometry, closely following the widely studied configuration from Triplett et al. with a channel diameter of 1.1 mm [3]. This geometry introduced complex inlet and development effects, providing a more realistic test environment to evaluate the model's predictive capability in capturing interface dynamics, flow regimes, and pressure drops.
- **Boiling Model:** In the final phase, the model was further extended to include wall heating and boiling phenomena. This was based on the experimental configuration studied by Sumith et al., which featured a microchannel diameter of 1.45 mm and aligned well with the annular flow regime targeted in this thesis while avoiding excessively high flow velocities [5].

Each simulation stage is discussed in detail in the following sections, including geometry setup, meshing strategies, boundary conditions, numerical schemes, and physical model settings. The source code for custom field function implementations and modeling logic is provided in Appendix A.

## 2.1 Baseline model

# 2.1.1 Geometry and mesh

The geometry used in the baseline model was based on the experimental setup by Kocamustafaogullari, featuring a horizontal pipe with an internal diameter of 50.3 mm [87]. To match the numerical configuration studied by Ekambara et al., a total pipe length of 9000 mm was adopted, ensuring full development of the two-phase flow [15]. Two different meshing strategies were considered (see Figure 2.1): a directed auto mesh using quadrilateral cells, and a more refined directed patch mesh employing a butterfly-type surface topology. The mesh settings used for each case are summarized in Table 2.1.

**Table 2.1:** Overview of mesh types and controls used for the baseline model.

Mesh Type	Meshers	Base Size (mm)	Layers
Directed Mesh	Auto (Quadrilateral)	2.0	100
Directed Mesh	Patched (Butterfly)	1.0 (10*)	100

<sup>\*</sup>Geometric divisions from wall edge to center

Initial tests showed that both meshing strategies yielded comparable stability and runtime performance. However, due to its superior surface resolution and more structured alignment with boundary layer gradients, the patched (butterfly) mesh was selected for all subsequent model development. This choice is supported in literature as a good practice for stratified and annular two-phase flow modeling in large pipes [29]. A mesh sensitivity analysis was performed to confirm this assumption and is presented in Section 3.1.2.5.

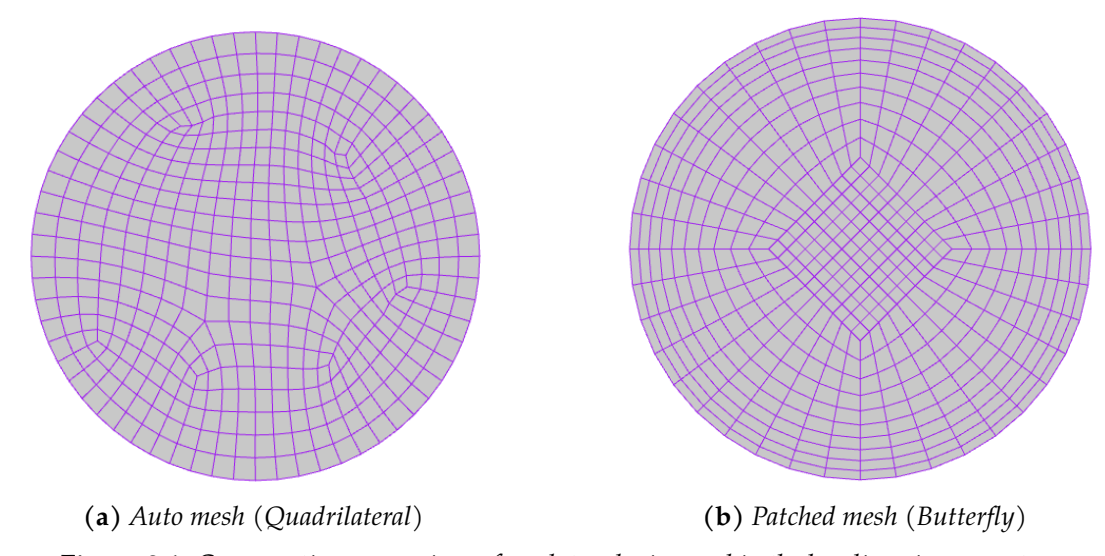


**Figure 2.1:** Cross-section comparison of mesh topologies used in the baseline pipe geometry.

2.1. Baseline model 33

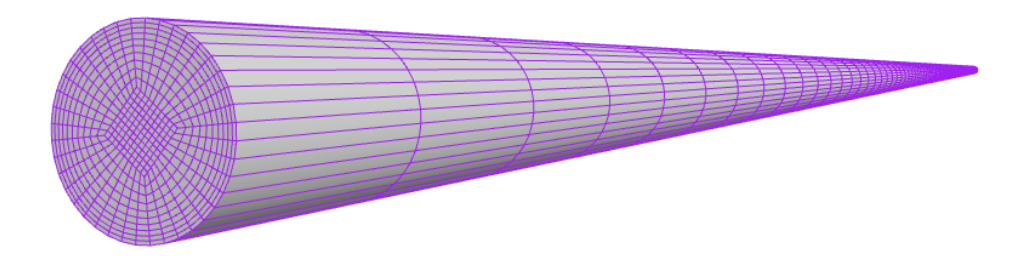


**Figure 2.2:** *Full view of the patched (butterfly) mesh applied to the 9-meter baseline pipe.* 

# 2.1.2 Physics Models

Table 2.2 shows the selected physical models for interfacial forces and turbulence together with their associated coefficients that resulted in the best agreement with experimental data for the baseline model [87]. The models themselves, along with the rationale behind their choice, are described in detail in Section 2.1.2.1-Section 2.1.2.5.

		•
Interfacial Force	Model	Coefficient(s)
Lift	Sugrue	_
Turbulent Dispersion	Lopez de Bertodano	$C_{TD} = 0.80 - 0.85$
Wall Lubrication	Antal et al.	$C_1 = -0.01, C_2 = 0.05$
Drag	Tomiyama	Intermediate contamination
Virtual Mass	Zuber	Spherical particle ( $C_{VM} = 0.5$ )

**Table 2.2:** Overview of all models used for the baseline model.

#### 2.1.2.1 Lift Force: Sugrue

Although the Tomiyama lift formulation is widely adopted in two-phase CFD, an alternative model was selected in this work [40]. Hibiki et al. demonstrated that turbulence can cause lift coefficient sign inversion at  $Eo\approx2.25$ , much earlier than the classical threshold of Eo=5–6, highlighting the limitations of shape-based criteria alone [88]. This insight motivated the use of the Sugrue model, which incorporates both bubble deformation (via the Eötvös number) together with local turbulence deformation effects through the Wobble number (Wo) to better capture lift behavior across flow regimes. The Hibiki model was also considered, but due to its limited validation range  $(3.68 < Re_b < 78.8)$ , it was ultimately not adopted [88]. By contrast, Sugrue's model offers a continuous, empirically calibrated lift formulation that remains applicable in the turbulent, transitional, and small-scale regimes relevant to this study [46]. Sugrue's formulation expresses the lift coefficient as a product of two empirical functions: one dependent on the Wobble number (Wo), and one on the void fraction  $(\alpha)$ :

$$C_L = f(Wo) \times f(\alpha)$$
 (2.1)

$$f(\text{Wo}) = \min \left[ 0.03, 5.0404 - 5.0781 \,\text{Wo}^{0.0108} \right]$$
 (2.2)

$$f(\alpha) = 1.0155 - 0.0154 \exp(8.0506 \alpha) \tag{2.3}$$

The two calibration functions are derived by brute-force optimization against the turbulent bubbly-flow data of Hibiki et al. By construction, f(Wo) captures the lift-inversion behavior under increasing turbulence (higher Wo reduces  $C_L$ ), while  $f(\alpha)$  attenuates the coefficient in dense bubbly flows.

Figure 2.3 visualises the difference between the Sugrue model used in this work and the widely adopted Tomiyama correlation [40,46]. Tomiyama's model exhibits a constant positive lift coefficient of  $C_L = 0.288$  for nearly spherical bubbles at low Eötvös numbers (Eo < 4), after which the lift force sharply transitions to negative values and continues decreasing until saturating at  $C_L \approx -0.27$  for Eo > 10. This abrupt sign change reflects the onset of strong bubble deformation, where the lift force reverses direction and drives bubbles toward the wall rather than the center.

In contrast, the Sugrue model provides a smoother, continuous transition in  $C_L$  as a function of Eo by incorporating the Wobble (Wo) number, which accounts for both Eötvös number and relative velocity. For typical values ( $u_{\rm rel}^2=1.5,\,k=1.1$ ), the lift coefficient starts at a fixed 0.03 for nearly spherical bubbles and becomes negative relatively quickly due to the local unsteadiness of the bubble. This behavior results in more gradual and velocity-sensitive lift force behavior, which can be particularly relevant in unsteady or microchannel flows where traditional models like Tomiyama's may overpredict the lift force magnitude or misrepresent transition regimes.

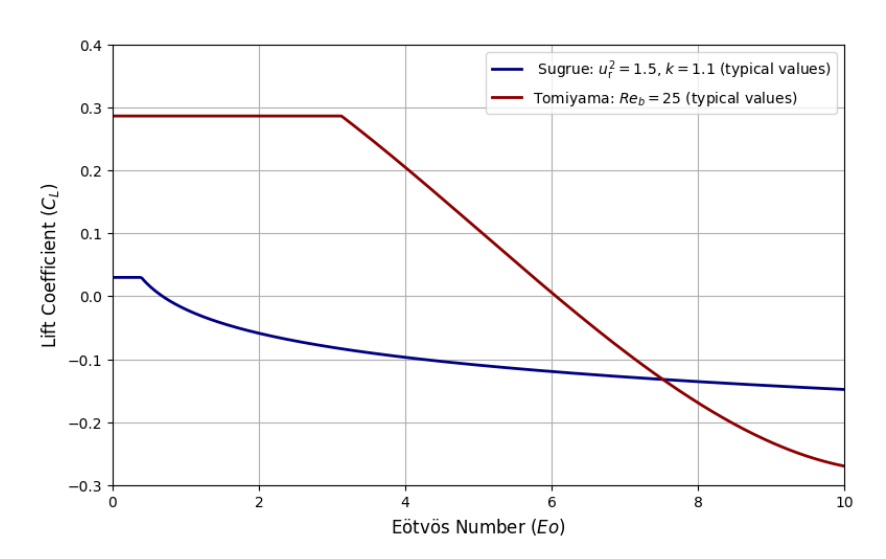


Figure 2.3: Comparison of Sugrue's and Tomiyama's Lift Coefficient.

An important modification to the formulations in this model was done: the void fraction term was set to one  $(f(\alpha) = 1)$ , leaving the lift coefficient solely dependent on the Wobble number (Wo). This simplification is supported by recent findings from Reiss et

2.1. Baseline model 35

al. [89], who observed that the void fraction-dependent term  $f(\alpha)$  undesirably damped the Wobble contribution. This resulted in a near-zero net lift coefficient, which in turn led to wall-peaked void fraction profiles in all test tubes (contradicting the experimentally observed center-peaked distributions obtained by negative lift coefficients).

Unlike earlier correlations, Sugrue's model contains no arbitrary tuning coefficients and has been shown to reproduce both wall-peaked and core-peaked void profiles over a wide range of flow conditions, which is a great improvement for general applicability.

#### 2.1.2.2 Turbulent Dispersion Force: Lopez de Bertodano

The Lopez de Bertodano model, expresses the turbulent dispersion force per unit volume as [51]:

$$\mathbf{F}_{\mathrm{TD}}^{\mathrm{c}} = -\mathbf{F}_{\mathrm{TD}}^{\mathrm{d}} = -C_{TD} \, \rho_{c} \, k_{c} \, \nabla \alpha_{c} \,, \tag{2.4}$$

where:

- $k_c$  is the turbulent kinetic energy,
- $C_{TD}$  is an empirical dispersion coefficient (typically  $0.1 \le C_{TD} \le 1.0$ ) [51].

Lopez et al. calibrated  $C_{TD}$  against vertical-pipe bubbly-flow experiments, finding good agreement in the ellipsoidal-bubble regime [51]. Subsequent studies have modified  $C_{TD}$  for large or small particle limits, but the form of Equation 2.4 remains the same [46]. By using the local field  $k_c$  rather than a global Reynolds number, and by tying the force directly to the resolved volume-fraction gradient.

This model was chosen over the widely used Burns formulation due to its simplicity (in both use and implementation), numerical stability, and demonstrated agreement with experimental data for horizontal channels [15,90]. Unlike Burns, the Lopez de Bertodano model is orientation-independent, relying solely on local turbulent kinetic energy and void fraction gradients—without dependence on slip velocity—making it particularly suitable for Eulerian–Eulerian simulations in small-diameter horizontal flows [51].

In such flows, where lift-induced phase separation and near-wall accumulation are prominent, turbulent dispersion plays a key role in achieving realistic void distributions and becomes one of the dominant contributors to the resolved void profile. The model acts as an effective void-smoothing mechanism and complements lift and drag forces, offering a robust and CFD-friendly closure that does not rely on bubble size or flow orientation.

#### 2.1.2.3 Wall Lubrication Force: Antal et al.

Antal et al. applied Blasius's theorem to a thin film between a rising bubble and a flat wall, and then generalized the result from cylinders to spherical bubbles by introducing an empirical wall-lubrication coefficient  $C_{WL}$  [55]. Their closure reads:

$$\mathbf{F}_{WL} = -C_{WL} \alpha_d \rho_c \frac{(\mathbf{u}_r - (\mathbf{u}_r \mathbf{n}_w) \mathbf{n}_w)^2}{d_b}$$
 (2.5)

$$C_{WL} = \max \left[ -C_{w1} + C_{w2} \frac{d_b}{2 y_w}, 0 \right]$$
 (2.6)

$$C_{w1} = -0.06 \,|\mathbf{u_r}| + 0.104, \quad C_{w2} = 0.147$$
 (2.7)

where:

- $\mathbf{n}_w$  is the unit normal pointing away from the wall,
- $y_w$  is the mean distance from the bubble center to the nearest wall.

This formulation ensures a repulsive lubrication force that vanishes when the term in brackets becomes negative. The main obstacle with this approach is the tuning of the coefficients  $C_{w1}$  &  $C_{w2}$ , the suggested values are  $C_{w1} = -0.01$  &  $C_{w2} = 0.05$  [58].

While the Antal et al. formulation is easy to use and modify and has been shown to improve void-fraction profiles in small-diameter channels, it is important to acknowledge its physical limitations. The underlying assumption that a wall-lubrication force arises from pressure gradients in a thin liquid film between a bubble and the wall is not well supported by experimental evidence. In reality, many bubbles in small and medium-diameter channels are observed to remain in direct contact with the wall, suggesting that such a film may not even exist under typical flow conditions [59].

While other more realistic models have been proposed in principle, such models have only been developed and validated for vertical channels. As no generalized version exists for small channel horizontal flows, the Antal model was retained because of its practicality and compatibility with small-channel simulations.

## 2.1.2.4 Drag Froce: Tomiyama

Tomiyama et al. proposed an empirical drag correlation for single bubbles in pure and (moderately) contaminated liquids [62]. The drag coefficient is given as a function of the bubble Reynolds number,  $Re_b$ , and the Eötvös number, Eo:

$$C_D = \max \left[ \min \left( \frac{24}{\text{Re}_b} (1 + 0.15 \,\text{Re}_b^{0.687}), \, \frac{72}{\text{Re}_b} \right), \, \frac{8 \,\text{Eo}}{3(\text{Eo}+4)} \right]$$
 (2.8)

While more advanced models such as the Ishii-Zuber correlation may offer improved accuracy under more specific conditions, the Tomiyama model remains more broadly applicable across a wide range of operating conditions (void fractions, velocities, (a)diabatic) [63]. Given the variability in flow regimes and inputs in this study, Tomiyama's formulation was deemed the most appropriate compromise between generality and accuracy for all the three models (baseline, refined and boiling). In all models the moderate contaminated version provided the best fit.

2.1. Baseline model 37

#### 2.1.2.5 Virtual Mass Force: Zuber

A classical Eulerian–Eulerian expression for the virtual mass force is [91]:

$$\mathbf{F}_{VM} = C_{VM} \, \alpha_d \, \rho_c \left( \frac{\mathrm{D} \mathbf{u}_c}{\mathrm{D} t} - \frac{\mathrm{D} \mathbf{u}_d}{\mathrm{D} t} \right), \tag{2.9}$$

where:

- $C_{VM}$  is the virtual-mass coefficient,
- D/Dt denotes the material derivative following each phase.

In this work, the classical formulation is retained with a constant coefficient  $C_{VM} = 0.5$ , as suggested by Zuber for clean spherical bubbles in inviscid flow [91].

While the virtual mass force is a theoretically well-established concept, it has not seen widespread application in practical two-phase CFD studies, and limited validation data is available. This is partly because it represents a purely inertial effect, and is difficult to isolate experimentally. The term was mainly incorporated in this model because inertial effects are relatively a bit more profound in small channels then in microchannels (where they are often neglected). Its inclusion serves to evaluate whether any measurable impact (fluid-dynamically as numerically) arises from modeling the virtual mass force in such confined geometries.

#### **2.1.2.6** Turbulence: $k-\varepsilon$ Model

**Turbulence Model** The standard  $k-\varepsilon$  model was chosen for its robustness and reliability. Since the domain lies in the small-channel regime rather than the microscale, the advantages of near-wall enhanced models like  $k-\omega$  are less pronounced, making the  $k-\varepsilon$  model a suitable and computationally efficient choice.

**Wall Model** In all three models developed in this work, the mesh is constructed to operate within the high- $y^+$  region ( $y^+ > 30$ ), which aligns with the logarithmic region of the boundary layer on Figure 1.9. This approach enables the use of standard wall functions, which are compatible with the selected k- $\varepsilon$  turbulence model and reduce computational cost by avoiding excessively fine near-wall mesh.

#### 2.1.2.7 Bubble Group Size: Pre-Integrated S- $\gamma$ Model

The Pre-Integrated  $S-\gamma$  model was selected to efficiently represent polydispersed gasliquid flows. The pre-integrated version further simplifies implementation by relying on built-in closure laws, enabling accurate estimation of interfacial area and SMD with minimal computational overhead. This model was consistently used in all three simulation stages (baseline, refined, and boiling) and therefore will not be discussed again in subsequent model sections.

# 2.1.3 Boundary and Initial Conditions

**Void Fractions:** To prevent numerical instabilities at startup (particularly in low-volume-fraction regions) the initial void fractions for the pipe walls and outlet were set to:  $\alpha = 1 \times 10^{-8}$ . The inlet void fractions were taken directly from the experimental data. This approach avoids the divergence issues commonly encountered when initializing with zero gas volume fraction.

**Velocities:** The velocity fields for both phases were calculated based on the experimental superficial velocities  $(j_c, j_d)$ , ensuring a consistent initialization with the expected gas-liquid flow ratio.

**Turbulence Settings:** For the dispersed gas phase, a turbulence intensity of I=0.05 and a turbulent viscosity ratio  $v_r=10$  were imposed. These are commonly adopted values for small channel pipe-driven two-phase flows and were observed to have minimal influence on the overall results within the studied operating range.

For the continuous liquid phase, turbulence properties were estimated based on the specific pipe geometry and inlet conditions. The turbulence intensity was calculated using the empirical correlation for fully developed pipe flow. The full calculation procedure is documented in Appendix B.

These turbulence initializations contributed to stable convergence behavior and physically consistent field development throughout the simulation domain. They were applied consistently across all models and contributed to stable convergence behavior and physically consistent field development throughout the simulation domain (and will therefore not be discussed again).

**Sauter Mean Diameter:** An initial SMD of 3.0 mm was adopted for all cases, producing stable and physically consistent results. This value aligns with both experimental observations and the recommendations of Burris et al. [92].

# 2.1.4 Solver parameters and Monitoring

All simulations were conducted using an unsteady segregated solver framework. A base time step of  $\Delta t=0.01\mathrm{s}$  was employed, with automatic time-step adaptation enabled. Due to the relatively efficient numerical setup and moderate mesh size, unsteady simulations converged rapidly, making this approach for this setup preferable over steady-state solution.

Table 2.3 summarizes the solver settings and under-relaxation factors used throughout the baseline model. These values were selected based on STAR-CCM+ best practices and refined through iterative testing to ensure stable and consistent convergence behavior across different flow regimes.

2.2. Refined model 39

Solver	Quantity Solved	Relaxation Factor
Segregated EMP Flow	Velocity	0.5
Segregated EMP Flow	Pressure	0.1
Volume Fraction	Gas-Liquid Distribution	0.5
S-Gamma	<b>Bubble Size Moments</b>	0.5
Segregated Energy	Enthalpy	0.5
$k$ - $\varepsilon$ Turbulence	$k, \varepsilon$ Transport	0.5
$k$ - $\varepsilon$ Turbulent Viscosity	Turbulent Viscosity	0.5

**Table 2.3:** Overview of solver settings for the baseline model.

# 2.2 Refined model

Simplified

# 2.2.1 Geometry and mesh

The geometry used in the refined model was based on the experimental setup by Triplett et al., which investigates air—water two-phase flow in horizontal microchannels with symmetric perpendicular air inlet configuration [3]. The test section features a pipe with an internal diameter of 1.1 mm, into which air is injected through two inlet tubes with a diameter of 1.45 mm. This configuration introduces complex flow development and interface dynamics representative of microchannel mixing behavior, making it a suitable benchmark for refined model validation.

Mesh Model	Mesh Type	Meshers	Base Size (mm)	Layers
Unified	Automated Mesh	Trimmed Cel	1.0	_
Split	Directed Mesh (Pipe)	Quadrilateral	0.1	100
opiit ,	Automated Mesh (Inlet)	Trimmed Cel	1.0	_

**Table 2.4:** Overview of mesh types and controls used for the refined model.

Butterfly

Directed Mesh

0.05(6)\*

100

Two main meshing strategies were evaluated for the refined model: one based on the full, detailed geometry (including both the water channel and the air inlet) and a second, simplified version of the geometry (like Figure 2.1). Within the full geometry setup, two mesh configurations were tested: a unified mesh spanning both domains, and a split-domain approach using separate meshes for the water and air inlets. The mesh settings used for each case are summarized Table 2.4 and the meshes can be seen on Figure 2.4, Figure 2.5 and Figure 2.6.

Although the combined mesh offered a continuous topology, it resulted in significantly longer run times without noticeable improvements in flow behavior or numerical stability. Consequently, the split mesh approach was adopted for the full geometry, while the simplified geometry used the butterfly-pattern patched mesh strategy for consistency and efficiency.

Given the increased sensitivity of the current simulations, special attention was de-

<sup>\*</sup>Geometric divisions from wall edge to center

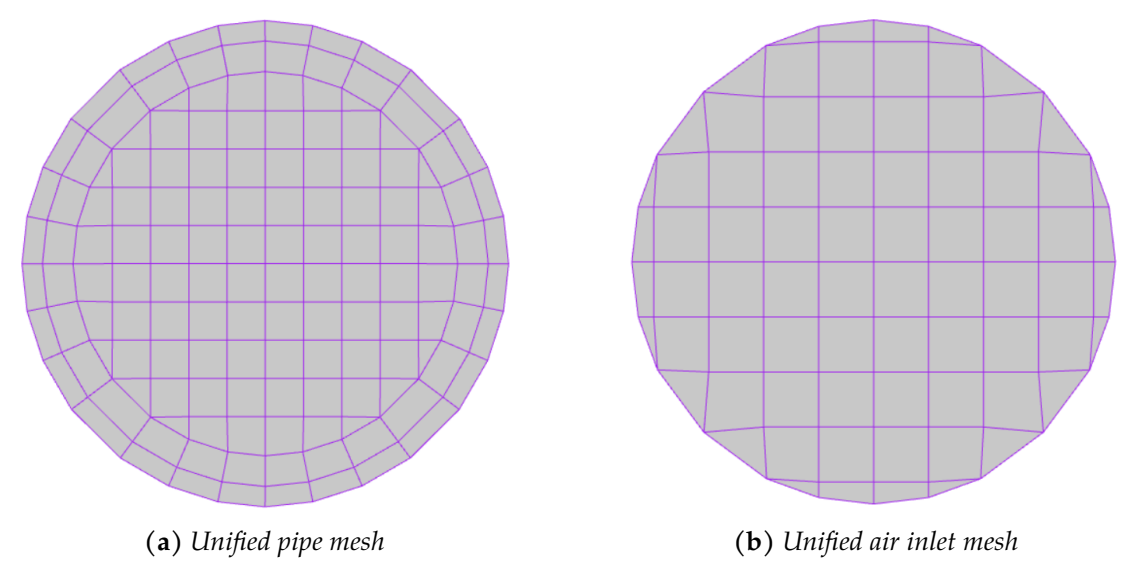


**Figure 2.4:** *Mesh overview of the unified mesh strategy.* 

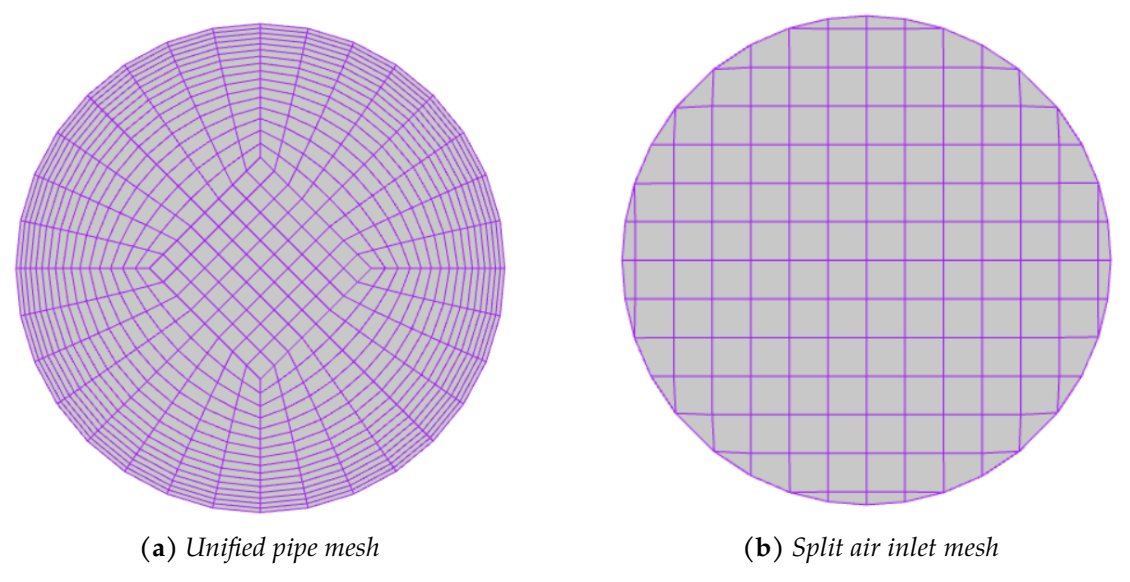


**Figure 2.5:** *Mesh overview of the split mesh strategy.* 

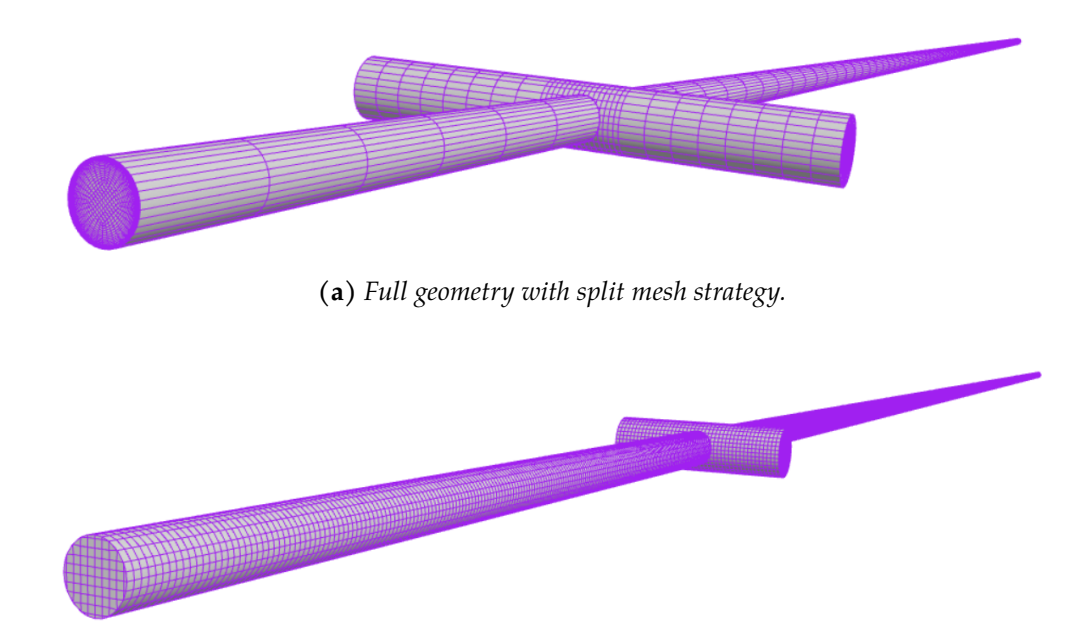
voted to mesh control parameters such as base size, surface growth rate, and the minimum diameter. These settings were carefully optimized to enhance mesh quality and ensure numerical stability while maintaining computational efficiency.

# 2.2.2 Physics Models

The interfacial forces used in the refined setup were chosen not only for their physical relevance to horizontal microchannel flow, but also with the eventual boiling model in mind. Since the primary aim of this thesis was to develop and compare models applicable to annular boiling flow, consistency across the refined and boiling cases was prioritized. This included using wall-directed lift and near-wall redistribution strategies that perform well under both adiabatic and diabatic conditions.

Table 2.5 summarizes the interfacial and turbulence models employed in the refined

2.2. Refined model 41



**(b)** Full geometry with unified mesh strategy.

**Figure 2.6:** Comparison of full-domain mesh strategies for the refined model.

setup, along with their respective coefficients or formulations. Compared to the base-line case, the model is almost completely changed which emphasizes again the difference in behavior between small and microchannels. Each model is described in more detail in Section 2.2.2.1–Section 2.2.2.5.

	J	
Interfacial Force	Model	Coefficient(s)
Lift	Constant	$C_L = -0.02$
Turbulent Dispersion	Burns et al.	$C_{\text{Calibration}} = 1.5$
Wall Lubrication	Lubchenko	-
Drag	Tomiyama	Intermediate contamination
Virtual Mass	Not included	-

**Table 2.5:** Overview of all models used for the refined model.

#### 2.2.2.1 Lift Force: Constant

A constant lift coefficient of  $C_L = -0.02$  was applied in the refined simulations. The choice of a negative constant was made to preserve wall-directed lift behavior, consistent with annular flow development in boiling regimes.

This strategy allowed the same lift setup to be reused in the boiling model without requiring re-tuning, facilitating more direct comparisons of phase distribution and pressure drop between the refined (adiabatic) and boiling (diabatic) cases. As the focus of this work was on developing a consistent CFD workflow across both flow regimes, this simplification was seen as a robust and justifiable compromise.

## 2.2.2.2 Turbulence Dispersion Force: Burns et al.

Burns et al. presented a detailed turbulent-dispersion closure that retains the influence of mean slip velocity, bubble size, and interfacial area. In their formulation, the dispersion force per unit volume is written as:

$$\mathbf{F_{TD}} = -\frac{3}{4} C_D \frac{\alpha}{D_b} \left| \mathbf{u_d} - \mathbf{u_c} \right| \underbrace{\frac{\mu_c^t}{\sigma_{TD}} \left( \frac{a_i}{\alpha} + \frac{1}{1 - \alpha} \right)}_{H(\alpha, k)} \nabla \alpha$$
 (2.10)

where:

- $C_D$  is the mean drag coefficient for a single bubble,
- $\sigma_{TD}$  is the turbulent Schmidt number for void-fraction diffusion,
- $\mu_c^t$  is the turbulent viscosity,
- a<sub>i</sub> is the interfacial area density,
- The bracketed term  $H(\alpha, k)$  accounts for the void-fraction dependence of the dispersion intensity.

This form emphasizes how turbulence (via  $\mu_L^t/\sigma_{TD}$ ), interfacial geometry ( $\alpha/D_b$ ,  $a_i$ ), and slip combine to drive diffusion of bubbles down the void-fraction gradient.

The Burns et al. model was chosen primarily because of its compatibility with the Lubchenko wall lubrication formulation (see Section 2.2.2.3. Lubchenko's approach explicitly assumes equilibrium with a dispersion force that has the structure of Burns' model. Using Burns instead of the Lopez formulation (baseline model) ensures a consistent force balance near the wall and allows the models to be coupled seamlessly. In addition to this theoretical compatibility, numerical tests showed improved stability when Burns was used in the refined Triplett setup. The Lopez model occasionally led to

sharp void gradients and convergence issues, whereas the Burns formulation provided smoother void redistribution and better numerical stability.

#### 2.2.2.3 Wall Lubrication Force: Lubchenko

Lubchenko et al. challenged the notion of a "physical" wall-lubrication force by observing that individual bubbles in contact with the wall experience no net lateral force pushing them away [59]. The key insight is purely geometric: spherical bubbles slide up the wall on a single point of contact (Figure 2.7a), and the cross-sectional area occupied by gas increases with distance from the wall (Figure 2.7b), yielding a parabola-shaped void fraction profile for a monodisperse layer (Figure 2.7c).

He therefore suggests that wall lubrication should not be treated as an additional physical force in Multiphase CFD, but rather as an averaging-correction that restores the near-wall void-fraction profile lost during volume averaging. The schematic in Figure 2.7 is taken from Lubchenko's original work [59].

Lubchenko et al. derived a wall-lubrication correction  $\mathbf{F}_{WL,TD}$  by enforcing equilibrium with the turbulent-dispersion force  $(\mathbf{F}_{TD} + \mathbf{F}_{WL,TD} = \mathbf{0})$  so that the parabolic near-wall

2.2. Refined model 43

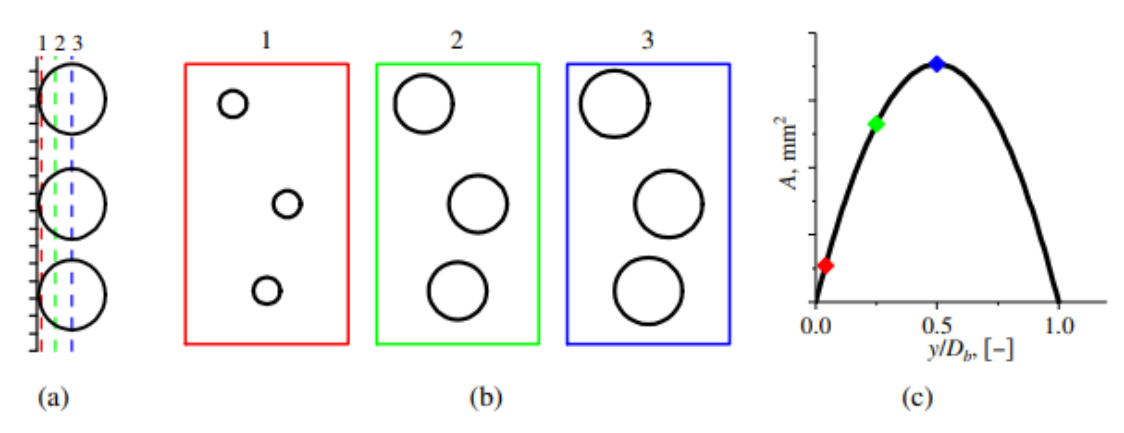


**Figure 2.7:** Schematic of Lubchenko's approach (a) side view of bubbles, (b) front view of the cross-sections of bubbles. (c) cross-section of gas phase as a function of distance from the wall.

void-fraction profile is recovered. Using Burns' turbulent-dispersion Equation 2.10 closure and by computing the averaged void fraction analytically by considering spherical bubbles of radius  $R_b = d_b/2$  sliding up the wall with centroid at  $y_0 = R_b$  so that

$$\nabla \alpha = \alpha_{\text{max}} \frac{4}{D_b} \left( 1 - \frac{2y}{D_b} \right) \mathbf{n}$$
 (2.11)

Substituting into the equilibrium condition gives the final piecewise expression:

$$\mathbf{F}_{WLTD} = \begin{cases} \frac{3 C_D}{4 D_b} \left| \mathbf{u_d} - \mathbf{u_d} \right| \frac{\mu_c^t}{\sigma_{TD}} \left( 1 + \frac{\alpha}{1 - \alpha} \right) \alpha \frac{1}{y} \frac{D_b - 2y}{D_b - y} \mathbf{n}, & y < \frac{D_b}{2}, \\ \mathbf{0}, & y \ge \frac{D_b}{2}, \end{cases}$$
(2.12)

where:

- $\sigma_{TD}$  is the turbulent Schmidt number for void-fraction diffusion,
- $\mu_c^t$  is the turbulent viscosity.

The Lubchenko wall lubrication model was selected despite being originally developed for vertical flows. While the refined model was designed to simulate horizontal microchannel flow (Triplet), the model's advantages (its strong physical basis, absence of tunable parameters, and seamless compatibility with the Burns turbulent dispersion formulation) made it a compelling option. Most importantly, Lubchenko's model was chosen with the boiling case in mind. Since the boiling simulations are conducted in a vertical microchannel, this model is ideally suited for that setup. Although it may not be the perfect fit for horizontal flow, using it here ensures a consistent interfacial force strategy across both refined and boiling models, which is essential for fair comparison and reliable performance evaluation.

#### 2.2.2.4 Drag Force: Tomiyama (& Kendoush)

As stated in Section 2.1.2.4, the intermediately contaminated Tomiyama drag coefficient  $(C_D)$  was used in all three models due to its broad applicability across a wide range

of operating conditions. Its robustness makes it suitable for both adiabatic and boiling flows without requiring regime-specific adjustments.

However, to explore the sensitivity of the model to flow regime characteristics specific to the Triplett geometry, an alternative drag model developed by Kendoush [64] was tested under selected conditions (Taylor flow). This model provides a closed-form expression for  $C_D$  tailored to long Taylor bubbles rising steadily in vertical pipes, derived from a balance of buoyancy and inertial drag under inertia-dominated flow. The expression incorporates the void fraction  $\alpha$ , liquid slug length  $L_f$ , and tube radius R:

$$C_D = 8.16 \left( \frac{\frac{8}{81} - \alpha \frac{L_f}{R}}{\alpha - \frac{4}{9}} \right) - 3.628$$
 (2.13)

- $L_f$  is the liquid slug length,
- *R* is the tube radius.

While this formulation may offer enhanced accuracy for Taylor flow structures, its limited applicability outside inertia-dominated vertical flows and sensitivity to geometric inputs (e.g.,  $L_f$ ) makes it less suitable for general two-phase conditions. For this reason, Tomiyama's model was retained as the primary drag correlation.

#### 2.2.2.5 Virtual Mass Force: Zuber

No virtual mass force was included in the refined model. In microchannel-scale geometries, inertial effects are significantly reduced due to small characteristic dimensions, making the contribution of virtual mass largely negligible. Furthermore, preliminary tests revealed noticeable momentum imbalances when the force was activated (particularly under conditions involving high slip velocities or significant initial void fraction inputs (>0.4)). For these reasons, the virtual mass term was excluded to improve numerical stability without compromising the results.

#### **2.2.2.6** Turbulence: $k-\varepsilon$ Model

The standard  $k-\varepsilon$  turbulence model was again used in the refined simulations for the same reasons as in the baseline case: it offers a well-established balance between accuracy and computational efficiency in fully developed pipe and channel flows. Its robustness in high-Reynolds-number regimes (conditions that are certainly present in several of the Triplett experiments) and its compatibility with the Eulerian–Eulerian framework make it a practical and reliable choice for modeling small-diameter horizontal two-phase flows.

## 2.2.3 Boundary and Initial Conditions

#### 2.2.3.1 Void Fractions & Correction Factor $\Psi$

The initial void fractions of the outlet and pipe were set to  $1 \times 10^{-5}$  for most cases to prevent numerical instabilities commonly associated with zero gas initialization. For

2.2. Refined model 45

high gas volume fraction cases ( $\alpha_d > 0.4$ ), a more adaptive approach was used by setting the initial value to 1% of the inlet void fraction to further aid convergence. However, simulations with extremely high inlet void fractions ( $\alpha_d > 0.85$ ) remained challenging and could not be fully converged despite these precautions.

For both the unified and split (realistic) mesh configurations, the air inlet void fractions were set to 1.0 and liquid inlet to 0.0 (logically). In contrast, for the simplified configuration, an empirical approach was used to determine the inlet void fractions based on the ratio of the dispersed velocity to the continuous ( $u_{dc}$ ).

To account for the mismatch between experimental solution void fraction and simulated initial void fractions, a correction ratio  $\Psi$  was introduced and correlated with the ratio of the dispersed velocity to the continuous ( $u_{dc} = u_d/u_c$ ). The correction ratio is defined as:

$$\Psi = \frac{\alpha_{i,\text{corrected}}}{\alpha_{\text{exp}}} \tag{2.14}$$

where  $\alpha_{\rm exp}$  is the surface-averaged void fraction measured in the test section of the Triplett experiments, and  $\alpha_{\rm corrected}$  is the adjusted initial void fraction that must be imposed at the inlet to numerically reproduce  $\alpha_{\rm exp}$  in the same testing region.

A series of 23 simulations was conducted using known experimental superficial velocities  $(j_c, j_d)$ , where  $\alpha_{\rm exp}$  was initially imposed. The initial void fraction was then iteratively adjusted until the simulation reproduced the experimental void fraction in the test section. The resulting correction ratios were plotted against the corresponding velocity ratios, and a correlation was formulated, as shown in Figure 2.8:

$$\Psi = \begin{cases}
1.2215 \cdot u_{dc}^{-0.813}, & \text{for } 0.05 < u_{dc} < 1 \\
\min \left[ 0.8, \ 0.5 + 0.432 \ln \left( \frac{u_{dc}}{0.5} \right) \right], & \text{for } 1 \le u_{dc} < 20
\end{cases}$$
(2.15)

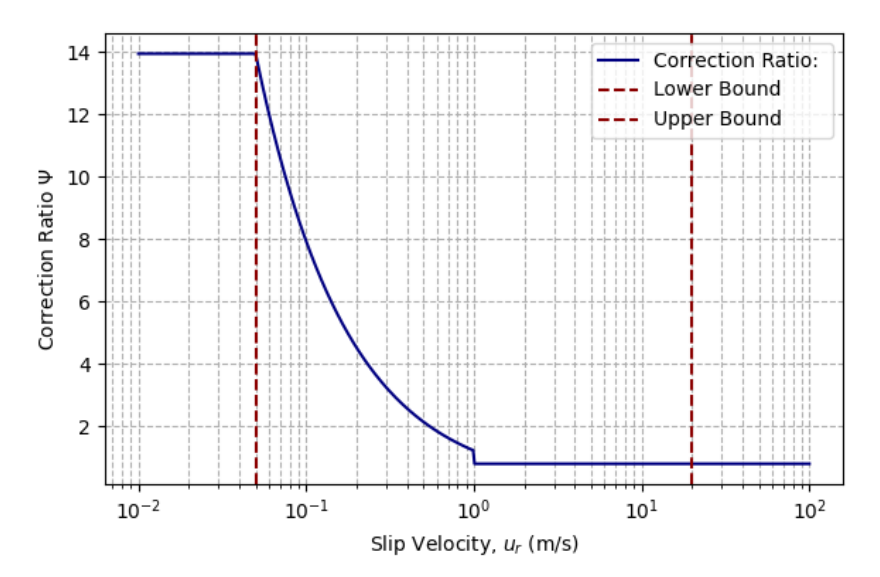


**Figure 2.8:** Correction ratio  $\Psi$  as a function of ratio of velocities  $(u_{dc})$ , based on the ratio between experimentally reported void fraction and the corrected inlet condition.

This formulation was found to perform well across a wide range of velocities ratios  $(0.05 < u_d c < 20)$  and provides a practical guideline for initializing void fractions in simulations that aim to match surface-averaged distributions from experimental data in horizontal microchannel flows. It must be additionally noted that when values larger than 0.90 are obtained for  $\alpha_{i,corrected}$ , they should be hard-set to 0.90, as higher values often lead to numerical instability in the simulation model.

However, in cases where experimental data for the surface-averaged void fraction was not available, the correction ratio approach could not be applied directly. To address this, an alternative empirical correlation was developed to estimate the expected surface-averaged void fraction directly from the ratio of velocities  $(u_{dc})$ . This was done by plotting the experimental superficial velocity data against the corresponding measured void fraction, which revealed a simple exponential relationship valid in the same range  $(0.05 < u_{dc} < 20)$ :

$$\alpha_{\rm exp} = 0.2779 \cdot u_{dc}^{0.423} \tag{2.16}$$

This correlation offers a lightweight and practical fallback method to initialize void fractions when experimental reference data was incomplete or unavailable. While this method is not grounded in first-principles fluid dynamics (e.g., dimensionless groups like Reynolds or Eötvös number), it offered a fast and surprisingly accurate way to estimate  $\alpha_{\rm exp}$  in the absence of direct experimental values, making it a practical engineering workaround for initializing simulations. It should also be noted that both the correction ratio correlation and this empirical prediction are tailored specifically to the Triplett dataset and geometry. They have not been validated against other experiments or geometrical configurations and should therefore be used cautiously outside the original context.

Additionally, to manage the high initial void fraction conditions and reduce numerical spikes, a ramp function was applied to gradually increase the inlet void fraction over time (iteration). This approach helped stabilize the early stages of the simulation by preventing abrupt phase interactions.

#### 2.2.3.2 Other Boundary and Initial Conditions

**Velocities:** The initial velocities for both phases were directly taken from the experimental data reported in the Triplett study [3]. Since the inlet conditions correspond to fully dispersed flow or single-phase injection (gas or liquid), the superficial velocities  $(j_c, j_d)$  were used as the phase velocities at the inlet (the same velocities were taken for the simplified mesh).

**Sauter Mean Diameter:** A constant initial SMD of 1 mm was used in all simulations. This value is the default value and wildly accepted for microchannel simulations.

2.3. Boiling model 47

# 2.2.4 Solver Parameters and Monitoring

While the baseline cases used an unsteady solver, the refined and boiling simulations adopted a steady-state framework to reduce computation time across more than 50 runs. This approach provided sufficient accuracy for the intended comparisons. Table 2.6 lists the relaxation factors used, with particular emphasis on velocity, pressure, and volume fraction which are key output parameters in the Triplett experiments [3].

Solver	<b>Quantity Solved</b>	Relaxation Factor
Segregated EMP Flow	Velocity	0.3
Segregated EMP Flow	Pressure	0.05
Volume Fraction	Gas-Liquid Distribution	0.3
S-Gamma	<b>Bubble Size Moments</b>	0.5
Segregated Energy	Enthalpy	0.5
$k$ - $\varepsilon$ Turbulence	$k, \varepsilon$ Transport	0.5
$k$ - $\varepsilon$ Turbulent Viscosity	Turbulent Viscosity	0.5

**Table 2.6:** Overview of solver settings for the refined model.

# 2.3 Boiling model

# 2.3.1 Geometry and mesh

The geometry used in this simulation was directly adopted from the experimental setup by Sumith et al. [5], featuring a vertical microchannel with an internal diameter of 1.45 mm and a heated region of 100 mm in length.

The meshing strategies used for this model focused on the use of a directed patched mesh (butterfly layout), which is advised by literature to be used by literature because it has the ability to capture the liquid-film formation more accurately [29]. Given its proven performance, this mesh type was selected as the baseline for further refinement. A mesh sensitivity analysis was then conducted by systematically varying the base size to evaluate its influence on solution accuracy (see Figure 2.9). Additionally, a comparison between the butterfly and quadrilateral meshing approaches was performed to confirm the robustness of the chosen strategy. The outcomes of this mesh analysis are presented in Section 3.3.3. Table 2.7 summarizes the detailed mesh settings used in the boiling model:

	3 31	<u> </u>	
Mesh Type	Meshers	Base Size (mm)	Layers
Directed Mesh	Auto (Quadrilateral)	2.0	100
Directed Mesh	Patched (Butterfly)	0.1 (10*)	100
Directed Mesh	Patched (Butterfly)	0.05 (14*)	100
Directed Mesh	Patched (Butterfly)	0.025 (12*)	100

**Table 2.7:** Overview of mesh types and controls used for the boiling model.

<sup>\*</sup>Geometric divisions from wall edge to center

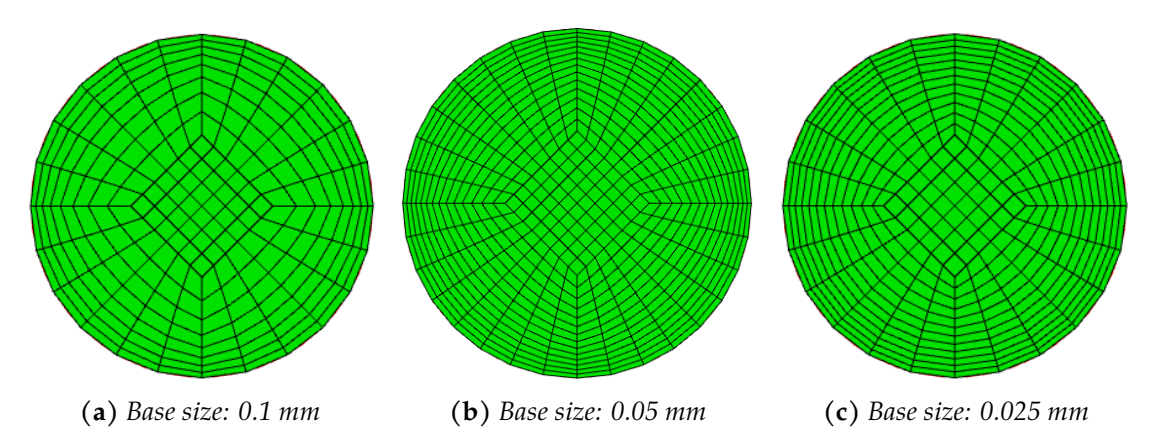


**Figure 2.9:** Comparison of mesh refinement levels for the boiling model.

# 2.3.2 Physics Models

#### 2.3.2.1 Interfacial Forces

As stated in Section 2.2.2, the interfacial force models used in the refined setup were selected with the goal of ensuring compatibility and optimal performance in vertical boiling microchannels, despite the different diameter and orientation. For consistency and comparative purposes, the same models for lift (Section 2.2.2.1), turbulent dispersion (Section 2.2.2.2), drag (Section 2.2.2.4), and virtual mass (Section 2.2.2.5) were reused here. These models are not described again in this section.

It is important to note that the wall lubrication model described in Section 2.2.2.3 was not incorporated into this boiling model. Although it was rigorously tested in combination with the MITB framework, its inclusion led to numerical instabilities for the current setup. As a result, the Lubchenko formulation was excluded to preserve simulation stability.

#### 2.3.2.2 Boiling Model

The boiling model implemented in this work is based on the recent framework developed by MITB [84]. This model introduces two key innovations: a newly reduced correlation for predicting the bubble departure diameter ( $D_b$ ) and a new formulation for wall heat transfer that remains valid across a broad range of pressures.

**Bubble Departure Diameter** ( $D_b$ ) This new formulation takes into account key physical influences such as pressure, wall superheat, liquid subcooling, and bulk velocity [86]. The resulting expression reads:

$$D_{d} = \underbrace{18.9 \times 10^{-6}}_{\text{Base constant}} \cdot \underbrace{\left(\frac{\rho_{\ell} - \rho_{g}}{\rho_{g}}\right)^{0.2747}}_{\text{Pressure effect}} \cdot \underbrace{Ja_{\sup}^{0.7845}}_{\text{Superheat effect}} \cdot \underbrace{(1 + Ja_{\sup})^{-0.3087}}_{\text{Subcooling effect}} \cdot \underbrace{u_{\text{bulk}}^{-0.2605}}_{\text{Velocity effect}}$$
 (2.17)

2.3. Boiling model 49

 Pressure effect: reflects the role of buoyancy, which intensifies at low pressure where the density ratio increases.

- Superheat effect: describes the thermal driving force for bubble growth. Larger superheat yields larger departure diameters.
- Subcooling effect: accounts for the degree of subcooling. Increased subcooling suppresses bubble growth, thus reducing departure diameter.
- Bulk velocity effect: describes convective stripping: higher liquid velocities shear bubbles off the wall earlier, leading to smaller bubbles.

**New all-pressure wall heat transfer model** As introduced in Section 1.10, four key coefficients are typically required to model wall boiling phenomena. However, the newly proposed wall heat flux that replaces the classical concept of quenching sliding conduction, leading to the following expression:

$$q_{wall}^{"} = (1 - S_{dry}) \, q_{NB}^{"} + S_{dry} \, q_{gas}^{"} \tag{2.18}$$

$$q_{NB}^{"} = q_f^{"} + q_{sc}^{"} + q_e^{"} \tag{2.19}$$

where:

- $q_{NB}^{"}$  is the heat flux transferred to the continuous via nucleate boiling,
- $q_{gas}^{"}$  is the heat flux transferred directly to the dispersed phase,
- $q_f''$  is the forced convective heat transfer contribution,
- $q_{sc}^{"}$  is the sliding conduction contribution, replacing traditional quenching,
- $q_e^{\prime\prime}$  is the evaporative heat transfer contribution.

Therefore, in addition to the fundamental parameters already discussed (excluding  $h_q$  and redefining  $A_e$ ), several new parameters become essential when extending the wall boiling model to include sliding conduction and more detailed nucleate boiling behavior:

- $h_{sc}$  is the sliding conduction heat transfer coefficient,
- $N_h''$  is the number of active nucleating bubbles per unit area,
- $A_{sl}$  is the average bubble sliding length along the wall,
- *t*\* is the characteristic time needed to reform the thermal boundary layer.

For a complete description of the derivation of the models and coefficients used in this formulation, the reader is referred to the work of Kommajosyula, specifically Chapter 4.1 [84]. How these parameters are specifically implemented into STAR-CCM+ is detailed in Appendix B.

## 2.3.3 Boundary and Initial Conditions

**Heat Flux:** To avoid non-physical spikes and instability at the start of the simulation, the wall heat flux was gradually introduced using a linear ramp function. This allowed

the system to adapt smoothly to increasing thermal loads, promoting convergence and physical realism in the early stages of boiling onset.

**Void Fractions:** A similar initialization strategy was applied as in the previous cases: both the pipe and outlet regions were initialized with a small void fraction to assist convergence. In addition, the inlet void fraction was set to also to the same value  $(1\times10^{-6})$ , helping to stabilize the volume fraction solver during the early stages of simulation when no boiling has yet occurred.

**Velocities:** The phase velocities were computed from the prescribed mass flux using the relation:

$$v = \frac{G}{\rho_c(T)}$$

where G is the local mass flux and  $\rho_c(T)$  is the temperature-dependent density of the continuous phase (the dispersed phase density is neglected).

**Sauter Mean Diameter:** An initial SMD of 1.0 mm was used, consistent with the refined model. Since no boiling is present at the simulation start (due to the use of a heat-flux ramp), this initialization is sufficient. As the simulation progresses and wall heating is introduced, the SMD evolves automatically through the boiling and breakup models.

# 2.3.4 Solver Settings and Strategy

For the boiling model, a hybrid approach was adopted using both steady-state and unsteady solvers. Steady-state simulations were first used to bring the system close to convergence, after which unsteady simulations were initiated to obtain an even more accurate solution.

Due to the added complexity introduced by phase change, wall boiling, and strong local gradients, the relaxation factors were carefully tuned to ensure numerical stability and convergence. In particular, attention was given to the pressure, volume fraction, and energy equations (as seen in Table 2.8, which are especially sensitive under diabatic conditions.

Solver	<b>Quantity Solved</b>	Relaxation Factor
Boiling Mass Transfer Rate	Mass	0.1
Segregated EMP Flow	Velocity	0.1
Segregated EMP Flow	Pressure	0.05
Volume Fraction	Gas-Liquid Distribution	0.3
S-Gamma	Bubble Size Moments	0.5
Segregated Energy	Enthalpy	0.25
$k$ - $\varepsilon$ Turbulence	$k$ , $\varepsilon$ Transport	0.5
$k$ - $\varepsilon$ Turbulent Viscosity	Turbulent Viscosity	0.5

**Table 2.8:** Overview of solver settings for the boiling model.

# 2.4 Performed Simulations & Setups

Now that the physical models and their implementation have been described, this section presents the simulations conducted using those models. The aim is to evaluate their performance across various geometries and operating conditions, with a primary focus on the annular flow regime. The objective is to extract key fluid-dynamic and thermo-hydraulic parameters to better understand two-phase flow behavior in microchannels, with the ultimate goal of transferring this knowledge to applications in MCHE design.

To enable quantitative comparison with experimental data, custom-defined planes, line probes, and point monitors were placed within the domain to replicate the measurement locations reported in the reference literature. Results were extracted using surface averages, integral volume averages, and global domain-averaged quantities.

#### 2.4.1 Baseline Model

In the baseline model, the primary objective was to validate the void fraction and velocity profiles against the experimental data of Kocamustafaogullari et al. [87]. Additionally, results were compared to the numerical study of Ekambara et al., who performed similar simulations using the commercial CFD software CFX-5.7.1 [15]. Pressure drop predictions were not a focus at this stage, as the larger channel dimensions fall outside the typical operating range of MCHEs and thus have limited relevance for microchannel heat exchanger design.

Furthermore, no evaluation of flow regimes was performed for the same reason: the flow structures observed in small channels differ significantly from those in microchannels, and insights derived from them cannot reliably be extended. Lastly, a mesh sensitivity analysis was carried out to assess the influence of the butterfly mesh in larger channels, providing possible insights for future scaling of the method. Beyond result comparison, this baseline model served as a foundational step to establish and calibrate the multiphase CFD modeling framework used in the refined and boiling configurations.

#### 2.4.2 Refined Model

The refined model served as the primary testing platform for evaluating adiabatic microscale two-phase flow behavior. Compared to the baseline setup, this model introduced a complex geometry based on the Triplett experiment, which significantly increased numerical difficulty and model sensitivity [3,93]. As will be discussed in the results section, achieving stable convergence in the full geometry proved challenging. To address this, the simplified mesh configuration was adopted, which enabled the development of the correction factor  $(\Psi)$  to adjust initial void fractions and ensure physically consistent results.

In contrast to the baseline model (where insights into the flow structure were of limited) the refined model targeted microscale-specific fluid dynamic parameters. In particular, it focused on accurate pressure drop prediction and flow regime identification, both of which are critical for the design and optimization of MCHEs, especially under boiling conditions. Additionally, a theoretical expression for the liquid film thickness was evaluated against both experimental data and simulation results. This comparison serves as a foundation for the subsequent development of the boiling model, where the dynamics of the liquid film play a central role in heat transfer performance.

# 2.4.3 Boiling Model

In this section, the boiling model was evaluated with a focus on two key aspects: pressure drop and wall superheat. Pressure drop predictions were benchmarked against experimental results from Sumith et al., serving as a validation for the model's thermohydraulic fidelity under boiling conditions [5]. The model was rigorously tested against wall temperature data, aiming to replicate both the absolute wall superheat, the variation in superheat across the heated surface and the wall superheat itself. These quantities are critical for understanding the onset and evolution of nucleate boiling in microchannels.

A mesh sensitivity analysis was also performed to assess the robustness of the predictions. Different meshing strategies were compared, including the default butterfly mesh and a structured quadrilateral-based approach. The influence of base cell size on the accuracy of the boiling model was also investigated.

#### 2.4.4 Monitoring of the simulations

Simulations were continuously monitored using vector and scalar (and streamline) visualization fields to identify and correct instabilities as early as possible. Insights from these fields were helped maintaining numerical stability and diagnosing the regions and mechanisms responsible for simulation divergence. The following set of diagnostics was used:

- **Velocity Spikes:** Local velocity magnitudes were tracked at interfaces and outlet boundaries to detect nonphysical spikes.
- Mass and Energy Balances: Global mass and energy were monitored to identify any imbalances or sharp deviations.
- Flow Regime Evolution: For the refined and boiling models, flow regime development was monitored to confirm annular behavior; interfacial force coefficients were tuned accordingly.
- **Void Fraction Conservation:** Void fraction fields were used to detect early signs of instability such as pressure surges or thermal runaway. An example of one of the used void fraction conservation techniques includes computing the volume-averaged value  $(\bar{\alpha}(t) = \frac{1}{V} \int_{V} \alpha(\mathbf{V}, t) \, dV)$  and verifying that  $\bar{\alpha}(t)$  remained equal to the prescribed initial void fraction  $\alpha_0$  (within numerical tolerance)

- Phase Momentum and Energy Stability: Residuals of phase momentum and total energy equations were recorded per iteration to assess numerical stability.
- Additional Diagnostics: Case-specific tools such as cross-sectional field analysis, pressure profile evolution, and wall heat flux trends were used to gain deeper insight into local instabilities and transient behaviors.

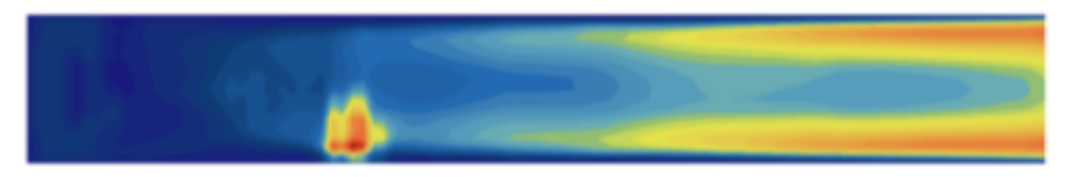


**Figure 2.10:** *Example of instability caused by singularity* 

# Results & Discussion

## 3.1 Baseline Model

The main objective of the baseline model was to accurately reproduce the velocity and void fraction profiles from Kocamustafaogullari's paper, while simultaneously gaining familiarity with CFD tools, specifically STAR-CCM+ [87]. This involved ensuring numerical stability and correct model setup, including the proper specification of boundary and initial conditions for both phases, as well as tuning turbulence-related parameters such as turbulent velocity scale, viscosity ratio, and turbulence intensity.

#### 3.1.1 Foundational Work

Overall, the baseline model demonstrated good numerical stability across the velocity range investigated. Although minor velocity spikes occasionally appeared near wall regions, they generally dissipated without triggering divergence, highlighting the robustness of the initial setup. While these results may not yield insights from a fluid-dynamic perspective, they served a critical role in validating the modeling framework and simulation practices. These foundational settings not only ensured stable behavior but also provided a flexible simulation environment, enabling the rapid integration and assessment of more advanced physical sub-models in later stages.

# 3.1.2 Liquid Velocity and Void Fraction Profile Validation

After the model proved to be stable over a wide range of input (superficial) velocities and void fractions, specific input and geometric parameters were used to mimic Kocamustafaogullari et al. experimental data [87]. As said before, results were also compared to the numerical results of Ekambara et al. [15]. It is again important to note that this experimental setup was a horizontal small ( $\oslash 50.26 \,\mathrm{mm}$ ) channel.

The numerical results from the baseline model are compared against the experimental data in Figure 3.1 and Figure 3.2. Simulations were carried out under four operating conditions, each defined by a superficial gas velocity  $(j_g)$ , superficial liquid velocity

3.1. Baseline Model 55

 $(j_f)$ , and resulting void fraction  $(\alpha)$ . The corresponding parameter sets for each case are:

Case A: 
$$j_g = 1.34$$
,  $j_f = 4.98$ ,  $\alpha = 0.204$ ,  
Case B:  $j_g = 0.80$ ,  $j_f = 4.98$ ,  $\alpha = 0.139$ ,  
Case C:  $j_g = 0.49$ ,  $j_f = 5.09$ ,  $\alpha = 0.080$ ,  
Case D:  $j_g = 0.24$ ,  $j_f = 5.10$ ,  $\alpha = 0.043$ .

All the experimental and numerical values (+ profiles) mentioned in Section 3.1.2.1 - Section 3.1.2.3 can be found in respectively Kocamustafaogullari's and Ekambara's papers [87] [15].

#### 3.1.2.1 Radial Void-Fraction Results

Across cases A–D, the best turbulent-dispersion coefficients were found to be  $C_{TD}$  = 0.80 for A, B and D, and  $C_{TD}$  = 0.85 for C. They all fall in the recommended range of 0.1-1.0 proposed by Lopez [51]. The most important observations were and can be seen on Figure 3.1:

- All cases showed good agreement between the experimental data and obtained results.
- Slight deviations between the experimental data and obtained results was observed near the bottom of the pipe  $(-1.00 \rightarrow -0.25 \ z/R)$ .
- Excellent good agreement was found in the upper region of the pipe. This indicates that the interfacial forces are modeled correctly for this setup.
- For the low void fraction ( $\alpha$ ) simulations (Case C & D), there is a slight shift of the obtained result to the right in comparison with the experimental data.
- The average relative deviation for each case were: 5.69%, 4.44%, 6.80%, 10.97% (Figure 3.1e).
- The absolute relative deviation is the highest at the top of the pipe.

#### 3.1.2.2 Liquid Radial Velocity Results

For all cases, the simulation reproduces similar radial velocity profiles but with different magnitudes. The most notable findings were and can be found on Figure 3.2:

- The shape of the profile and magnitude corresponds well with experimental data for cases A & B.
- Cases C & D showed larger deviation in profile shape between the top + bottom and center, but the maximum magnitude was in good agreement.
- The average relative deviation for each case were: 3.52%, 3.18%, 6.38%, 4.40% (Figure 3.2e).
- The absolute relative deviation is the lowest at the center of the pipe.

#### 3.1.2.3 Two-Dimensional Profile Comparison

The obtained 2D-profiles for cases B, C & D were compared against Ekambara's numerical data<sup>1</sup> and Kocamustafaogullari's experimental data. The peak values are summarized in Table 3.1 and the 2D void-fraction and velocities profiles can be found in Figure 3.3 and Figure 3.4.

Case		Peak void f	raction	Peak liquid velocity [m/s]			
	Ours	Ekambara	Koca. (exp.)	Ours	Ekambara	Koca. (exp.)	
В	0.411	0.583	0.445	7.03	7.029	7.148	
C	0.236	0.334	0.246	6.50	5.963	6.452	
D	0.148	0.192	0.142	6.24	5.747	6.383	

**Table 3.1:** Comparison of peak void fraction and peak liquid velocity

The velocity and void fraction profiles, along with their respective peak values, confirm the validity of the selected set of interfacial force models as defined in Section 2.1.2. In particular the lateral forces (lift, turbulent dispersion, and wall lubrication) were confirmed to be well-suited for the present setup. The strong agreement observed in the upper region of the pipe further supports this conclusion.

An important discussion point is the slight shift of the radial void-fraction profile to the right for the low void-fraction simulations. This shift can likely be attributed to a combination of physical and numerical effects [94]. Since the lift force model (Sugrue) is independent of the void fraction, and the turbulent dispersion force depends on the gradient of the continuous phase volume fraction (which should stabilize and symmetrize the distribution even more), the most plausible explanation lies with the wall lubrication force. The adopted model (Antal et al.) is linearly dependent on the void fraction. Therefore a lower void fraction results in a weaker wall lubrication effect that implies a reduction in lateral migration away from the surface, and thus a rightward shift of the bubble concentration profile.

The deviations noted in the velocity profiles for cases C & D are likely attributable to the poor quality or unrealistic nature of the experimental reference data. However, the discrepancy observed in Case A (both for the velocity and void fraction profile) is less easily explained by experimental uncertainty. It is linked to the choice of turbulence model, the standard k- $\epsilon$  model. To investigate this further, additional simulations using the k- $\omega$  turbulence model, which typically performs better in flows with strong separation, are recommended.

 $<sup>^{\</sup>rm 1}$  No numerical data was provided by Ekambara for case A

3.1. Baseline Model 57

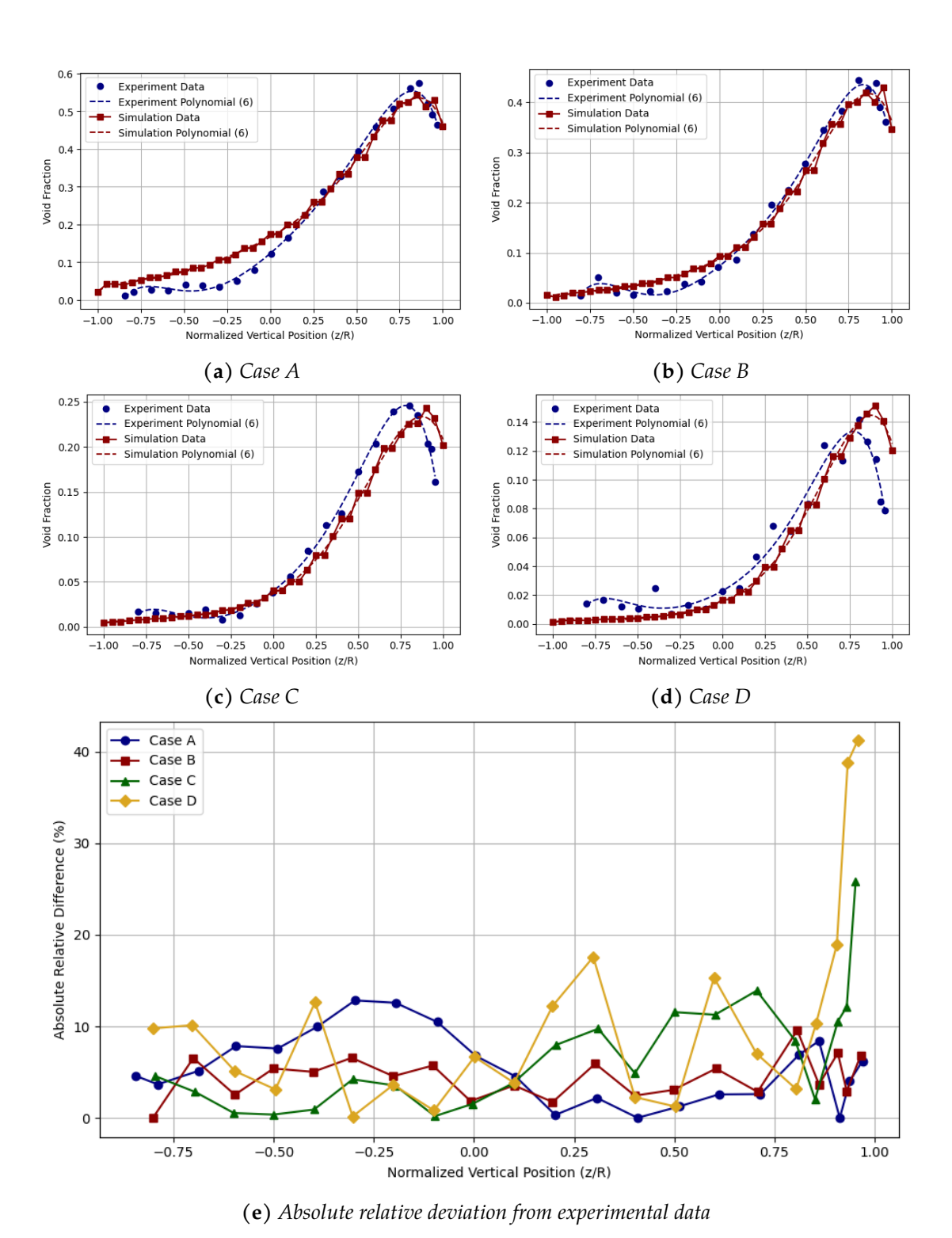


**Figure 3.1:** *Radial void-fraction profiles and absolute relative deviations for Cases A–D.* 

58 3. Results & Discussion

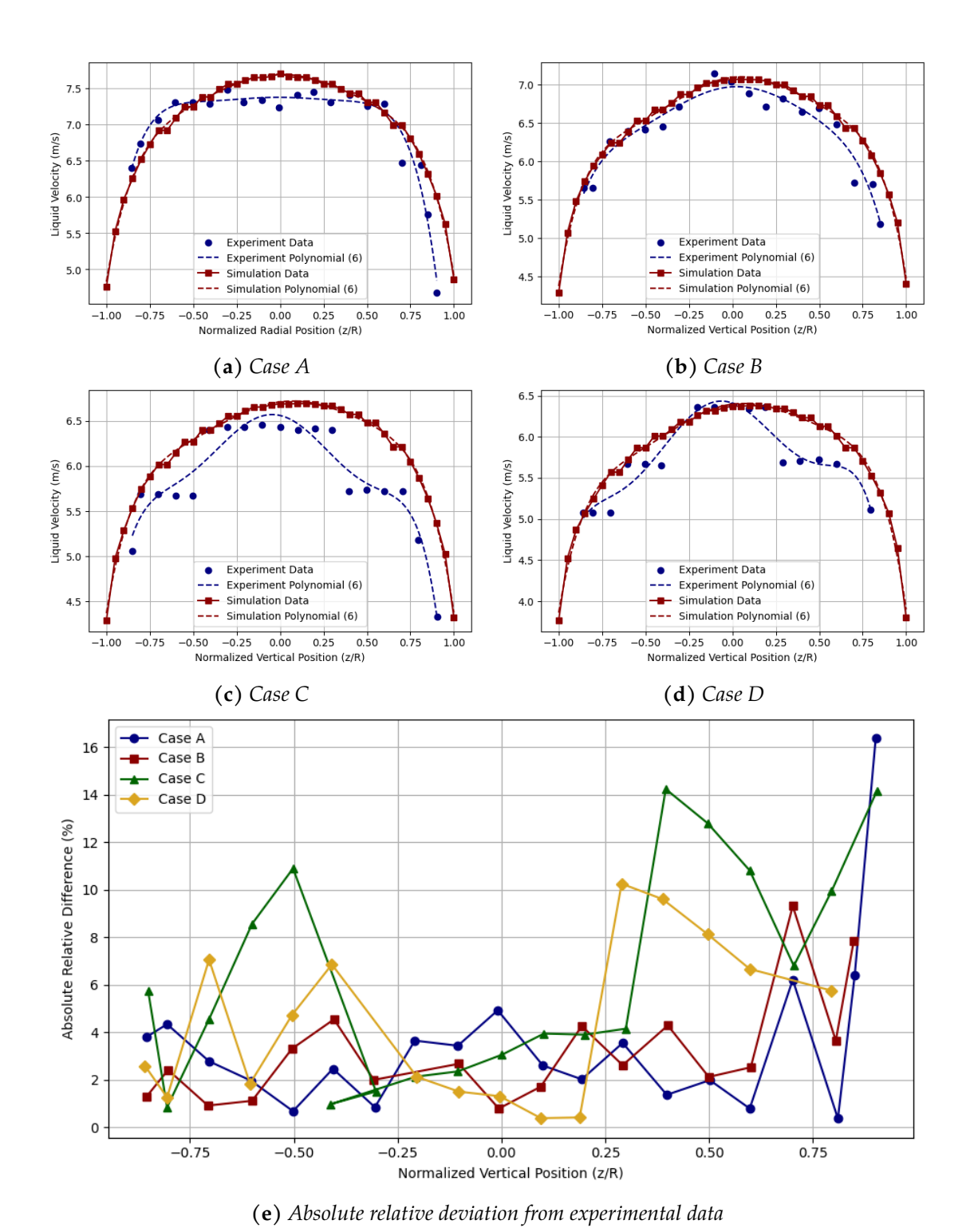


**Figure 3.2:** *Liquid radial velocity profiles and absolute relative deviations for Cases A–D.* 

3.1. Baseline Model 59

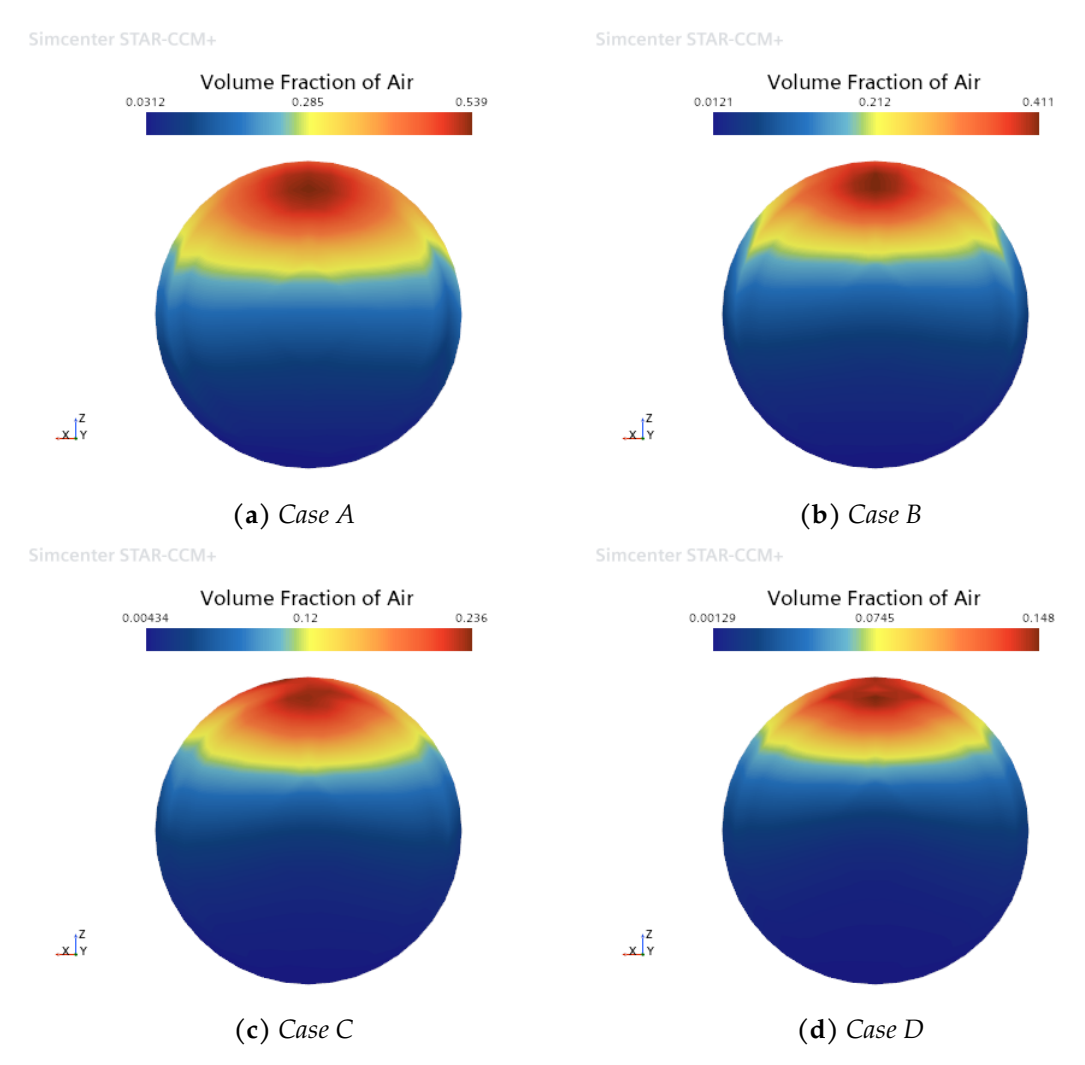


**Figure 3.3:** 2D void-fraction profiles for Cases A-D

3. Results & Discussion

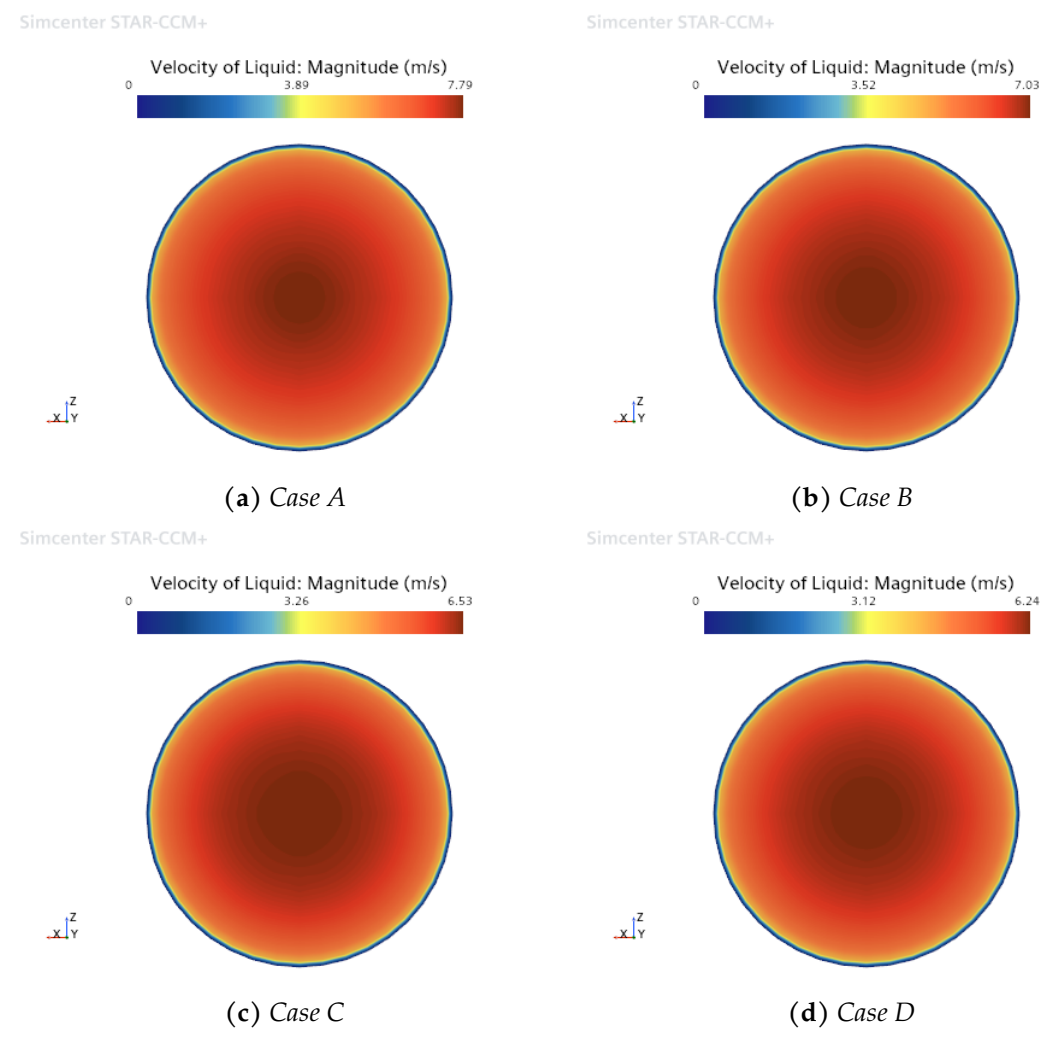


**Figure 3.4:** 2D velocity profiles for Cases A-D

3.1. Baseline Model 61

#### 3.1.2.4 Common Results

As demonstrated across the various test cases, the optimal turbulent dispersion coefficient  $C_{TD}$  remained relatively consistent and generally fell within the 0.1–1.0 range recommended by López et al. [51]. This results suggests that a constant value for  $C_{TD}$  yields reliable results across a moderately wide range of input velocities. Although more accurate formulations could involve making  $C_{TD}$  dependent on local flow parameters, no significant improvement is believed to be made by incorporating this.

A more critical observation was the sensitivity of the simulation to the chosen  $C_{TD}$  value: excessively high values, especially when combined with suboptimal unsteady solver time-steps, led to mass conservation errors and nonphysical flow patterns. Conversely, overly low values resulted in inflated void fractions, over-mixed phases, and unrealistic interface distributions. Figure 3.5 illustrates the consequences of an underestimated turbulent dispersion coefficient.

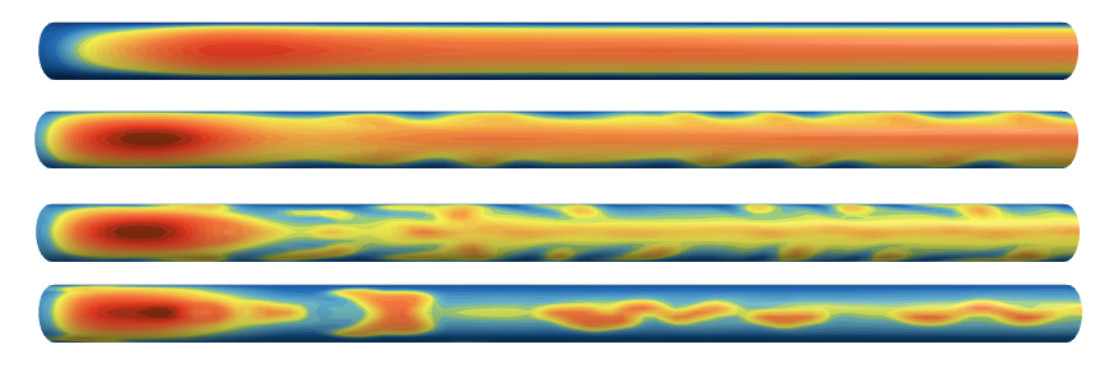


**Figure 3.5:** The influence of  $C_{TD}$  on the void fraction distribution (top view), from low  $C_{TD}$  (0.2) to extremely high  $C_{TD}$  (1.5).

Another notable finding is that the optimal turbulent dispersion coefficient identified in this study deviates from the value used by Ekambara et al. ( $C_{TD} = 0.5$ ). While various unknowns exist regarding model inputs and boundary or initial conditions, and although Ekambara slightly underpredicts the peak velocities observed in their own experiments, the interfacial force models employed are largely similar. The primary difference lies in the neglect of the virtual mass force in Ekambara's setup.

This suggests that the virtual mass force may contribute slightly to the observed peak values in void fraction and velocity. However, the overall distributions remain comparable, implying that virtual mass effects are not dominant in shaping the general flow profile. Still, the deviation in  $C_{TD}$  values might indicate that neglecting the virtual mass force indirectly impacts peak velocities and void fractions, as a higher turbulent dispersion coefficient may be needed to compensate for the virtual mass momentum exchange.

For all cases the validation criteria defined in Section 2.4.4 held true, an example of the mass-conservation errors for the gas and liquid phases is shown in Figure 3.6 and Figure 3.7. The two curves exhibit complementary behavior: the air-phase error is negative (starting around -0.02 g, dipping to roughly -0.04 g near iteration 200, then

recovering to about -0.01 g), whereas the liquid-phase error is positive (rising from 10 g up to 35 g by iteration 800, then settling near 5 g  $\approx 0.035\%$ ). Both errors diminish and fluctuate within tight bands after convergence, confirming that mass is conserved globally. The broad envelope in the early iterations is simply a consequence of the fully unsteady approach (each time step alternately over- and under-shoots mass in the unsteady approach) and when thousands of points are plotted in a compressed view, they form a wide "filled" band rather than a single line.

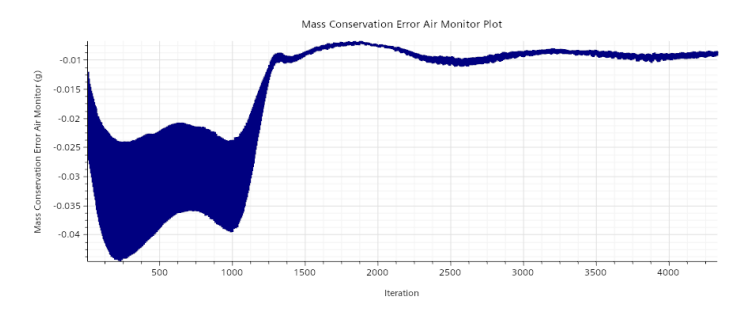


**Figure 3.6:** *Mass-conservation error for the air phase.* 

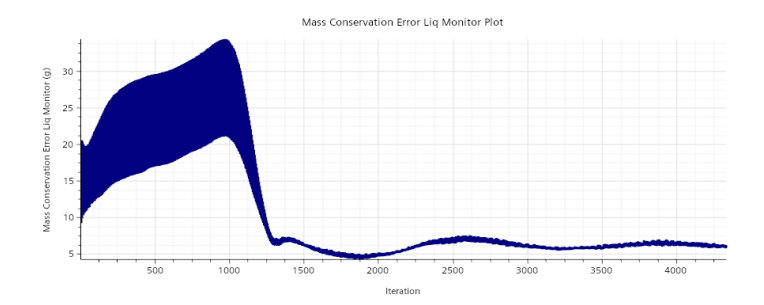


**Figure 3.7:** *Mass-conservation error for the liquid phase.* 

In summary, the present baseline model reproduces both void-fraction distributions and velocity profiles with high accuracy to experimental and numerical benchmarks. The agreement in peak velocity and the realistic phase distribution indicate that the model also captures the essential hydrodynamic behavior. Consequently, this validated setup provides a reliable baseline for future studies.

#### 3.1.2.5 Mesh Sensitivity Analysis

A mesh sensitivity analysis was performed on case B (which has the best agreement to experimental data for both velocity and void-fractions radial and 2D-profiles. The meshing strategies compared have already been described in Section 2.1.1 and will not be repeated here.

The most significant differences were observed in the radial profiles. While the 2D-profiles plots exhibited similar shapes (and are therefore not shown), the radial profiles revealed notable deviations in magnitude. As shown in Figure 3.8a, the quadrilateral mesh struggled to accurately predict the void fraction near the pipe wall, whereas the

3.1. Baseline Model 63

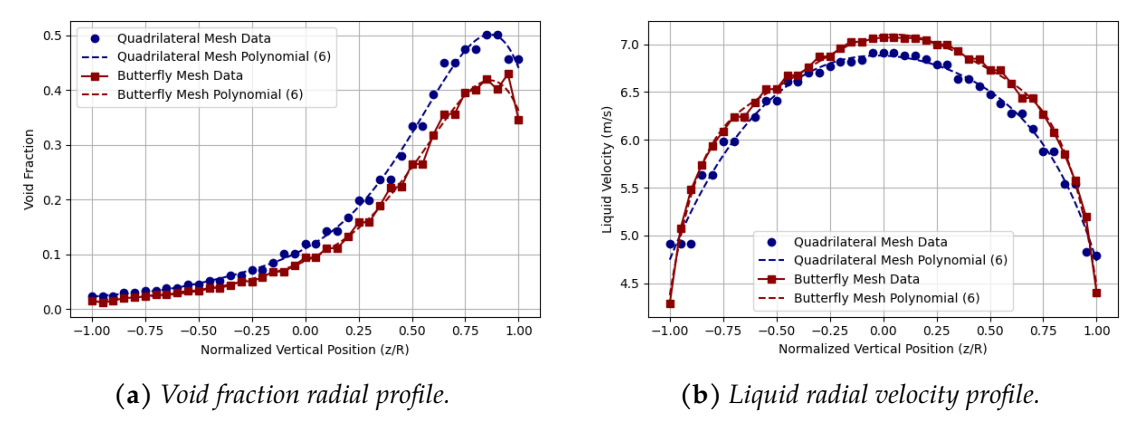


**Figure 3.8:** *Influence of mesh strategy on radial profiles for Case B.* 

butterfly mesh showed much better agreement with experimental data. In contrast, the differences in the liquid velocity radial profiles were less pronounced, as seen in Figure 3.8b.

This discrepancy highlights the critical role of mesh topology in resolving near-wall interfacial dynamics. Since the liquid phase is less sensitive to interfacial forces, the velocity field remains relatively unaffected, unlike the void fraction distribution. Even in small-diameter channels, accurate modeling of wall-bounded phenomena requires not only advanced interfacial force models but also mesh structures that retain sufficient geometric resolution. In particular, the observed deviations are likely due to how the Sugrue lift model responds in under-resolved boundary layers: in coarsely meshed near-wall regions, Wobble numbers are overestimated due to elevated turbulence, which in turn amplifies the lift force. This overprediction inflates the void fraction near the wall, a trend clearly visible in the quadrilateral mesh results.

#### 3.2 Refined Model

Using this model, we aimed to reproduce the experiment performed by Triplett et al. [3], with the objective of predicting pressure drops, liquid films and capturing specific characteristic flow patterns (annular), while maintaining computational robustness.

#### 3.2.1 Meshing Strategy Choice

As outlined in Section 2.2.1, two meshing strategies were evaluated for the mixing-pipe simulations: a full (split) geometry and a simplified one. It was quickly observed that the primary challenge in using the full geometry was maintaining numerical stability. Significant velocity spikes emerged near the liquid–air interface and at the outlet region. Figure 3.9 and Figure 3.10 illustrate the difference between stable and unstable velocity fields in these regions.

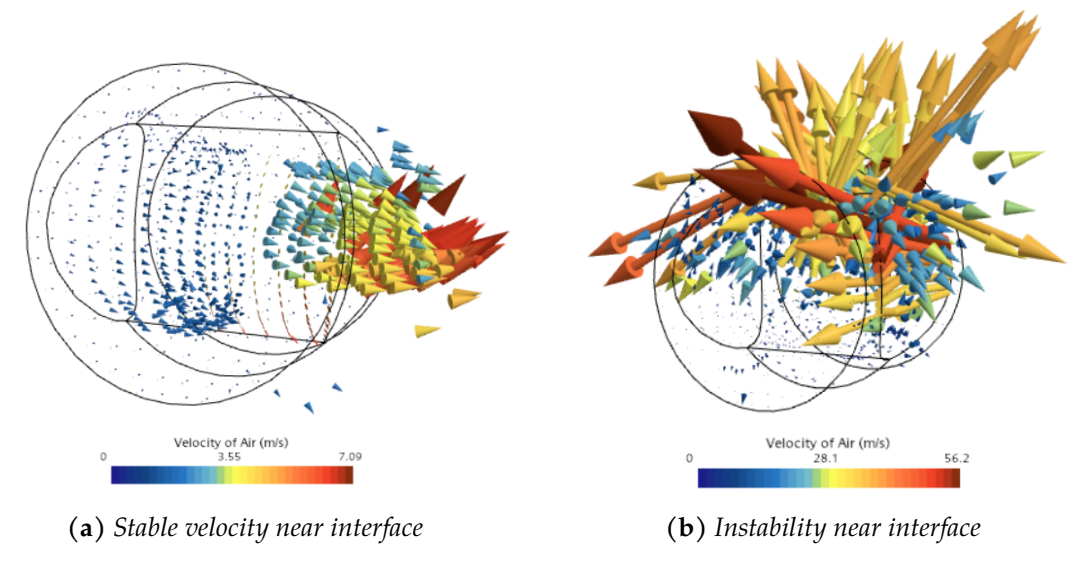


**Figure 3.9:** Comparison of stable vs unstable velocity near the liquid—air interface.

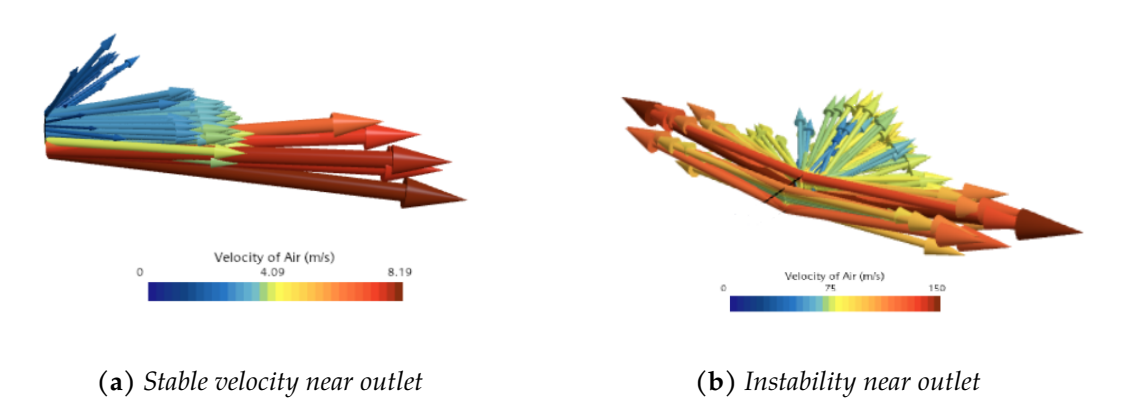


**Figure 3.10:** Comparison of stable vs unstable velocity near the outlet region.

Although some of these instabilities were mitigated by refining the mesh and carefully tuning boundary and initial conditions they were still present (just in a lower magni-

3.2. Refined Model 65

tude), the presence of sharp spatial gradients (especially near geometric edges) continued to cause divergence issues. These became particularly pronounced when the Lubchenko wall lubrication model was activated.

Consequently, the decision was made to conduct the simulations using the simplified geometry. However, as discussed in Section 2.2.3.1, a correction correlation  $(\Psi)$  had to be developed to account for the geometric simplifications and maintain physical accuracy.

#### 3.2.2 Predictive Performance of the Correction Factor $\Psi$

Before simulating the pressure drops for the Triplett experiment, it was necessary to determine the appropriate initial void fractions for the simulations ( $\alpha_{i,corrected}$ ) since the simplified mesh approach was adopted. The first step involved computing the theoretical surface-averaged void fraction based on the known interfacial velocities, using the formulation in Equation 2.16.

Next, the correction factor  $(\Psi)$  was calculated using Equation 2.15. Finally, this value was used to back-calculate the initial void fraction to be set in the simulation domain by applying the inverse transformation in Equation 2.14. This ensured that the simulated void fraction fields would be more consistent with the experimentally observed bulk values.

To demonstrate the predictive performance of the correction factor, the approach was applied to a dataset that was not used during the derivation of the correlation. Specifically, the test was performed on the void fraction data corresponding to a fixed liquid superficial velocity of  $j_d = 3.021$  m/s (taken from Figure 1 of the work by Triplett et al.) [93].

Table 3.2 gives an overview of the boundary superficial velocities, calculated parameters using the correction factor approach, the simulation void fraction result, the experimental void fraction results and the effective simulation correction factor iteratively obtained.

$u_c$	$u_d$	$u_{dc}$	$lpha_{th}$	Ψ	$\alpha_{ m corr}$	$\alpha_{ m sim}$	$\alpha_{\mathrm{exp}}$	$\alpha_{ m corr,eff}$
0.4119	3.021	0.1363	0.1196	6.17	0.738	0.120	0.1252	≈ 0.65
1.9700	3.021	0.6521	0.2319	1.73	0.401	0.178	0.3546	$\approx 0.60$
9.6900	3.021	3.2075	0.4550	1.00	0.455	0.46	0.6060	$\approx 0.50$

**Table 3.2:** Overview of the predictive performance of the correlation factor  $\Psi$ .

As shown in Table 3.2, the general trend is an underprediction of the experimental surface-averaged void fraction  $\alpha_{\rm exp}$ . This underprediction is relatively mild when the theoretical void fraction  $\alpha_{\rm th}$  is close to the experimental value (as seen in the first row) indicating that the correction factor  $\Psi$  performs well when applied to a reasonable theoretical starting point.

However, in the second and third rows,  $\alpha_{th}$  significantly underestimates  $\alpha_{exp}$ , resulting in also a bad value for  $\alpha_{sim}$ . This suggests that the primary source of error is not the

66 3. Results & Discussion

correction factor itself, but rather the initial theoretical estimate. When  $\alpha_{th}$  is too low, even a well-calibrated correction factor may not fully compensate, leading to persistent underprediction in the final simulation value  $\alpha_{sim}$ .

It is however important to emphasize that these underpredictions are not unexpected. The correction equations used in this work were derived from a limited and somewhat noisy dataset, relying on simple empirical curve fitting for a very complex problem (void fraction distribution). While the correction factor offers a practical and computationally inexpensive method to approximate void fraction initialization, it is ultimately a cheap solution.

For improved robustness and accuracy across the entire operational range, future work could consider developing a more physics-informed correlation (incorporating channel geometry, bubbly dynamics coefficients number,...). Alternatively, machine learning regression on high-fidelity datasets or analytical closure models based on interfacial momentum balance may also provide enhanced predictive capabilities.

#### 3.2.3 Pressure Drops

After the correction factor was shown to reliably (enough) predict the initial void fraction conditions for the numerical simulations, this methodology was adapted to the pressure drop simulations, since no void fraction data was available for these specific velocity cases.

In this study, the pressure drop was evaluated for three distinct continuous-phase superficial velocities: case A ( $j_c = 0.156 \text{ m/s}$ ), case B ( $j_c = 0.515 \text{ m/s}$ ), and case C ( $j_c = 3.018 \text{ m/s}$ ). These values were not chosen arbitrarily. Rather, they were selected to span a representative range of velocity ratios ( $j_d/j_c$ ), where case A typically features ratios greater than 1, case B hovers around 1, and case C presents ratios well below 1. This approach ensures that the model is tested across a broad input space, reducing the risk of overfitting to a narrow operational regime. For every continuous-phase velocity, simulations were performed over a set of 8–10 different dispersed-phase superficial velocities ( $j_d$ ), capturing a wide range of two-phase flow conditions. Figure 3.11 - Figure 3.13 visualize the pressure drop in function of the superficial gas velocity.

#### 3.2.3.1 Case A: High Velocity Ratio

Tab	le 3.3:	Experimental	data, ti	heoretical	calcul	ated	parameters and	l simul	lation	results	for case A	₹.
-----	---------	--------------	----------	------------	--------	------	----------------	---------	--------	---------	------------	----

Exp Nr.	$u_d$	$u_c$	$\alpha_{th}$	Ψ	$\alpha_{\mathrm{in}}$	$\Delta P_{\rm sim} (k Pa)$	$\Delta P_{\rm exp}  ({\rm kPa})$
1	0.041	0.156	0.1579	3.6200	0.5716	0.473	0.603
2	0.165	0.156	0.2846	1.0000	0.2846	0.810	1.130
3	0.515	0.156	0.4606	1.0000	0.4606	2.236	1.849
4	0.917	0.156	0.5879	1.0000	0.5879	3.200	2.191
5	1.430	0.156	0.7094	1.0000	0.7094	3.623	2.385
6	2.679	0.156	0.9252	1.0000	0.9252	4.259	2.467

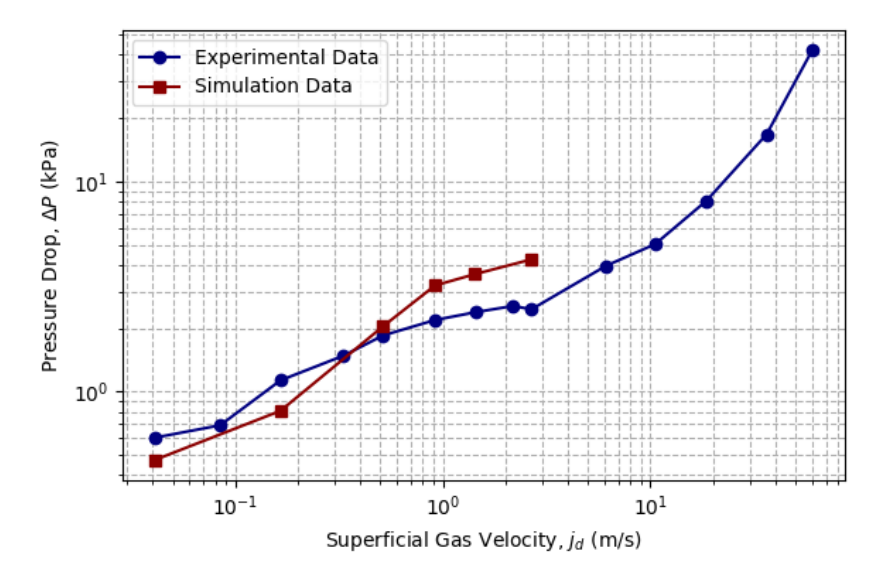


**Figure 3.11:** Simulated vs. experimental pressure drop results for case A ( $j_c = 0.156 \text{ m/s}$ ).

# 3.2.3.2 Case B: Normal Velocity Ratio

**Table 3.4:** Experimental data, theoretical parameters, and simulation results for Case B

Exp Nr.	$u_d$	$u_c$	$\alpha_{th}$	Ψ	$\alpha_{in}$	$\Delta P_{\text{sim}} \text{ (kPa)}$	$\Delta P_{\rm exp} \ ({\rm kPa})$
1	0.04304	0.515	0.0973	9.1887	0.8937	0.333	2.118
2	0.12365	0.515	0.1520	3.8962	0.5921	0.650	2.874
3	0.42245	0.515	0.2556	1.4350	0.3667	0.944	3.707
4	0.82384	0.515	0.3390	1.0000	0.3390	1.210	4.863
5	1.40803	0.515	0.4253	1.0000	0.4253	1.745	6.944
6	3.01430	0.515	0.5868	1.0000	0.5868	6.280	6.827
7	5.35470	0.515	0.7483	1.0000	0.7483	8.225	10.433

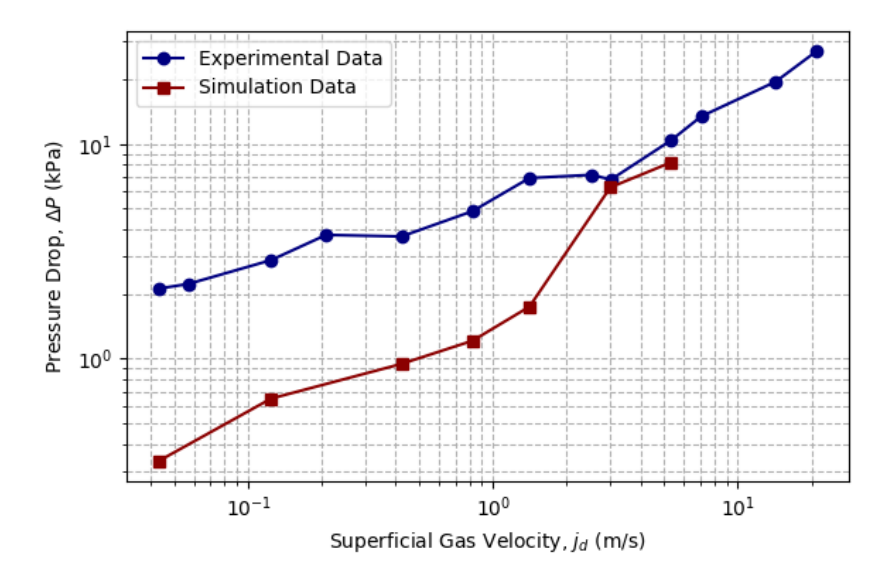


**Figure 3.12:** Simulated vs. experimental pressure drop results for case B ( $j_c = 0.515 \text{ m/s}$ ).

68 3. Results & Discussion

#### 3.2.3.3 Case C: Low Velocity Ratio

				•			-
Exp Nr.	$u_d$	$u_c$	$lpha_{th}$	Ψ	$\alpha_{in}$	$\Delta P_{\rm sim} (kPa)$	$\Delta P_{\rm exp} \ ({\rm kPa})$
1	0.264	3.018	0.0992	8.8540	0.8779	4.536	26.07
2	0.395	3.018	0.1176	6.3808	0.7502	8.600	29.86
3	0.858	3.018	0.1632	3.3961	0.5544	13.222	36.60
4	1.220	3.018	0.1895	2.5509	0.4833	17.569	44.11
5	2.010	3.018	0.2340	1.6998	0.3978	26.765	54.07
6	3.010	3.018	0.2776	1.2241	0.3398	48.172	58.85

**Table 3.5:** *Experimental data, theoretical parameters, and simulation results for Case C.* 

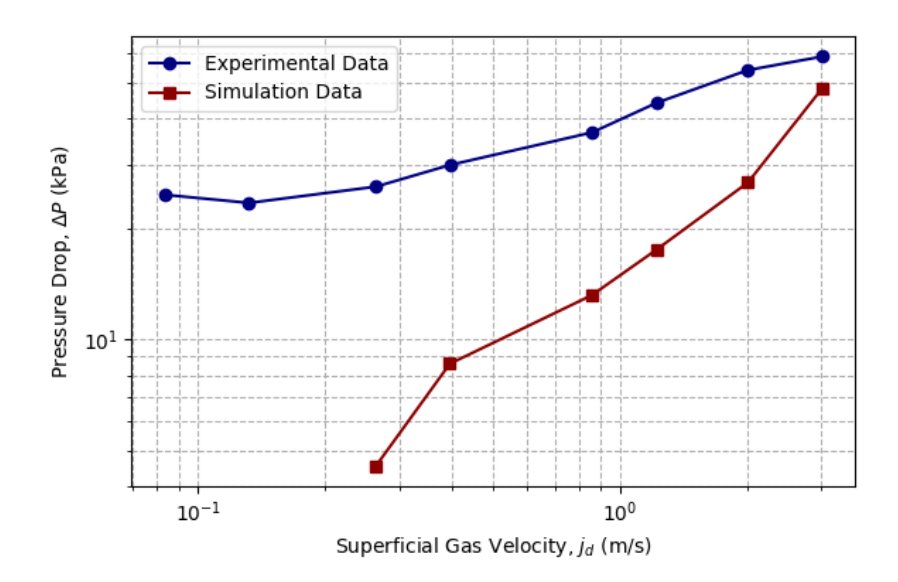


**Figure 3.13:** Simulated vs. experimental pressure drop results for case C ( $j_c = 3.018 \text{ m/s}$ ).

#### 3.2.3.4 Discussion of the Pressure Drop Results

The pressure drop results for all three velocity ratio cases are compared against experimental data in Figure 3.11, Figure 3.12, and Figure 3.13. While the overall trends are captured, the simulation exhibits varying degrees of agreement across the velocity ratio spectrum. Among the three cases, case A (high velocity ratio) shows the closest match with experimental measurements, as evidenced by both the shape and magnitude of the pressure drop curve. In contrast, case B (moderate velocity ratio) and case C (low velocity ratio) present notable discrepancies in magnitude. Nevertheless, the general shape of the simulation curves for cases B and C aligns decently with experimental trends. To further validate the applicability of the pressure drop simulations, it is observed that lower void fractions are generally associated with higher pressure drops. This behavior is primarily attributed to increased frictional losses under liquid-dominant conditions and aligns with established scaling relations commonly reported in transitional flow regimes [95].

3.2. Refined Model 69

To try to understand the model's predictive (in)accuracy, the superficial velocity ratio  $(j_d/j_c)$  was compared against the corresponding relative pressure drop error. The following key observations were made:

- For low velocity ratios  $(j_d/j_c < 1)$ , the relative error is large and negative, indicating that the simulation significantly underpredicts the pressure drop compared to experimental data.
- In the mid-range region  $(1 < j_d/j_c < 5)$ , the simulation begins to align more closely with experimental trends. This suggests a transition regime where the model performs better.
- At higher velocity ratios  $(j_d/j_c > 5)$ , the predicted pressure drop agrees well with experimental values.

From this can be concluded that the model performs better in regimes where gas (later vapor) clearly dominates, and struggles in transitional or liquid-dominant regimes where interfacial dynamics and turbulence effects become more complex to capture. This limitation is acceptable in the context of this work, as the primary focus lies on annular flow regimes, which typically develop under conditions of high velocity ratios. To better understand the model's better predictive performance at high velocity ratios and its reduced accuracy in lower velocity regimes, further analysis was carried out as presented in Section 3.2.4. This evaluation clarifies that the model performs well in predicting pressure drop in high velocity ratio scenarios primarily because it accurately captures the annular flow regime along with a reasonable prediction of the liquid film, as shown in Section 3.2.5. These features are typically dominant in high velocity ratio conditions. In contrast, lower velocity ratios often correspond to more complex and transitional flow regimes such as bubbly and slug flow. As illustrated in Figure 3.15b and Figure 3.16b, the model demonstrates clear difficulties in representing these regimes, which helps explain its reduced accuracy in pressure drop prediction under low velocity ratio conditions [96].

It is also worth emphasizing that simulation convergence was particularly challenging at both extremes of the velocity spectrum. These numerical instabilities are not attributed to deficiencies in the physical modeling itself (such as drag, lift, or wall lubrication forces), but rather to the extreme void fractions and velocity gradients involved. These conditions push the limits of numerical solvers and can lead to divergence or spurious oscillations in pressure and velocity fields.

Lastly (and perhaps most importantly) it must be reiterated that the void fraction plays a major role in accurately predicting the pressure drop. A key limitation of the current model (for this setup) lies in the simplifications used to estimate the initial void fraction distribution (correction factor  $\Psi$ ). While this method performs reasonably well at high superficial velocity ratios, it significantly underpredicts the initial void fraction in medium and low velocity regimes (as discussed in Section 3.2.2). This discrepancy is one of the dominant sources of deviation between the simulated and experimental pressure drops. Therefore, improving the initial void fraction modeling, could

markedly enhance the predictive capability of the model (for this setup) across the full velocity spectrum.

#### 3.2.4 Flow Regime Testing

During the simulation campaign aimed at collecting the necessary data to develop the correction factor  $(\Psi)$ , several distinct flow regimes were observed under varying inlet conditions. Four flow regimes (bubbly, slug, wavy-annular, and annular) were captured and are discussed below. For each case, experimental images taken from the work of Triplett et al. are presented above corresponding simulation results (for similar inlet superficial velocities) [3].

While the primary focus of this model was not to accurately capture flow regimes, the results nonetheless demonstrate that volume-averaged models, when appropriately optimized for specific regimes, have the potential to predict them with reasonable accuracy even within a simplified Eulerian–Eulerian formulation.

All simulation images presented in this section use a consistent void fraction color scale (unless specified), ranging from 0 (dark blue, pure liquid) to 1 (dark red, pure gas), to ensure visual comparability across different flow regimes:

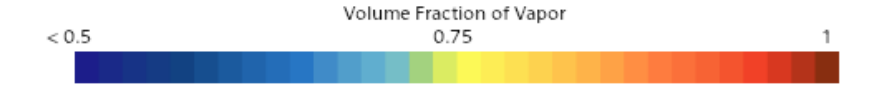


**Figure 3.14:** *Void fraction color scale used for all visualized flow regime results.* 

#### **3.2.4.1 Bubbly Flow**

The bubbly regime proved challenging to reproduce at low gas and liquid flow rates, with simulations showing limited agreement with experimental images from Triplett. In particular, the model struggled to accurately capture the bubble size and distribution. This limitation is well known for Eulerian–Eulerian frameworks, which often perform poorly in bubbly flows, especially in horizontal configurations, due to the limitations of volume-averaging techniques [90].

Accurately modeling dispersed bubbly structures typically requires interface-resolving methods, rather than averaged approaches [97]. Fundamentally, bubbly flows are highly sensitive to turbulent dispersion forces and require carefully tuned closure models. Standard models like Burns et al. tend to underperform in these regimes. Aternative formulations such as those proposed by Lavieville are often recommended for improved accuracy [48].

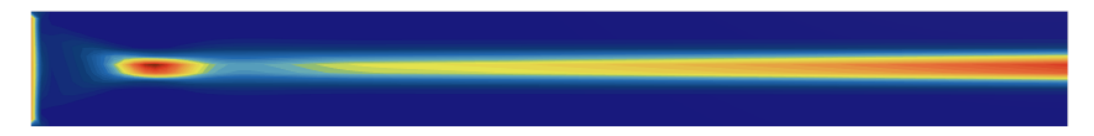
#### **3.2.4.2** Slug Flow

Particularly for the slug flow regime, the drag coefficient model proposed by Kendoush was tested for some cases in place of Tomiyama's drag coefficient. This substitution

3.2. Refined Model 71



(a) Experimental image of bubbly flow.

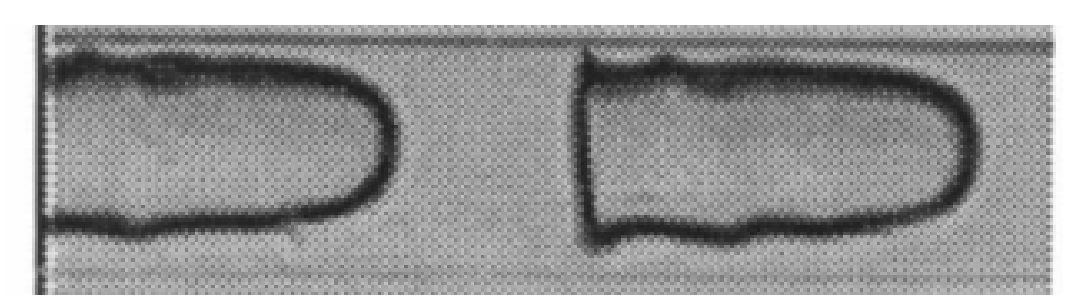


(b) Simulated bubbly flow.

**Figure 3.15:** *Comparison of experimental and simulated bubbly flow.* 

was motivated by the Kendoush model's specific applicability to elongated gas slugs in narrow channels, where interfacial curvature, confinement effects, and inertial drag become significant [64].

The simulation successfully reproduced the overall shape of a Taylor bubble, showing a rounded gas core separated by liquid slugs, consistent with experimental observations from Triplett (Figure 3.16). While the agreement is qualitatively decent, key features are still missing, most notably being that the liquid film is not well resolved. Additionally, no numerical convergence was achieved for this case, which limits the reliability of the result. Nonetheless, the case highlights the potential of tailored interfacial models like Kendoush's for capturing slug flow morphology, though further improvements in wall film modeling and solver stability are needed.



(a) Experimental image of Taylor (slug) flow.



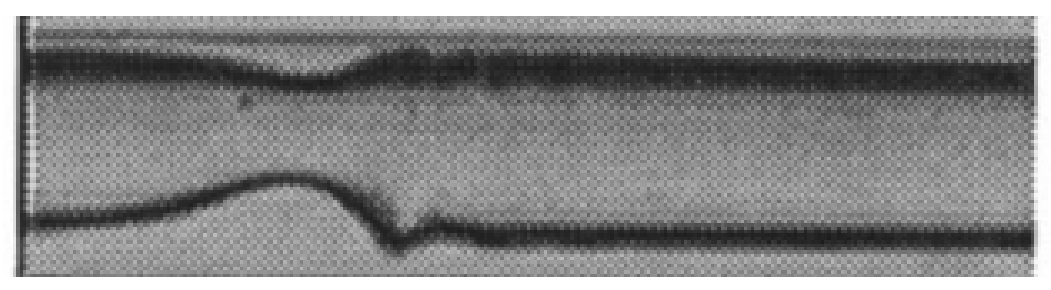
**(b)** *Simulated slug flow.* 

**Figure 3.16:** Comparison of experimental and simulated slug (Taylor) flow.

72 3. Results & Discussion

#### 3.2.4.3 Wavy-Annular Flow

Wavy-annular flow represents one of the transitional regimes, which are notoriously difficult to capture using Eulerian frameworks. Even the classification of such regimes remains a significant modeling challenge. [34]. This limitation is evident in Figure 3.17, where some qualitative similarities with the experimental image are present, but the flow on the left side lacks a clearly developed structure. This suggests that the agreement observed may be largely coincidental rather than the result of accurate physical modeling. It is also important to note that the void fraction on Figure 3.17 was capped at a maximum value of 0.4, which may visually suppress regions of higher gas concentration and affect the perceived structure of the flow.



(a) Experimental image of wavy-annular flow.



**(b)** Simulated wavy-annular flow.

**Figure 3.17:** Comparison of experimental and simulated wavy-annular flow.

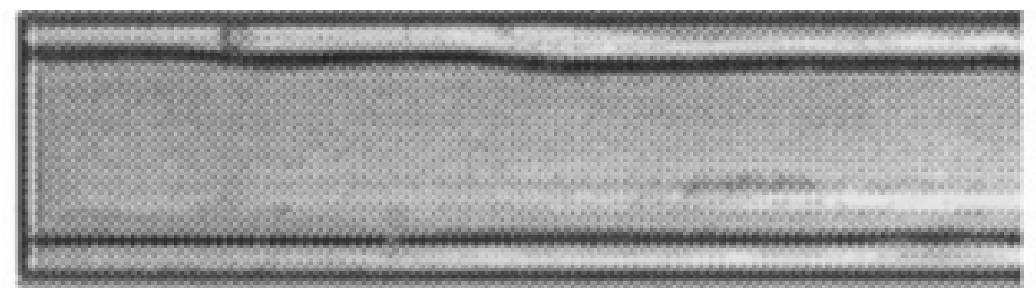
#### 3.2.4.4 Annular Flow

Annular flow was reproduced with the highest accuracy across a wide range of inlet velocities within the expected annular regime. This is to be expected, as the interfacial models were specifically selected and tuned to replicate annular flow behavior in microchannel geometries.

In the visual comparison (Figure 3.18, the simulated gas core appears slightly wider than in the experimental image from Triplett et al., or equivalently, the liquid film appears somewhat thinner. This discrepancy is likely influenced by the relatively low lift coefficient used in the simulations ( $C_L = -0.02$ ), which, in combination with the high gas interfacial velocities ( $j_g > 25 \text{m/s}$ ), may reduce the lateral migration of bubbles toward the center, thereby narrowing the predicted liquid film.

The accuracy of the simulated liquid film thickness is further analyzed in Section 3.2.5, where it is compared against both experimental datasets and theoretical models. Overall, the annular regime remains a strong validation case for the model's robustness in resolving phase-separated, high void fraction flow structures in microchannel environments.

3.2. Refined Model 73



(a) Experimental image of annular flow (Triplett).



(b) Simulated annular flow with gas core and thin peripheral liquid film.

**Figure 3.18:** Comparison of experimental and simulated annular flow.

#### 3.2.5 Liquid Film Comparison

In annular flow regimes, the liquid film thickness along the channel wall plays a critical role in determining heat and mass transfer performance. Accurately capturing this film is essential for reliable CFD predictions in microscale two-phase flows. In this section, the simulated film thicknesses are compared with experimental data inferred from Triplett's flow visualizations, a theoretical correlation proposed by Fukano and Kariyasaki, and the results of the simulations [98].

The empirical correlation used is given by:

$$\frac{\delta_m}{D} = 0.082 \exp\left\{-0.0594 \operatorname{Re}_L^{0.21} \chi^{0.12} Fr_G^{0.25}\right\}$$
 (3.1)

where  $\delta_m$  is the mean liquid film thickness and D is the hydraulic diameter.

Table 3.6 summarizes the superficial velocities and resulting film thicknesses for the theoretical prediction and simulation output:

<b>Table 3.6:</b> Comparison o	f t	heoretical, and	l simula	ated li	iquid	film	thicknesses	in	μm.
--------------------------------	-----	-----------------	----------	---------	-------	------	-------------	----	-----

Case Nr.	$j_L$ [m/s]	$j_G$ [m/s]	$\delta_{m,theor}$	$\delta_{m,s\bar{i}m}$
1	0.2	5	69.6	107.226
2	0.3	7.5	64.99	60.43
3	0.4	10	61.44	46.21
4	0.5	14	57.53	32.6
5	0.6	18	54.02	-

Figure 3.20 visualizes the corresponding simulation snapshots of the liquid film for each case to support the comparison:

Figure 3.19 presents the predicted liquid film thicknesses from the simulations and experimental data (Triplett), plotted against the theoretical model proposed by Fukano. The log-log plot includes  $\pm 25\%$  deviation bounds around the theoretical curve to il-

74 3. Results & Discussion

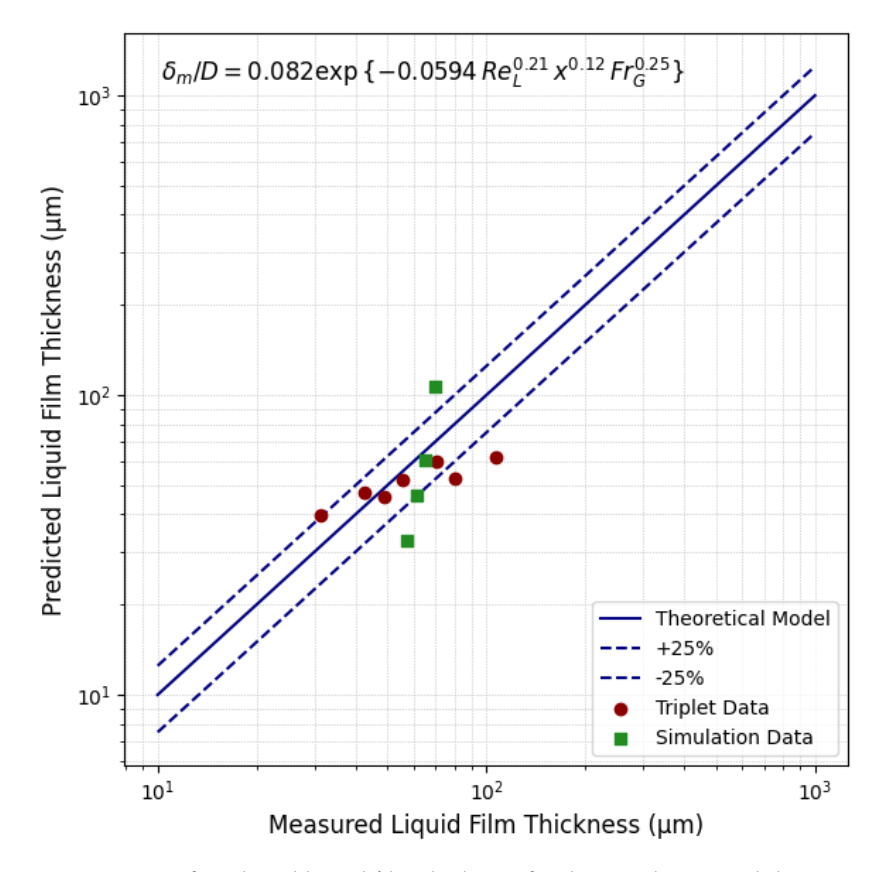


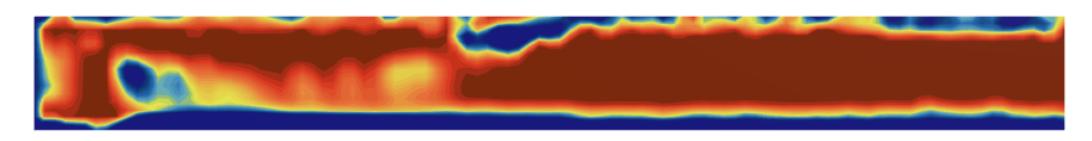
Figure 3.19: Comparison of predicted liquid film thickness for the simulation and the experimental data.

lustrate the model's expected accuracy range.

The tested simulation cases generally fall within or near these bounds, indicating reasonable agreement with the theoretical prediction. At lower flow conditions (case 1), the simulation tends to overpredict the film thickness, while at higher conditions (case 4), it underpredicts the film. For case 5, the film thickness could not be reliably extracted due to numerical instabilities. Despite these deviations, a clear "sweet spot" is observed at intermediate conditions (notably case 2), where simulation, theory, and experimental data align closely.

This comparison highlights that while volume-averaged Eulerian models may struggle to capture fine near-wall film dynamics in extreme regimes, they can still predict annular film thickness with reasonable accuracy when appropriately calibrated for specific operating conditions. Further improvements may be achieved through local mesh refinement and the application of regime-specific interfacial closure models.

3.2. Refined Model 75



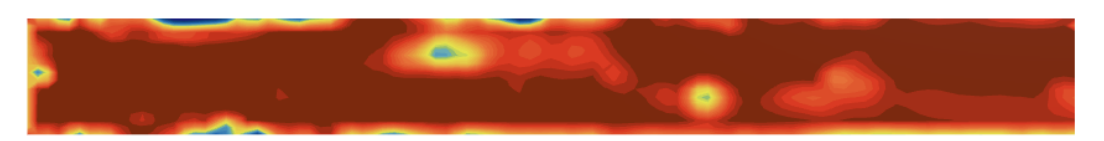
(a) Case 1: Highly chaotic and unstable liquid film formation.



**(b)** Case 2: Well-developed and stable liquid film around the wall.



**(c)** *Case 3: Uniform and thin but stable liquid film distribution.* 



(d) Case 4: Gradual disappearance of the liquid film, indicating instability.



 $(\mathbf{e})$  Case 5: Complete disappearance of the wall-adjacent liquid film.

**Figure 3.20:** Visualization of simulated liquid film behavior across five representative cases, highlighting transitions from stable to unstable regimes and eventual film depletion.

# 3.3 Boiling Model

The primary objective of the boiling model was to extend the interfacial closure framework developed for the adiabatic cases to capture key phase-change phenomena. Specifically, it aimed to predict pressure drop behavior, annular flow dynamics, liquid film evolution, and wall superheat under boiling conditions. These phenomena were analyzed to gain deeper insight into the underlying mechanisms. The simulation results were subsequently validated against the experimental data reported by Sumith et al. [5].

#### 3.3.1 Pressure Drop

The most critical parameter for validating the boiling model is, without a doubt, the pressure drop, as emphasized multiple times throughout this thesis. To assess the accuracy of the developed model, the numerical results were compared against the experimental data from Sumith et al. [5]. A visual comparison is presented in Figure 3.21, illustrating the agreement between simulation and experiment.

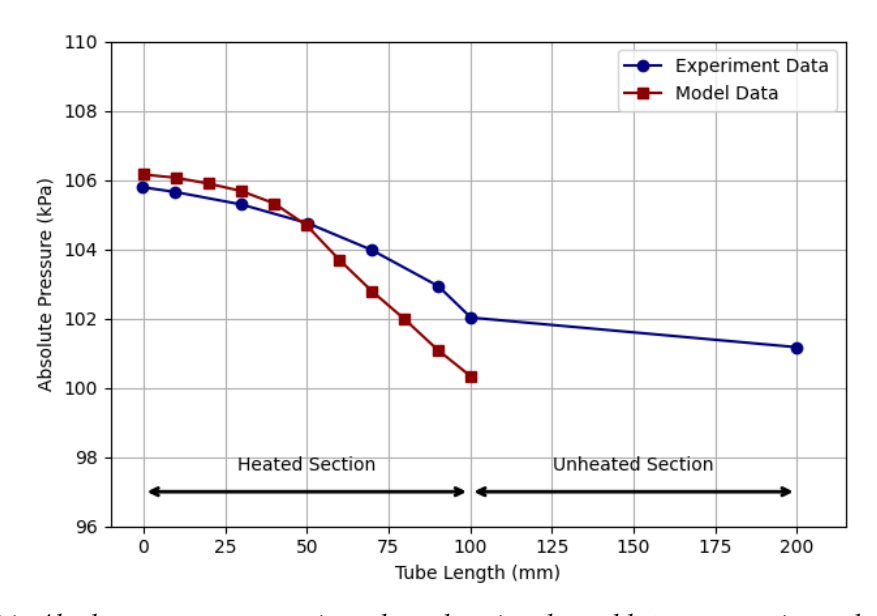


**Figure 3.21:** Absolute pressure comparison along the microchannel between experimental and simulation

The model accurately reproduced the expected pressure drop profile, maintaining an average relative error of 0.93%. No datapoints were collected in the unheated region due to time constraints during data acquisition. Additionally, the development of annular flow and the formation of a liquid film along the wall were clearly visible in the simulated void fraction cross-sections, as illustrated on Figure 3.22.

The deviation observed in the second part of the heated section (> 50 mm) can be explained using Figure 3.22 and by considering the dominant heat transfer mechanism in this region. Specifically, heat is primarily removed through forced convective vaporization of a thin annular liquid film, which develops due to the annular flow [99]. As

3.3. Boiling Model 77

discussed before in Section 3.2.5, the model is capable of predicting and sustaining liquid films with reasonable accuracy. However, its predictive capacity is limited across a broader range of operating conditions. So, when the simulated liquid film is thinner (or absent) in a given region, the local heat transfer coefficient is reduced. This leads to lower vapor generation rates, fewer bubbles, and increased liquid friction, ultimately resulting in higher frictional pressure losses. This cascade effect helps explain the slight overprediction of the pressure drop observed in this part of the domain. Conversely, toward the other end of the heated section, the model appears to slightly overpredict the liquid film thickness, leading to excessive vapor production, reduced friction, and thus an underprediction of the pressure drop compared to the experimental data.

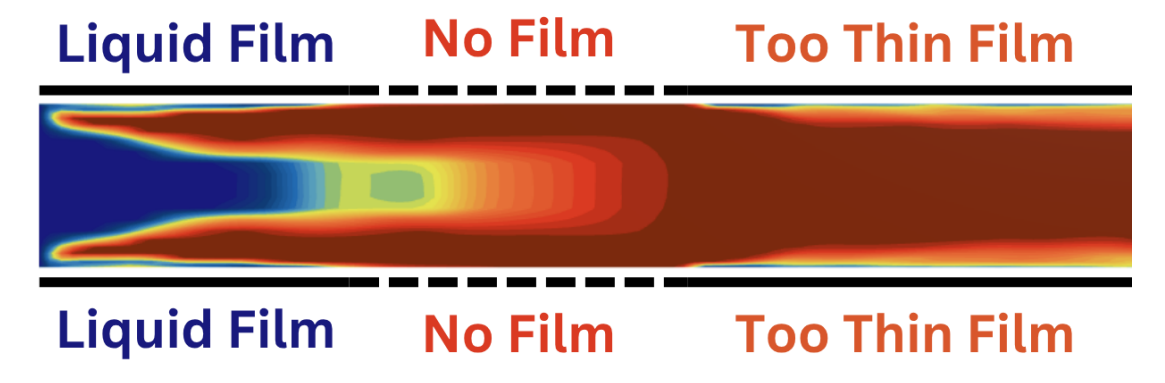


**Figure 3.22:** Liquid film thickness along the microchannel at  $Q = 151 kW/m^2$ 

Identifying the exact cause of the overly thick or thin liquid film based solely on the available data is not feasible. It is likely the result of a complex interplay between the self-sustaining boiling coefficients and the interfacial forces. Given that the MITB wall boiling model has been validated across a wide range of operating conditions, it is more probable that one of the lateral interfacial forces is responsible. Notably, the wall lubrication force, which is often crucial in stabilizing the near wall liquid distribution, was not included due to numerical instabilities. As a result, the precise cause remains uncertain as a lack of an accurate prediction model for the liquid film thickness remains [17].

This same logic can also be used to explain the slight deviation in the wall temperature profile. While the relative average error remains below 0.68%, the simulated wall temperatures are slightly higher than the experimental values, especially in the first part of the heated pipe. The delayed development of the liquid film in the early part of the channel, which limits heat transfer from the wall to the fluid. As a result, less energy is used for phase change, and more is retained as sensible heat in the wall, increasing the local wall temperature.

When comparing the present results to other CFD studies employing similar mass flux (G) and heat flux (Q) conditions, good agreement is observed. The trends and magnitudes are consistent with those reported in the literature, such as the work by Höhne et al. [100].

78 3. Results & Discussion

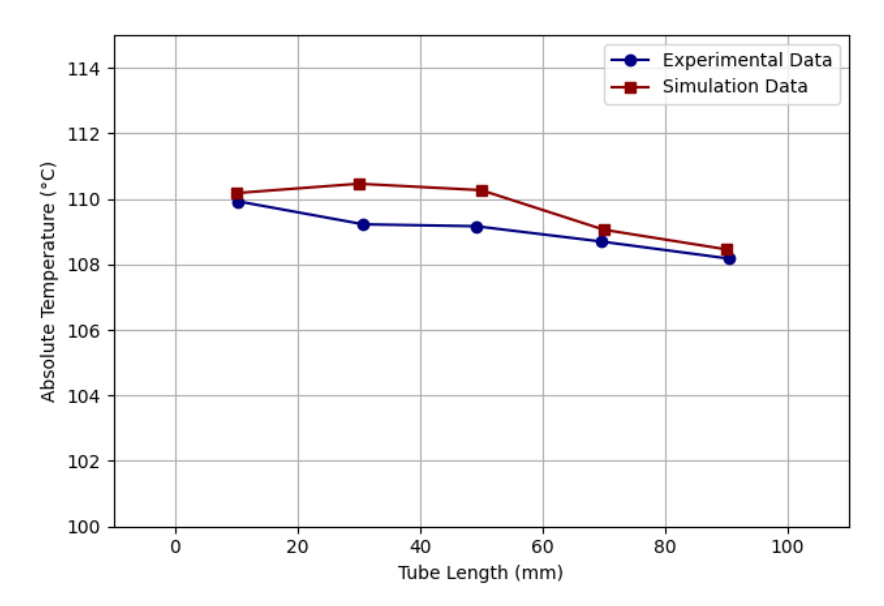


**Figure 3.23:** Absolute temperature comparison along the microchannel between experimental and simulation

#### 3.3.2 Wall Superheat Behavior

To further validate and assess the predictive capability of the boiling model, as well as to identify areas for improvement, the wall superheat was analyzed for two mass flux conditions ( $G = 71 \text{ kg/m}^2\text{s}$  and  $G = 106.5 \text{ kg/m}^2\text{s}$ ) under various applied heat fluxes to investigate liquid film stability and detect possible transitions in the dominant flow regimes. Additionally, the wall superheat difference ( $\Delta T_{max} - \Delta T_{min}$ ) was studied at  $G = 106.5 \text{ kg/m}^2\text{s}$ .

#### 3.3.2.1 Wall Temperature and Heat Flux Response

Prior to analyzing the wall superheat, a baseline validation was performed by comparing the simulated average wall temperatures with experimental results reported by Sumith et al. [5], across four distinct heat flux conditions at  $G=106.5 \text{ kg/m}^2\text{s}$ . The comparison is summarized in Table 3.7. Good agreement was found, confirming that the model correctly resolves the wall heat transfer response under boiling conditions.

**Table 3.7:** Comparison of imposed heat fluxes and wall temperature response at  $G = 106.5 \text{ kg/m}^2\text{s}$ .

Heat Flux [kW/m <sup>2</sup> ]	Wall Temperature Exp [°C]	Wall Temperature Simu [°C]
36	$101.82 \pm 0.83$	$102.84 \pm 0.25$
101	$105.87 \pm 0.60$	$107.17 \pm 0.14$
209	$110.77 \pm 1.25$	$110.9 \pm 3.2$
589	$132.20 \pm 7.5$	$126.8 \pm 5.6$

3.3. Boiling Model 79

#### 3.3.2.2 Wall Superheating Trends

Following this validation, the evolution of the wall superheat with increasing heat flux was investigated. In the experimental data, two "turning" points (1 & 2) are observed for both the mass fluxes. These points correspond to transition zones for flow (2) and heat transfer (1) regimes [5]. In the transition zone for flow regime, the regime changes from nucleate boiling to an annular flow. In the transition zone for heat transfer the dominant heat transfer mechanism shifts from only thin liquid film evaporation to partial thin liquid film evaporation and partially wall dry-out.

Figure 3.24 describes these turning points together with additional points (A & B) corresponding to different simulations void fraction profiles (see Figure 3.25) to demonstrate the change in heat transfer mechanism that was observed in different simulations to confirm the transition zones.

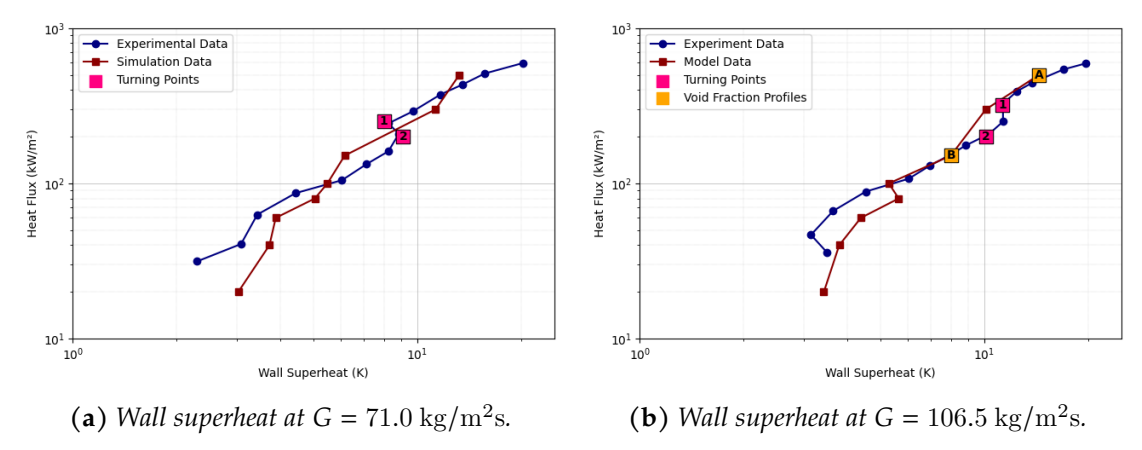
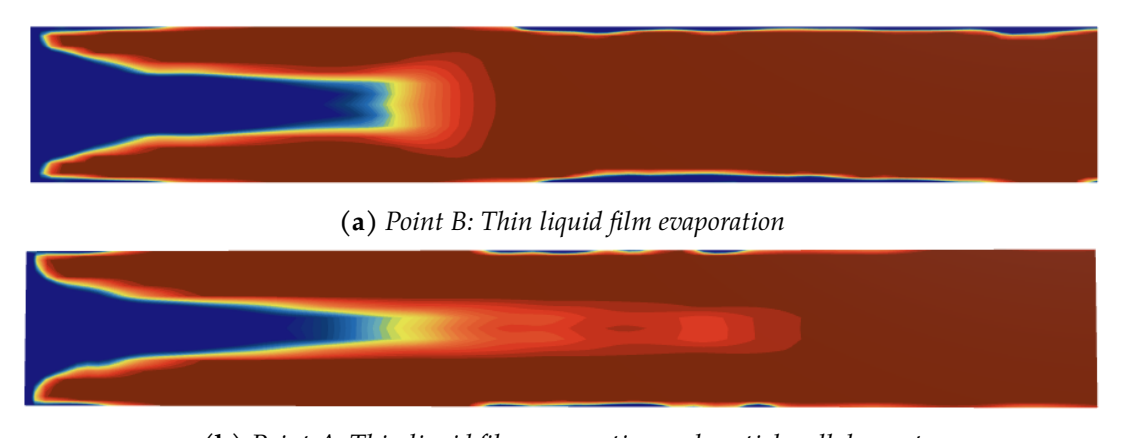


**Figure 3.24:** Wall superheat under varying heat fluxes for different mass fluxes together with the pool boiling correlation and crusical points A & B.



(b) Point A: Thin liquid film evaporation and partial wall dry-out

Figure 3.25: Differences is dominant heat transfer mechanism

Although a local heat transfer coefficient was also evaluated  $(h_y)$ , the model tended to overpredict its magnitude, typically by a factor between 1.3 and 2.0. Due to this discrepancy and lack of experimental resolution for local effects, no further investigation was carried out regarding quality-dependent local heat transfer phenomena. Future

work could focus on correlating the heat transfer coefficient with flow regimes and identifying transition zones while validating against Sumith's data [5].

#### 3.3.2.3 Wall Superheat Difference

To further assess film dynamics and wall boiling stability, the difference in maximum and minimum wall superheat along the channel height was analyzed (at  $G = 106.5 \,\mathrm{kg/m^2s}$ ).

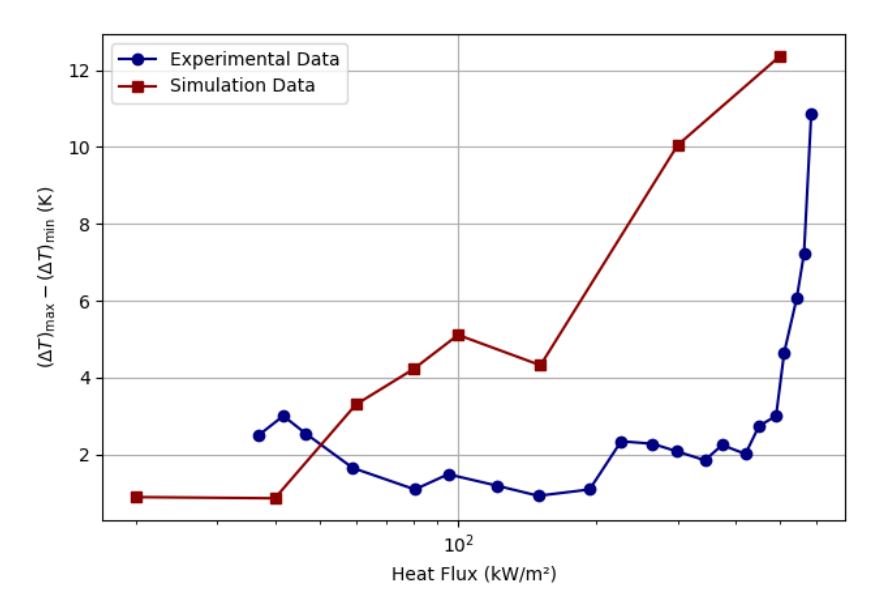


**Figure 3.26:** Wall superheat difference along the flow direction for  $G = 106.5 \text{ kg/m}^2\text{s}$ .

Figure 3.26 compares the simulation results to experimental data. The simulation consistently predicts a larger difference between maximum and minimum wall superheat temperatures as the heat flux increases. This may indicate a localization of heat transfer or film thinning in certain regions, which deviates from the more uniformly distributed thermal response observed in the experiment. These discrepancies point out the need for improved modeling of the wall heat transfer mechanisms.

#### 3.3.3 Mesh Sensitivity Analysis

Lastly, to assess the robustness of the numerical predictions, a mesh sensitivity analysis was conducted by varying the base mesh size across three levels: 0.1 mm, 0.05 mm, and 0.025 mm as stated in Section 2.3.1. The impact on key simulation outputs, including void fraction distribution, liquid film formation and pressure drop were systematically evaluated. Additionally, a quadrilateral mesh was compared against the 0.1 mm base mesh case. This comparison served to validate the selected base mesh as a good compromise between computational cost and numerical accuracy.

#### 3.3.3.1 Baze Size Comparison

**Void Fraction and Liquid Film Distribution** A clear distinction in void fraction behavior emerges across the different mesh resolutions. Interestingly, mesh refinement

3.3. Boiling Model 81

did not lead to improved predictions of void structure or liquid film formation. The original base mesh of 0.1 mm yielded the most physically consistent results, with a stable annular flow and clean liquid film along the walls. The 0.025 mm mesh produced a partially developed film with intermittent wetting, while the 0.05 mm mesh showed almost exclusively dry-wall regions. Additionally, both refined meshes (0.05 mm and 0.025 mm) exhibited signs of inverted annular flow, with liquid occupying some of the center of the channel, contrary to expected behavior. A detailed comparison of these effects is presented in Figure 3.27. It is important to note that the 0.05 mm mesh had more internal divisions then the 0.025 mm mesh implying that the division might influence the liquid film formation and void fraction distribution more then the base size.

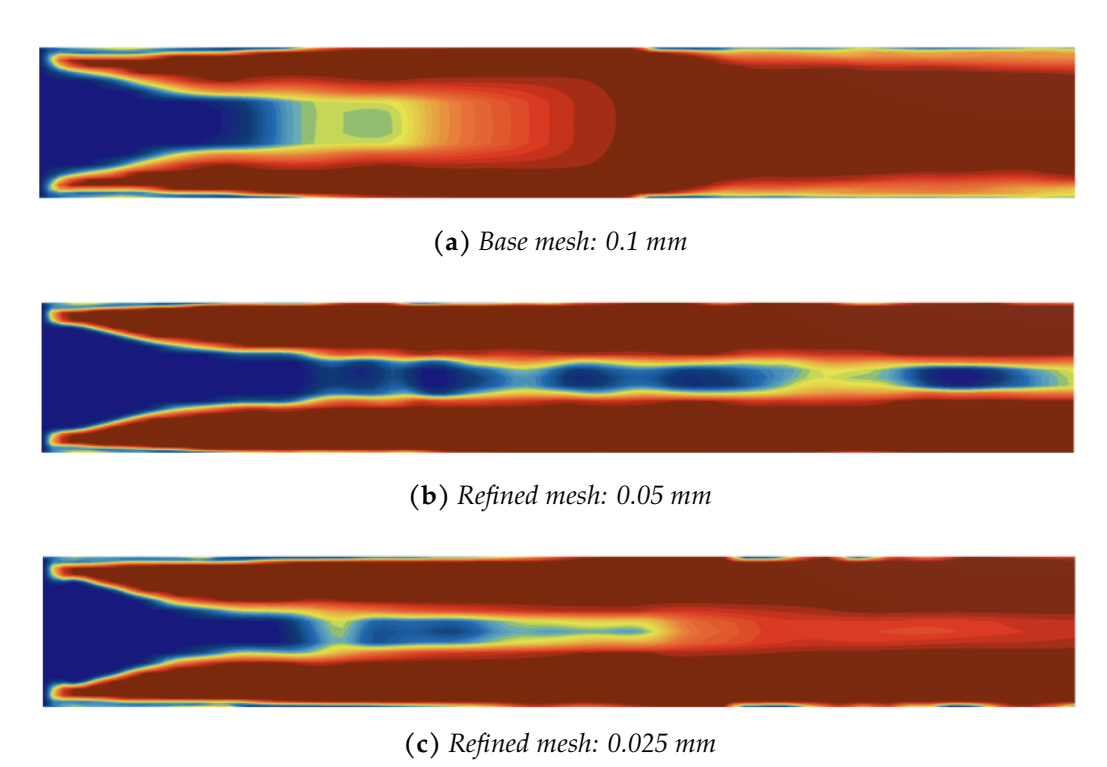


**Figure 3.27:** *Comparison of void fraction field across different mesh resolutions.* 

**Pressure Drop** The most notable observation from the pressure drop analysis is that all simulations converge to the same outlet pressure, indicating that a fixed outlet boundary condition may have been unintentionally applied. Nevertheless, differences appear along the channel.

The simulation using the 0.025 mm mesh showed excellent agreement with experimental pressure drop in the first half of the channel, with an average deviation of only 0.6% over the first six points. In contrast, all meshes underpredict the pressure drop in the second half of the heated region. This suggests that while mesh resolution influences early development, the observed discrepancies in the second half likely stem from physical modeling limitations rather than mesh resolution.

82 3. Results & Discussion

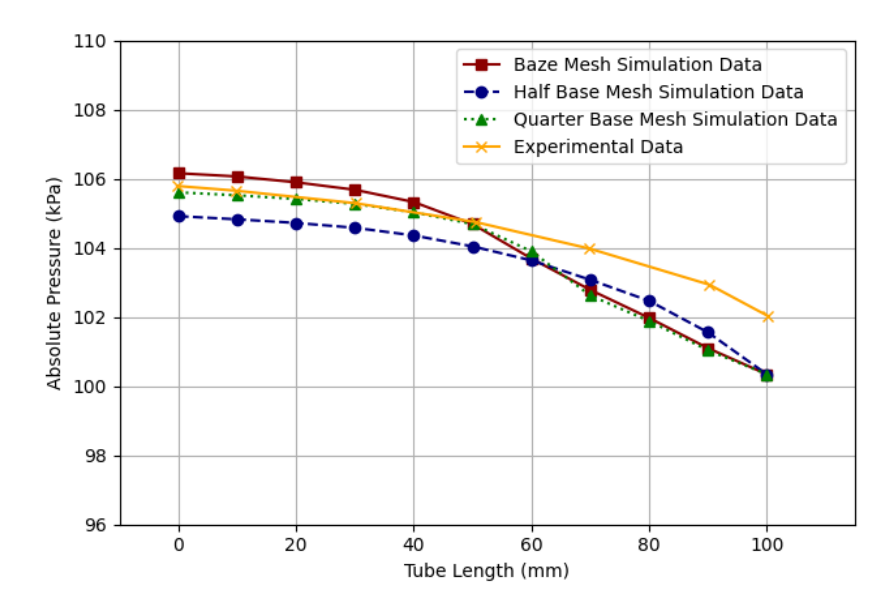
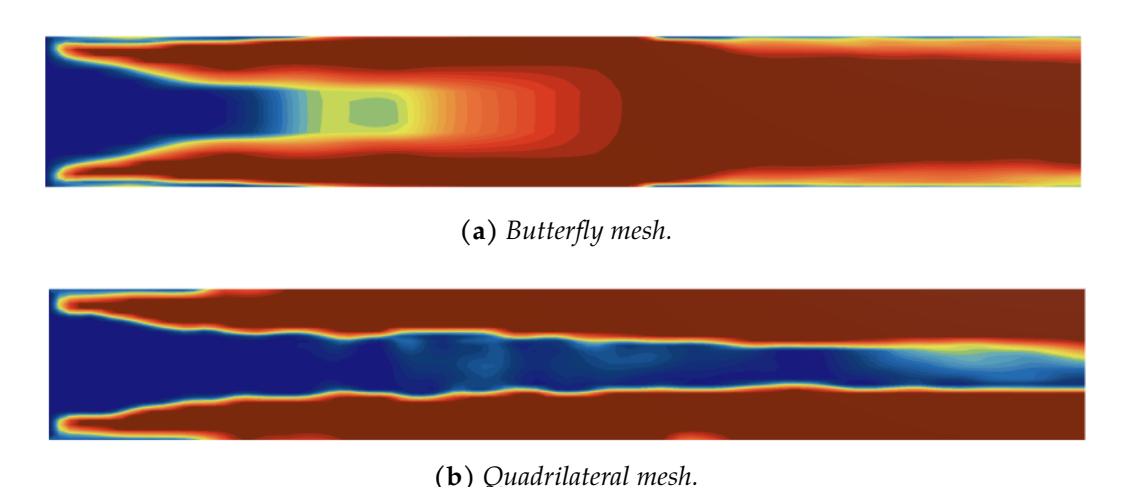


Figure 3.28: Pressure drop prediction for different mesh resolutions.

**Conclusion** In summary, the 0.1 mm base mesh offers the most reliable film structure and flow regime prediction, while the strongly refinement (0.025 mm) can improve pressure drop accuracy in the channel's early regions. However, finer meshes introduce physical artifacts such as inverted annular flow and do not improve prediction in the latter half, where modeling limitations dominate.

#### 3.3.3.2 Butterfly vs Quadrilateral Comparison

**Void Fraction and Liquid Film Distribution** The quadrilateral mesh (completely) fails to reproduce the expected annular flow pattern. Instead, it yields an inverted annular structure where liquid is concentrated in the core and shows no evidence of a liquid film. In contrast, the butterfly mesh consistently generates the correct annular flow with a well-defined liquid film along the channel walls. This stark difference is visualized in Figure 3.29.



**Figure 3.29:** Comparison of void fraction distribution across mesh types.

3.3. Boiling Model 83

**Pressure Drop** The quadrilateral mesh also manages to reproduce the general pressure drop trend, albeit with a slightly larger deviation from expected results (Figure 3.30. However, it is important to note that achieving convergence for the quadrilateral case took approximately four to five times longer than the butterfly mesh, indicating significantly lower numerical efficiency.

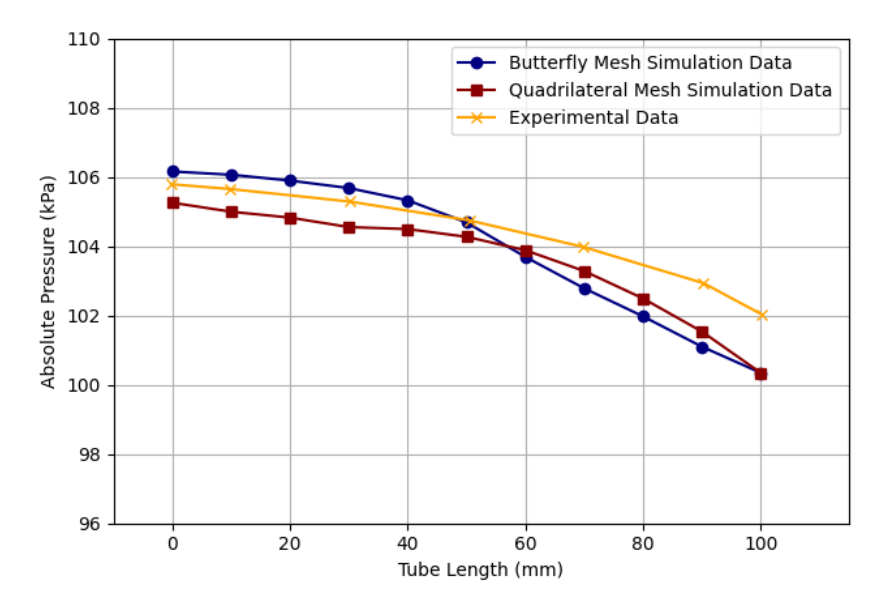


**Figure 3.30:** *Pressure drop comparison between butterfly and quadrilateral mesh simulations.* 

**Conclusion** Although the quadrilateral mesh was able to capture the overall pressure drop, it is clearly inferior to the butterfly mesh. It requires more computational effort and fails to correctly represent the interfacial dynamics and annular flow structure. As such, the butterfly mesh remains the preferred choice for accurate and efficient two-phase boiling flow simulations.

#### 3.3.4 Turbulence Analysis

An attempt was made to test the k- $\omega$  turbulence model, but simulations failed when using the custom MITB sub-models (especially those for nucleation site density, bubble departure diameter and frequency, wall area fraction, and quenching heat transfer coefficient). A turbulence model sensitivity study was initially planned to assess the influence of turbulence modeling on two-phase structures and wall heat transfer. Given the strong role of turbulence in boundary layer development, its accurate modeling is essential in boiling flows.

However, due to numerical instability and limited time, this analysis was postponed. Future work should examine how different models, such as standard k- $\varepsilon$ , realizable k- $\varepsilon$ , and SST k- $\omega$ , affect film dynamics, regime transitions, and heat transfer accuracy.

# 4

# Conclusions and Future Developments

#### 4.1 Conclusions

This thesis set out to investigate whether a Computational Fluid Dynamics model, based on the Eulerian–Eulerian approach, could be developed and validated for simulating adiabatic and diabatic two-phase flows in a single microchannel, with a particular focus on its future extendability to Microchannel Heat Exchangerss model for Small Module Reactors applications.

To address this, a progressive modeling strategy was adopted. First, a baseline adiabatic model was constructed to gain familiarity with CFD and to validate flow behavior in vertical small channel geometries [87]. This was followed by a refined adiabatic model, where more appropriate interfacial force models were selected with a view toward future extension to boiling conditions. The refined model was validated against the horizontal microchannel setup from Triplett [3]. Finally, a boiling-capable extension of the refined model was developed by incorporating wall boiling and boiling bubble dynamics to reproduce the experimental setup of Sumith et al. [5].

#### 4.1.1 Baseline Model

The central goal of the baseline model was to reproduced the main fluid-dynamics features (void fraction and velocity profiles) of adiabatic two-phase flow in a vertical small-diameter channel.

Across all cases, both velocity and void fraction profiles showed good agreement with experimental and numerical reference data. In the upper near wall region of the pipe (where interfacial dynamics are most critical) the predicted void distributions closely matched experimental observations, confirming the suitability of the selected interfacial force models. For lower void fractions, small shifts in the radial profiles were observed, likely due to the linear void-fraction dependence of the wall lubrication model.

4.1. Conclusions 85

The liquid velocity profile results also aligned well with experiments, a 2D comparison against Ekambara's data supported these findings. The mesh sensitivity study further emphasized the importance of near-wall resolution, particularly for void fraction predictions. Overall, the baseline model provided a numerically stable and physically accurate foundation small channel geometries.

#### 4.1.2 Refined Model

The main objective of the refined model was to predict the pressure drops, liquid film behavior, and identifying dominant flow regimes against Triplett's data, while preserving computational stability and keeping in mind the extendability to the boiling model.

The model was validated against three sets of pressure drop experiments representing different velocity ratios ( $u_{dc}$ ). It was found that the model shows good agreement with experimental trends in both shape and magnitude for high velocity ratios, while lower velocity ratios exhibited increasing discrepancies. These discrepancies were traced back to two key limitations: the void fraction initialization method (using the correction factor ( $\Psi$ ) and the inability of the model to capture complex flow regimes. The performed flow regime analysis supported this finding. Annular and wavy-annular flows were captured with good fidelity. Bubbly and slug regimes, however, showed poor agreement in both spatial structure and phase distribution. Lastly, the liquid film thickness was benchmarked against both experimental results and a theoretical correlation from Fukano [98]. Simulation results showed good agreement under intermediate flow conditions, validating the model's ability to reproduce mean film thickness for (non-extreme) annular flows. In conclusion, the refined model provides robust and accurate predictions for annular-dominant flow regimes in horizontal microchannels.

#### 4.1.3 Boiling Model

The goal of the boiling model was to successfully extended the adiabatic interfacial framework to simulate wall boiling two-phase pressure drops and heat transfer, specifically for annular flow, and compare it against experimental data of Sumith.

The model demonstrated very high accuracy in predicting average pressure drops and wall temperature. Slight over- and underpredictions of pressure drops were traced back to deviations in local liquid film thickness, influenced by not optimal or missing stabilizing forces. Wall superheat trends revealed clear turning points that correspond to heat transfer and flow regime transitions, aligned with literature. Although average wall temperatures matched well, local heat transfer coefficients were overestimated. Lastly, mesh sensitivity studies showed that base size is not the main factor influencing prediction accuracy or stability, but rather the number of divisions toward the channel center plays a more significant role. The butterfly mesh consistently outperformed quadrilateral mesh in reproducing realistic flow regimes and offered far better numerical convergence and computational efficiency.

### 4.1.4 Pressure Drop Comparison and General Conclusion

The refined adiabatic and diabatic models exhibit complementary strengths across different flow regimes. Both models show strong performance at high superficial velocity ratios  $(u_{dc})$ , where annular flow dominates and is accurately reproduced. However, the diabatic model achieves superior agreement with experimental results. This is primarily because the experimental pressure drop under boiling conditions,  $\left(\frac{dP}{dy}\right)_{\rm B}$ , is significantly higher than the corresponding single-phase (adiabatic) pressure gradient,  $\left(\frac{dP}{dy}\right)_{\rm ST}$ , in the annular flow regime. As a result, the total pressure drop in the diabatic simulations, given by  $\left(\frac{dP}{dy}\right)_{\rm T} = \left(\frac{dP}{dy}\right)_{\rm B} + \left(\frac{dP}{dy}\right)_{\rm ST}$ , aligns more closely with experimental measurements. This indicates that the diabatic sub-model (MITB) currently provides sufficient predictive accuracy and does not require immediate refinement. Instead, future improvements should focus on enhancing the adiabatic pressure drop component, which remains the dominant source of error.

Overall, the developed models (particularly the boiling model) demonstrated strong thermo-hydraulic predictive capabilities in annular flow regimes, while also identifying the key sources of deviation and modeling challenges that persist across broader operating conditions.

# 4.2 Future Developments

While annular flow regimes (expected to dominate in MCHEs for SMRs) were well resolved, the model exhibits significant limitations in transitional and liquid-dominant regimes, particularly at lower relative velocities. These challenges were evident in both the flow regime analysis and pressure drop deviations.

To extend the model's applicability, future work should focus on developing more generalized and interconnected interfacial force formulations. This could involve rethinking traditional interpretations (like Lubchenko did for the wall lubrication force) and also try integrating them with boiling physics. For example, one could derive the Lubchenko model with the bubble departure diameter (instead of constant spherical) proposed by MITB to create a more adaptive, regime-sensitive model. Another possible method involves the application of machine learning techniques to improve model calibration or identify dominant interfacial mechanisms across flow regimes [101]. Such enhancements would improve performance in other flow regimes, ultimately increasing the accuracy of pressure drop predictions across a wider range of conditions. However, it cannot be overstated how complex this task is within the constraints of volume-averaged methods such as the Eulerian–Eulerian approach.

From this point, two main development paths for the future are possible. The first focuses on improving the model's generalizability before scaling to multi-channel configurations. This would involve robust validation and refinement of interfacial closures to ensure reliable predictions across all relevant flow regimes. The second path assumes annular flow predominance and proceeds directly to multi-channel modeling based

87

on the current framework. Although this assumption may not be justified by the used geometry of the MCHE.

In either case, both paths eventually converge: the model must be extended to realistic, multi-channel MCHE geometries, which includes simulating interacting flow paths and validating thermo-hydraulic outputs. Ultimately, by incrementally increasing the model's geometric complexity, a fully detailed digital twin of a MCHE can be realized. Achieving this will mark a significant step toward using CFD as a predictive design tool for compact, high-efficiency heat exchangers in next-generation nuclear systems.

# Bibliography

- [1] P. A. Breeze, *Nuclear power*, ser. The power generation series. London, United Kingdom: Academic Press, 2017, includes bibliographical references. Print version record.
- [2] International Energy Agency, *Energy and AI*. Paris, France: International Energy Agency, 2024, ch. 2, pp. 49–86, world Energy Outlook Special Report. [Online]. Available: https://www.iea.org/reports/energy-and-ai
- [3] K. Triplett, S. Ghiaasiaan, S. Abdel-Khalik, and D. Sadowski, "Gas–liquid two-phase flow in microchannels part i: two-phase flow patterns," *International Journal of Multiphase Flow*, vol. 25, no. 3, pp. 377–394, Apr. 1999.
- [4] K. Bang, K. Kim, S. Lee, and B. Lee, "Pressure effect on flow boiling heat transfer of water in minichannels," *International Journal of Thermal Sciences*, vol. 50, no. 3, pp. 280–286, Mar. 2011.
- [5] B. Sumith, F. Kaminaga, and K. Matsumura, "Saturated flow boiling of water in a vertical small diameter tube," *Experimental Thermal and Fluid Science*, vol. 27, no. 7, pp. 789–801, Sep. 2003.
- [6] S. Laborie, C. Cabassud, L. Durand-Bourlier, and J. Lainé, "Characterisation of gas–liquid two-phase flow inside capillaries," *Chemical Engineering Science*, vol. 54, no. 23, pp. 5723–5735, Dec. 1999.
- [7] H. C. Kim, W.-P. Baek, and S. H. Chang, "Critical heat flux of water in vertical round tubes at low pressure and low flow conditions," *Nuclear Engineering and Design*, vol. 199, no. 1–2, pp. 49–73, Jun. 2000.
- [8] A. M. Lezzi, A. Niro, and G. P. Beretta, "Experimental data on chf for forced convection water boiling in long horizontal capillary tubes," in *Proceeding of International Heat Transfer Conference 10*. Begellhouse, 1994, pp. 491–496.
- [9] C. Shin, "Experimental study for pressure drop and flow instability of two-phaseflow in the pche-type steam generator for smrs," *Nuclear Engineering and Design*, vol. 318, pp. 109–118, 2017. [Online]. Available: https://www.sciencedirect.com/science/article/pii/S002954931730167X?via=ihub

[10] F. Verhaeghe, L.-S. Luo, and B. Blanpain, "Lattice boltzmann modeling of microchannel flow in slip flow regime," *Journal of Computational Physics*, vol. 228, no. 1, pp. 147–157, Jan. 2009.

- [11] S. Rassame and T. Hibiki, "Drift-flux correlation for gas-liquid two-phase flow in a horizontal pipe," *International Journal of Heat and Fluid Flow*, vol. 69, pp. 33–42, Feb. 2018.
- [12] T. Hibiki, "One-dimensional drift-flux correlations for two-phase flow in medium-size channels," *Experimental and Computational Multiphase Flow*, vol. 1, no. 2, pp. 85–100, Apr. 2019.
- [13] S. Mohanty, O. Parkash, and R. Arora, "Analytical and comparative investigations on counter flow heat exchanger using computational fluid dynamics," *Journal of Computational & Applied Research in Mechanical Engineering (JCARME)*, 2019.
- [14] K. Foli, T. Okabe, M. Olhofer, Y. Jin, and B. Sendhoff, "Optimization of micro heat exchanger: Cfd, analytical approach and multi-objective evolutionary algorithms," *International Journal of Heat and Mass Transfer*, vol. 49, no. 5–6, pp. 1090–1099, Mar. 2006.
- [15] K. Ekambara, R. Sanders, K. Nandakumar, and J. Masliyah, "Cfd simulation of bubbly two-phase flow in horizontal pipes," *Chemical Engineering Journal*, vol. 144, no. 2, pp. 277–288, Oct. 2008.
- [16] H. Aburema, B. Hanson, M. Fairweather, and M. Colombo, "A generalised multiphase modelling approach with heat transfer and thermal phase change," *International Journal of Heat and Fluid Flow*, vol. 109, p. 109524, Oct. 2024.
- [17] M. A. Amidu and H. Kim, "Modeling and simulation of flow boiling heat transfer on a downward-facing heating wall in the presence of vapor slugs," *Nuclear Engineering and Design*, vol. 351, pp. 175–188, Sep. 2019.
- [18] S. Tom, P. Mangarjuna Rao, B. Venkatraman, and S. Raghupathy, "Development of cfd based model for sodium flow boiling in narrow channel akin to sfr fuel subchannel towards high void fraction regimes," *Nuclear Engineering and Design*, vol. 396, p. 111877, Sep. 2022.
- [19] E. Krepper, R. Rzehak, C. Lifante, and T. Frank, "Cfd for subcooled flow boiling: Coupling wall boiling and population balance models," *Nuclear Engineering and Design*, vol. 255, pp. 330–346, Feb. 2013.
- [20] X. Peng and G. Peterson, "The effect of thermofluid and geometrical parameters on convection of liquids through rectangular microchannels," *International Journal of Heat and Mass Transfer*, vol. 38, no. 4, pp. 755–758, Mar. 1995.

[21] Y. Han, Y. Liu, M. Li, and J. Huang, "A review of development of micro-channel heat exchanger applied in air-conditioning system," *Energy Procedia*, vol. 14, pp. 148–153, 2012.

- [22] D. Tuckerman and R. Pease, "High-performance heat sinking for vlsi," *IEEE Electron Device Letters*, vol. 2, no. 5, pp. 126–129, May 1981.
- [23] A. J. S.S. Mehendale, "Evaporative heat transfer in mesoscale heatexchangers," in *ASHRAE Trans*, vol. 106, no. 1, 2000, pp. 446–452.
- [24] S. G. Kandlikar and W. J. Grande, "Evolution of microchannel flow passages—thermohydraulic performance and fabrication technology," *Heat Transfer Engineering*, vol. 24, no. 1, pp. 3–17, Jan. 2003.
- [25] P. A. Kew and K. Cornwell, "Correlations for the prediction of boiling heat transfer in small-diameter channels," *Applied Thermal Engineering*, vol. 17, no. 8–10, pp. 705–715, Aug. 1997.
- [26] L. Cheng and G. Xia, "Flow patterns and flow pattern maps for adiabatic and diabatic gas liquid two phase flow in microchannels: fundamentals, mechanisms and applications," *Experimental Thermal and Fluid Science*, vol. 148, p. 110988, Oct. 2023.
- [27] L. Cheng, G. Xia, and J. R. Thome, "Flow boiling heat transfer and two-phase flow phenomena of co2 in macro- and micro-channel evaporators: Fundamentals, applications and engineering design," *Applied Thermal Engineering*, vol. 195, p. 117070, Aug. 2021.
- [28] R. Gupta and A. Deshpande, *CFD Modeling of Two-Phase Flow in Mini and Microchannels*. Springer Nature Singapore, 2023, pp. 1279–1304.
- [29] V. Hernandez-Perez, M. Abdulkadir, and B. Azzopardi, "Grid generation issues in the cfd modelling of two-phase flow in a pipe," *The Journal of Computational Multiphase Flows*, vol. 3, no. 1, pp. 13–26, Mar. 2011.
- [30] S. Hardt and F. Wondra, "Evaporation model for interfacial flows based on a continuum-field representation of the source terms," *Journal of Computational Physics*, vol. 227, no. 11, pp. 5871–5895, May 2008.
- [31] M. Ishii and T. Hibiki, *Thermo-Fluid Dynamics of Two-Phase Flow*. Springer US, 2006.
- [32] N. Kurul and M. Z. Podowski, "Multidimensional effects in forced convection subcooled boiling," in *Proceeding of International Heat Transfer Conference 9*. Begellhouse, 1990.

[33] T. Fouilland, D. Fletcher, and B. Haynes, "Film and slug behaviour in intermittent slug–annular microchannel flows," *Chemical Engineering Science*, vol. 65, no. 19, pp. 5344–5355, Oct. 2010.

- [34] N. Shao, A. Gavriilidis, and P. Angeli, "Flow regimes for adiabatic gas–liquid flow in microchannels," *Chemical Engineering Science*, vol. 64, no. 11, pp. 2749–2761, Jun. 2009.
- [35] M. K. Akbar, D. A. Plummer, and S. M. Ghiaasiaan, "Gas-liquid two-phase flow regimes in microchannels," in *Heat Transfer, Volume 7*, ser. IMECE2002. ASMEDC, Jan. 2002, pp. 527–534.
- [36] T. Harirchian and S. V. Garimella, "Boiling heat transfer and flow regimes in microchannels—a comprehensive understanding," *Journal of Electronic Packaging*, vol. 133, no. 1, Mar. 2011.
- [37] N. Thomas, "Entrapment and transport of bubbles by transient large eddies in turbulent shear flow," *BHRA International Conference on the Physical Modelling of Multiphase Flow*, 1983.
- [38] I. Žun, "The transverse migration of bubbles influenced by walls in vertical bubbly flow," *International Journal of Multiphase Flow*, vol. 6, no. 6, pp. 583–588, Dec. 1980.
- [39] D. Drew and R. Lahey, "The virtual mass and lift force on a sphere in rotating and straining inviscid flow," *International Journal of Multiphase Flow*, vol. 13, no. 1, pp. 113–121, Jan. 1987.
- [40] A. Tomiyama, H. Tamai, I. Zun, and S. Hosokawa, "Transverse migration of single bubbles in simple shear flows," *Chemical Engineering Science*, vol. 57, no. 11, pp. 1849–1858, Jun. 2002.
- [41] E. Baglietto and M. Christon, "Demonstration and assessment of advanced modeling capabilities to multiphase flow with sub-cooled boiling," CASL, Tech. Rep., 2013.
- [42] D. LEGENDRE and J. MAGNAUDET, "The lift force on a spherical bubble in a viscous linear shear flow," *Journal of Fluid Mechanics*, vol. 368, pp. 81–126, Aug. 1998.
- [43] P. G. Saffman, "The lift on a small sphere in a slow shear flow," *Journal of Fluid Mechanics*, vol. 22, no. 2, pp. 385–400, Jun. 1965.
- [44] T. Auton, "The lift force on a spherical rotational flow," *Journal of Fluid Mechanics*, vol. 183, pp. 199–218, 1987.
- [45] J. B. McLaughlin, "Inertial migration of a small sphere in linear shear flows," *Journal of Fluid Mechanics*, vol. 224, pp. 261–274, Mar. 1991.

[46] R. M. Sugrue, "A robust momentum closure approach for multiphase computational fluid dynamics applications," Ph.D. dissertation, Massachusetts Institute of Technology, Cambridge, MA, USA, Sep. 2017.

- [47] A. D. Burns, T. Frank, I. Hamill, and J.-M. Shi, "The favre averaged drag model for turbulent dispersion in eulerian multi-phase flows," in *Proceedings of the 5th International Conference on Multiphase Flow (ICMF'04)*, Yokohama, Japan, May 2004, paper No. 392.
- [48] J. Laviéville, N. Mérigoux, M. Guingo, C. Baudry, and S. Mimouni, "A generalized turbulent dispersion model for bubbly flow numerical simulation in neptune-cfd," *Nuclear Engineering and Design*, vol. 312, pp. 284–293, Feb. 2017.
- [49] A. D. Gosman, C. Lekakou, S. Politis, R. I. Issa, and M. K. Looney, "Multidimensional modeling of turbulent two-phase flows in stirred vessels," *AIChE Journal*, vol. 38, no. 12, pp. 1946–1956, Dec. 1992.
- [50] C. Ljus, "On particle transport and turbulence modification in air-particle flows," Ph.D. dissertation, Chalmers University of Technology, Sweden, 2000.
- [51] M. López de Bertodano, "Turbulent bubbly two-phase flow in a triangular duct," phdthesis, Rensselaer Polytechnic Institute, Troy, New York, 1992.
- [52] P. Carrica, D. Drew, F. Bonetto, and R. Lahey, "A polydisperse model for bubbly two-phase flow around a surface ship," *International Journal of Multiphase Flow*, vol. 25, no. 2, pp. 257–305, Mar. 1999.
- [53] V. E. Nakoryakov, O. N. Kashinsky, V. V. Randin, and L. S. Timkin, "Gas-liquid bubbly flow in vertical pipes," *Journal of Fluids Engineering*, vol. 118, no. 2, pp. 377–382, Jun. 1996.
- [54] J. Marié, E. Moursali, and S. Tran-Cong, "Similarity law and turbulence intensity profiles in a bubbly boundary layer at low void fractions," *International Journal of Multiphase Flow*, vol. 23, no. 2, pp. 227–247, Apr. 1997.
- [55] S. Antal, R. Lahey, and J. Flaherty, "Analysis of phase distribution in fully developed laminar bubbly two-phase flow," *International Journal of Multiphase Flow*, vol. 17, no. 5, pp. 635–652, Sep. 1991.
- [56] J. Lu and G. Tryggvason, "Dynamics of nearly spherical bubbles in a turbulent channel upflow," *Journal of Fluid Mechanics*, vol. 732, pp. 166–189, Aug. 2013.
- [57] A. Tomiyama, "Struggle with computational bubble dynamics," *Multiphase Science and Technology*, vol. 10, no. 4, pp. 369–405, 1998.
- [58] T. Frank, P. Zwart, E. Krepper, H.-M. Prasser, and D. Lucas, "Validation of cfd models for mono- and polydisperse air—water two-phase flows in pipes," *Nuclear Engineering and Design*, vol. 238, no. 3, pp. 647–659, Mar. 2008.

[59] N. Lubchenko, B. Magolan, R. Sugrue, and E. Baglietto, "A more fundamental wall lubrication force from turbulent dispersion regularization for multiphase cfd applications," *International Journal of Multiphase Flow*, vol. 99, pp. 179–192, 2018.

- [60] D. Shaver and M. Podowski, "Modeling of interfacial forces for bubbly flows in subcooled boiling conditions," in *Transactions of the American Nuclear Society*, vol. 113. (Proc. of ANS Winter Meeting, 2015, pp. 1368–1371.
- [61] Z. A. N. L. Schiller, "Drag coefficient correlation," Z. Ver. Dtsch. Ing., vol. 77, pp. 318–320, 1935.
- [62] A. Tomiyama, I. Kataoka, I. Zun, and T. Sakaguchi, "Drag coefficients of single bubbles under normal and micro gravity conditions," *JSME International Journal. Series B, Fluids and Thermal Engineering*, vol. 41, no. 2, pp. 472–479, 1998.
- [63] N. Z. M. Ishii, "Drag coecient and relative velocity in bubbly, droplet, or particulate flows," *AlChE Journal*, vol. 25, no. 5, pp. 843–855, 1979.
- [64] A. A. Kendoush, "The drag forces on a taylor bubble rising steadily in vertical pipes," *Journal of Energy and Power Technology*, vol. 3, no. 4, pp. 1–1, Oct. 2021.
- [65] G. Bozzano and M. Dente, "Shape and terminal velocity of single bubble motion: a novel approach," *Computers &; Chemical Engineering*, vol. 25, no. 4–6, pp. 571–576, May 2001.
- [66] C. Y. Wen and Y. H. Yu, "A generalized method for predicting the minimum fluidization velocity," *AIChE Journal*, vol. 12, no. 3, pp. 610–612, May 1966.
- [67] D. GIDASPOW, ONE-DIMENSIONAL STEADY GAS-SOLID FLOW. Elsevier, 1994, pp. 31–60.
- [68] W. Liu, Y. He, M. Li, C. Huang, and Y. Liu, "Effect of drag models on hydrodynamic behaviors of slurry flows in horizontal pipes," *Physics of Fluids*, vol. 34, no. 10, Oct. 2022.
- [69] R. Rzehak and E. Krepper, "Cfd modeling of bubble-induced turbulence," *International Journal of Multiphase Flow*, vol. 55, pp. 138–155, Oct. 2013.
- [70] B. Launder and D. Spalding, *Mathematical Models of Turbulence*. Academic Press, 1972.
- [71] D. C. Wilcox, "Reassessment of the scale-determining equation for advanced turbulence models," *AIAA Journal*, vol. 26, no. 11, pp. 1299–1310, Nov. 1988.
- [72] Y. Sato and K. Sekoguchi, "Liquid velocity distribution in two-phase bubble flow," *International Journal of Multiphase Flow*, vol. 2, no. 1, pp. 79–95, Jun. 1975.

[73] S. Lo and D. Zhang, "Modelling of break-up and coalescence in bubbly two-phase flows," *The Journal of Computational Multiphase Flows*, vol. 1, no. 1, pp. 23–38, Jan. 2009.

- [74] H. Hulburt and S. Katz, "Some problems in particle technology," *Chemical Engineering Science*, vol. 19, no. 8, pp. 555–574, Aug. 1964.
- [75] G. Vaessen, "Coalescence and breakup modelling in a two-phase cfd code: theoretical framework," BRITE, Report III-1, Dec. 1998, developed under a European Project, Brite/EuRam BE 4322.
- [76] R. Bowring, "Physical model based on bubble detachmentand calculation of steam voidage in the subcooled region of aheated channel. menergi," Institute for Atomenergi, Halden, Norway, Tech. Rep., 1963.
- [77] D. Kenning and V. H. Del Valle M, "Fully-developed nucleate boiling: Overlap of areas of influence and interference between bubble sites," *International Journal of Heat and Mass Transfer*, vol. 24, no. 6, pp. 1025–1032, Jun. 1981.
- [78] R. L. Judd and K. S. Hwang, "A comprehensive model for nucleate pool boiling heat transfer including microlayer evaporation," *Journal of Heat Transfer*, vol. 98, no. 4, pp. 623–629, Nov. 1976.
- [79] T. Hibiki and M. Ishii, "Active nucleation site density in boiling systems," *International Journal of Heat and Mass Transfer*, vol. 46, no. 14, pp. 2587–2601, Jul. 2003.
- [80] L. W. Jakob M., "Heat transfer from a horizontal plate," *Forch.Gebiete Ingenieur* W, vol. 4, no. 2, pp. 75–81, 1933.
- [81] R. Séméria, "La cinématographie ultra-rapide et l'ébullition à haute pression," *La Houille Blanche*, vol. 49, no. 6, pp. 679–686, Oct. 1963.
- [82] R. Cole, "A photographic study of pool boiling in the region of the critical heat flux," *AIChE Journal*, vol. 6, no. 4, pp. 533–538, Dec. 1960.
- [83] Z. Wang, D. Shaver, and M. Podowski, "On the modeling of wall heat flux partitioning in subcooled flow boiling," *Transactions of the American Nuclear Society*, vol. 114, pp. 881–883, 06 2016.
- [84] R. Kommajosyula, "Development and assessment of a physics-based model for subcooled flow boiling with application to cfd," Ph.D. dissertation, Massachusetts Institute of Technology, Cambridge, MA, USA, Sep. 2020.
- [85] L. Gilman and E. Baglietto, "A self-consistent, physics-based boiling heat transfer modeling framework for use in computational fluid dynamics," *International Journal of Multiphase Flow*, vol. 95, pp. 35–53, Oct. 2017.

[86] E. Baglietto, "GEN-II Wall Boiling Models: A Self-Consistent, Physics-Based Framework," https://nuclear.mit.edu, 2023, lecture CMFD.07, Thermal-Hydraulics in Power Technology, MIT.

- [87] G. Kocamustafaogullari and Z. Wang, "An experimental study on local interfacial parameters in a horizontal bubbly two-phase flow," *International Journal of Multiphase Flow*, vol. 17, no. 5, pp. 553–572, Sep. 1991.
- [88] T. Hibiki and M. Ishii, "Lift force in bubbly flow systems," *Chemical Engineering Science*, vol. 62, no. 22, pp. 6457–6474, Nov. 2007.
- [89] C. Reiss, A. Gerschenfeld, and C. Colin, "Boiling-flow multiphase cfd simulations for nuclear reactor conditions without interfacial area transport equation," *Nuclear Engineering and Design*, vol. 428, p. 113453, Nov. 2024.
- [90] M. Colombo and M. Fairweather, "Prediction of bubbly flow and flow regime development in a horizontal air-water pipe flow with a morphology-adaptive multifluid cfd model," *International Journal of Multiphase Flow*, vol. 184, p. 105112, Mar. 2025.
- [91] N. Zuber, "On the dispersed two-phase flow in the laminar flow regime," *Chemical Engineering Science*, vol. 19, no. 11, pp. 897–917, Nov. 1964.
- [92] V. L. Burris, D. F. McGinnis, and J. C. Little, "Predicting oxygen transfer and water flow rate in airlift aerators," *Water Research*, vol. 36, no. 18, pp. 4605–4615, Nov. 2002.
- [93] K. Triplett, S. Ghiaasiaan, S. Abdel-Khalik, A. LeMouel, and B. McCord, "Gas–liquid two-phase flow in microchannels part ii: void fraction and pressure drop," *International Journal of Multiphase Flow*, vol. 25, no. 3, pp. 395–410, Apr. 1999.
- [94] D. Lucas, E. Krepper, and H.-M. Prasser, "Prediction of radial gas profiles in vertical pipe flow on the basis of bubble size distribution," *International Journal of Thermal Sciences*, vol. 40, no. 3, pp. 217–225, Mar. 2001.
- [95] A. Ebrahimi and E. Khamehchi, "A robust model for computing pressure drop in vertical multiphase flow," *Journal of Natural Gas Science and Engineering*, vol. 26, pp. 1306–1316, Sep. 2015.
- [96] W. Zhang, T. Hibiki, and K. Mishima, "Correlations of two-phase frictional pressure drop and void fraction in mini-channel," *International Journal of Heat and Mass Transfer*, vol. 53, no. 1–3, pp. 453–465, Jan. 2010.
- [97] E. Krepper, D. Lucas, and H.-M. Prasser, "On the modelling of bubbly flow in vertical pipes," *Nuclear Engineering and Design*, vol. 235, no. 5, pp. 597–611, Feb. 2005.

[98] T. Fukano and T. Furukawa, "Prediction of the effects of liquid viscosity on interfacial shear stress and frictional pressure drop in vertical upward gas—liquid annular flow," *International Journal of Multiphase Flow*, vol. 24, no. 4, pp. 587–603, Jun. 1998.

- [99] A. Judd, "Convective boiling and condensation." *Chemical Engineering Science*, vol. 28, no. 9, p. 1775, Sep. 1973.
- [100] T. Höhne, E. Krepper, G. Montoya, and D. Lucas, "Cfd-simulation of boiling in a heated pipe including flow pattern transitions using the gentop concept," *Nuclear Engineering and Design*, vol. 322, pp. 165–176, Oct. 2017.
- [101] F. Bolourchifard, K. Ardam, F. Dadras Javan, B. Najafi, P. Vega Penichet Domecq, F. Rinaldi, and L. P. M. Colombo, "Pressure drop estimation of two-phase adiabatic flows in smooth tubes: Development of machine learning-based pipelines," *Fluids*, vol. 9, no. 8, p. 181, Aug. 2024.





# A.1 STAR-CCM+ Implementation Code

## A.1.1 Sugrue's Lift Coefficient

**Listing A.1:** Sugrue's Lift Coefficient STAR-CCM+ Code

```
1 Eo = g * ${DensityLiquid} - ${DensitySteam}) * pow(${SauterMeanDiameterSteam},2) / ${SurfaceTension}
2
3 Wo = {Eo} * ${TurbulentKineticEnergyLiquid} / pow(mag($${VelocityLiquid} - $$ {VelocitySteam}),2)
4
5 CL_Sugrue = min(0.03, 5.0404 - 5.0781 * pow(($Wo), 0.0108))
```

# A.1.2 Lopez de Bertodano's Turbulent Dispersion Model

**Listing A.2:** Lopez de Bertodano's Turbulent Dispersion Model STAR-CCM+ Code

```
1 F_TD_D = {Lopez_de_Bertodano_Coef} * ${DensityLiquid} * ${
        TurbulentKineticEnergyLiquid} * grad(${VolumeFractionLiquid})
2
3 F_TD_C = -${Lopez_de_Bertodano_Coef} * ${DensityLiquid} * ${
        TurbulentKineticEnergyLiquid} * grad(${VolumeFractionLiquid})
4
5 CTD_L = 0.1
```



#### **B.1** Other Used Codes

### **B.1.1** Python Script for Turbulence Calculation

**Listing B.1:** Python script used to calculate turbulence quantities for inlet boundary conditions.

```
2 from CoolProp.CoolProp import PropsSI
3 from math import pi
5 # Geometry and flow setup
6 d = 0.00145 # Pipe diameter [m]
7 A = pi * (d/2)**2 # Cross-sectional area [m<sup>2</sup>]
8 P = 1e5 # Pressure [Pa]
9 T = 373.15 # Temperature [K]
w = 71 * A # Mass flow rate [kg/s]
12 # Fluid properties
13 rho = PropsSI('D', 'T', T, 'P', P, 'water')
14 mu = PropsSI('V', 'T', T, 'P', P, 'water')
15 nu = mu / rho # Kinematic viscosity [m²/s]
# Bulk velocity and Reynolds number
u = w / A / rho
19 Re = rho * u * d / mu
21 # Turbulence intensity for fully developed pipe flow
I = 0.16 * Re**(-1/8)
24 # Turbulent kinetic energy
25 k = 1.5 * (u * I)**2
27 # Turbulence length scale (ANSYS pipe estimate)
1 = 0.038 * d
```

100 B. Appendix

```
30 # Turbulent dissipation rate and specific dissipation
31 C_mu = 0.09
32 eps = C_mu * k**(3/2) / 1
33 omega = eps / (C_mu * k)
34
35 # Turbulent viscosity ratio
36 v_t = (3/2)**0.5 * u * I * 1
37 v_r = v_t / nu
```

# **B.1.2** MITB STAR-CCM+ Implementation Code

The code can be requested.

